Field resolving spectrometer for mid-infrared molecular spectroscopy

Syed Ali Hussain

München 2021

Field resolving spectrometer for mid-infrared molecular spectroscopy

Syed Ali Hussain

Dissertation
an der Fakultät für Physik
der Ludwig-Maximilians-Universität
München

vorgelegt von
Syed Ali Hussain
aus Chiniot (Pakistan)

München, den 26.11.2020

Zusammenfassung

Die Untersuchung molekularer Proben mit breitbandiger Mittelinfrarot-Strahlung (MIR) führt zu hochspezifischen "Schwingungs-Fingerabdrücken", die eine Fülle von Informationen über die molekulare Struktur und Zusammensetzung enthalten. Dies macht die Schwingungsspektroskopie zu einem leistungsstarken und vielseitigen Werkzeug für Anwendungen, die von der Grundlagenwissenschaft über die Biowissenschaften bis hin zu industriellen Anwendungen reichen. Konventionelle MIR-Spektroskopietechniken stoßen auf starke Einschränkungen in der Nachweisempfindlichkeit, insbesondere aufgrund der schlechten Kohärenzeigenschaften üblicher MIR-Quellen sowie der mäßigen Detektivität und des dynamischen Bereichs breitbandiger MIR-Detektoren. Die in dieser Arbeit berichtete Forschung hat sich mit der Suche nach neuartigen Wegen zur Erschließung des Potenzials breitbandiger MIR-Fingerabdrücke befasst, wobei moderne Hochleistungs-Femtosekunden-Lasertechnologie zum Einsatz kommt.

Im ersten Teil der Arbeit wird über die Konstruktion oktavübergreifender, kohärenter Femtosekunden-MIR-Quellen berichtet, bei denen modernste Yb:YAG-modengekoppelte Dünnscheiben-Oszillatoren mit 100 W mittlerer Leistung zum Einsatz kommen. Wir demonstrierten ultrabreitbandige kohärente MIR-Quellen mit einer Brillanz, die die von MIR-Experimenten bei Synchrotrons der 3. Generation übertrifft, und stellten fest, dass Pulse, die durch die Erzeugung von Intra-Puls-Differenzfrequenzmischung entstehen, eine überlegene (und unübertroffene) optische Wellenformstabilität im Vergleich zur gewöhnlichen optisch-parametrischen Verstärkung bieten. Die zeitliche Beschränkung der breitbandigen MIR-Strahlung auf Folgen von Pulsen mit einer Dauer von unter 100 Femtosekunden und die feldaufgelöste Detektion mittels elektro-optischer Abtastung (electro-optic sampling, EOS) ermöglicht die Detektion des molekularen Fingerabdrucksignals im nahen Infrarotbereich, wo hocheffiziente Detektoren mit hoher Dynamik verfügbar sind. Die optimierte EOS-Detektion ermöglichte eine lineare Antwort über einen dynamischen Intensitätsbereich von 150 dB bei einer zentralen Wellenlänge von 8,6 µm. Dies übertrifft den bisherigen Stand der Technik bei weitem und ebnet den Weg für Transmissionsmessungen mit hohem Signal-Rausch-Verhältnis von wässrigen biologischen Proben, wie biologischen Flüssigkeiten, lebenden Zellen und Gewebe.

Die Wellenformstabilität der Pulse im mittleren Infrarotbereich spielt eine entscheidende Rolle für reale feldaufgelöste Spektroskopiemessungen und ist von größter Bedeutung für präzisionsmetrologische Anwendungen. Im zweiten Teil dieser Arbeit wurde EOS mit hoher Quanteneffizienz für Präzisionsmessungen des Wellenformjitters eingesetzt und für Millionen von Pulsen ausgewertet. Diese Studie zeigte einen zeitlichen Jitter von wenigen Attosekunden im Band von 1 Hz bis 0,625 MHz zwischen dem Massenschwerpunkt der treibenden Nahinfrarot-Pulse und einzelnen Feld-Nulldurchgängen des entstehenden,

breitbandigen MIR-Feldes. Dies bestätigt die hervorragende Wellenformstabilität, die mit parametrischen Prozessen zweiter Ordnung mit einer um eine Größenordnung verbesserten Genauigkeit im Vergleich zu früheren Messungen erreicht werden kann. Darüber hinaus zeigte sich beim Chirpen des MIR-Pulses ein von der optischen Frequenz abhängiger Wellenformjitter im Attosekundenbereich, dessen Dynamik quantitativ auf das Intensitätsrauschen des modengekoppelten Oszillators zurückgeführt wurde. Somit validierte diese Studie EOS als breitbandige (sowohl im Radiofrequenz- als auch im optischen Bereich), hochempfindliche Messtechnik für die Dynamik optischer Wellenformen jenseits des standardmäßigen, das optische Spektrum integrierenden Träger-Hüllkurven-Phasenmodells.

Das im Rahmen dieser Arbeit entwickelte Instrument wurde für die ersten hochempfindlichen feldaufgelösten Messungen im molekularen Fingerabdruckbereich. Es ermöglichte den Nachweis von molekularen Konzentrationen über 5 Größenordnungen bis hinunter zu 200-ng/mL in wässrigen Lösungen und die Untersuchung lebender biologischer Systeme mit einer Dicke von bis zu 0,2 mm. Gegenwärtig wird das Instrument für die ersten groß angelegten Studien zur Erkennung von Krankheiten auf der Grundlage von Vibrations-Fingerabdrücken von menschlichem Blutserum eingesetzt.

Die Einführung der Intra-Scan-Referenzierung, die in den letzten Wochen dieser Doktorarbeit erfolgreich durchgeführt wurde, zusammen mit den Schnellabtasttechniken und der Erweiterung der spektralen MIR-Bandbreite, die in unserem Labor derzeit entwickelt werden, versprechen eine Ausweitung der in dieser Arbeit vorgestellten Technologie auf neue Ebenen der Empfindlichkeit und Reproduzierbarkeit in der Schwingungsspektroskopie. Neben dem direkten Nutzen für analytische Anwendungen werden diese Entwicklungen höchstwahrscheinlich auch neue Einblicke in Licht-Materie-Wechselwirkungen ermöglichen.

Abstract

The interrogation of molecular samples with broadband mid-infrared (MIR) radiation results in highly specific "vibrational fingerprints," containing a wealth of information on molecular structure and composition. This renders vibrational spectroscopy a powerful and versatile tool for applications ranging from fundamental science to the life sciences and to industrial applications. Conventional MIR spectroscopic techniques face severe limitations in detection sensitivity, in particular due to the poor coherence properties of common MIR sources as well as to the moderate detectivity and dynamic range of broadband MIR detectors. The research reported in this thesis has addressed the quest for novel routes towards tapping the potential of MIR spectral fingerprinting, harnessing modern, high-power femtosecond laser technology.

The first part of the work reports the construction of octave-spanning, coherent femtosecond MIR sources, employing state-of-the-art 100-W-average-power-level thin-disk Yb:YAG modelocked oscillators. We demonstrated ultrabroadband coherent MIR sources with a brilliance exceeding that of MIR beamlines at 3rd-generation synchrotrons, and found that pulses emerging via intra-pulse difference frequency generation offer superior (and unparalleled) optical-waveform stability as compared to standard optical-parametric amplification. The temporal confinement of broadband MIR radiation to trains of sub-100-femtosecond pulses, together with field-resolved detection via electro-optic sampling (EOS) affords detection of the molecular fingerprint signal in the near-infrared region, where highly-efficient, high-dynamic-range detectors exist. Optimized EOS detection enabled a linear response over an intensity dynamic range of 150 dB at a central wavelength of 8.6 μm. This exceeds the previous state of the art by a large margin and has paved the way to high-signal-to-noise-ratio transmission measurements of aqueous biological samples like living cells and tissue.

The waveform stability of the mid-infrared pulses plays a crucial role for real-life field-resolved spectroscopy measurements, and is of paramount importance for precision-metrological applications. In the second part of this thesis, high-quantum-efficiency EOS was employed for precision measurements of waveform jitter, evaluated for millions of pulses. This study demonstrated few-attosecond temporal jitter in the 1-Hz-to-0.625-MHz band, between the centre of mass of the driving near-infrared pulses, and individual field zero-crossings of the emerging, broadband mid-infrared field. This confirms the outstanding waveform stability achievable with second-order parametric processes with an order-of-magnitude improved accuracy compared to previous measurements. Furthermore, chirping the MIR pulse revealed attosecond-level optical-frequency-dependent waveform jitter, whose dynamics were quantitatively traced back to excessive intensity noise of the mode-locked oscillator. Thus, this study validated EOS as a broadband (both in the radio-frequency and in the optical domain), high-sensitivity measurement technique for the

dynamics of optical waveforms beyond the standard, optical-spectrum-integrating carrier-envelope phase model.

The instrument developed during this thesis was utilized for the first highly sensitive field-resolved measurements in the MIR molecular fingerprint region. It enabled the detection of molecular concentrations spanning 5 orders of magnitude down to 200-ng/mL in aqueous solutions and the examination of living biological systems with a thickness of up to 0.2 mm. Currently, the instrument is being used for the first large-scale studies on disease recognition based on vibrational fingerprinting of human blood serum.

The implementation of intra-scan referencing, successfully carried out in the last weeks of this doctoral work, together with fast-scanning techniques and the extension of the MIR spectral bandwidth which are underway at our laboratory, promise to extend the technology pioneered in this thesis to new levels of sensitivity and reproducibility in vibrational spectroscopy. In addition to directly benefitting analytical applications, these developments are likely to afford novel insights into light-matter interactions.

Table of Contents

List of Figures

List of Tables

Chapter 1

Introduction

The quest to probe matter lies in the very nature of human beings. Different molecular structures that constitute matter possess specific signatures for their identification and quantification. This makes optical spectroscopy an indispensable tool for the analysis of molecules in physics, chemistry, biosciences and related disciplines[1–6]. The scheme relies on the absorption of light, which causes the molecules in a sample to vibrate. The "optical response" is then detected by either recording the reduction in the intensity of the incident light or by monitoring the free-induction decay.

Transitions between molecular vibrational states lie in the wavelength range of 1-20 μm (10000-500 cm^{-1}). Vibrational modes describing the motion of chemical bonds of the molecule, are mainly of two types: stretching and bending. The former is characterized by a variation in interatomic distances along the bond axis and the latter by the change in bond angles. Two widely used techniques based on vibrational studies are Raman spectroscopy and infrared (IR) spectroscopy. Raman spectroscopy utilizes the detection of inelastically scattered light to explore the molecular information[7,8]. IR spectroscopy, on the other hand, relies on the absorption of incident light and re-emission of light to study the transition between vibrational energy levels of the molecules[9,10]. Both of these techniques provide molecular-specific information based on the fact that each molecule has a characteristic fingerprint.

The label-free nature of these techniques makes them highly attractive both for fundamental research and for industrial applications. Direct and broadband probing of molecular vibrations at their characteristic frequencies in the mid-infrared (MIR) fingerprint region profits from the large interaction cross-sections, along with a unique combination of spectral coverage and sensitivity[4,11].

To date, the most widespread scheme for infrared vibrational spectroscopy, namely Fourier-transform infrared spectroscopy[10] (FTIR), relies on thermal sources. These sources have technological limitations in terms of brightness and lack spatial as well as temporal coherence. This leads to a limit in their performance in terms of sensitivity to weak signals, investigation of thick samples, and dynamic range of detectable signals. An alternative to such broadband sources is synchrotron-based radiation, but these sources are scarce and expensive. Table 1.1 shows the comparative overview of broadband IR sources.

Table 1.1 | Overview of infrared sources.

Source	Bandwidth	Brightness	Spatial coherence	Temporal coherence	Compactness
Globar	✓	✗	✗	✗	✓
Synchrotron	✓	✓	✓	✗	✗
Laser-Based	✓	✓	✓	✓	✓

Developments in femtosecond laser technology with mode-locked oscillators, promise an alternative route for optical metrology and precision spectroscopy. The temporal interplay between optical gain, linear and nonlinear propagation in a mode-locked laser oscillator[12] results in a train of output pulses with highly reproducible shot-to-shot intensity envelopes, and with durations of few hundreds of femtoseconds. These sophisticated sources became powerful tools for a variety of time- and frequency-domain applications.

The lack of suitable laser gain media for longer wavelengths (> 3μm) restricts these oscillators to the near-infrared and visible spectral regions. At wavelengths close to 1 μm, femtosecond pulses with more than hundred watt of average power have been realized[13–16]. Laser sources emitting at 2-μm wavelength, on the other hand, can provide several watts of average power directly from the oscillator[17–19] These high-power laser sources can be utilized in frequency down-conversion processes, to achieve femtosecond laser pulses in the MIR spectral region.

The control of phase of the optical carrier wave with respect to its intensity envelope[20–22] further pushed the precision limits of temporal and frequency resolution in optical measurements. Second-order nonlinear processes such as optical parametric amplification (OPA) and intrapulse difference-frequency generation (IPDFG), intrinsically and passively[23,24] comprises this control. The nonlinear polarization responsible for the emission of the difference-frequency wave follows the temporal intensity envelope of the driving pulse[25]. This renders passive stabilization techniques a preferred scheme for the generation of waveform-stable ultrashort pulse trains and carrier-envelope offset frequency controlled frequency combs[19,26–28].

These developments of laser technology have spawned MIR radiation sources meeting the long-standing challenge of combining broad bandwidth with high average power and outstanding coherence properties[27–30]. Another unique feature of femtosecond MIR laser sources is the temporal confinement of the broadband MIR pulses to durations significantly shorter than the typical picosecond dephasing time of molecular vibrations[31]. Using frequency up-conversion in electro-optic sampling, this property can be utilized for

time-domain observation[32,33] of resonant MIR molecular vibrations following impulsive excitation in field-resolved spectroscopy (FRS).

In FRS, the generation of waveform-stable MIR pulses along with electro-optic sampling[26] detection grants access to the electric field emitted by the sample molecules as the most direct observation of the molecular dipoles coherently oscillating following the impulsive excitation. Additionally, signal strength in FRS scales linearly with the electric field of the MIR waveform rather than with its intensity, in contrast to conventional techniques. This makes FRS a promising approach to study thick, strongly attenuating samples, and rapidly dephasing molecular vibrations in biological samples[34–36].

1.1 Thesis outline

The thesis is structured as follows: Chapter 2 addresses theoretically the comparison of the minimum detectable absorbance in time-integrating, frequency-resolved spectroscopy and in electric-field-resolved infrared spectroscopy.

Chapter 3 covers details of the laser front-end, including the laser oscillator and MIR generation. Experimental setups for MIR generation based on narrowband and broadband pump optical parametric amplification, and intra-pulse difference frequency generation are presented. The advantages and drawbacks of both schemes for are summarized.

Chapter 4 discusses the electro-optic sampling detection setup. The performance of electro-optic detection in two *Infrasampler*[*] setups is demonstrated.

Chapter 5 combines all the technological know-how into realizing the world's first field-resolving spectrometer optimized for liquid biopsies, and presents its performance. Electro-optic sampling is introduced as a highly sensitive metrology technique for the analysis of infrared waveform stability in radio-frequency domain of noise and in the optical domain of the laser pulse. The unprecedented temporal coherence and waveform stability was utilized to explore sensitivity and specificity of first experimental studies towards real-world application of the field-resolving spectrometer.

Finally, Chapter 6 concludes the experimental findings and gives an overview of future prospects.

---

[*] Infrasampler = Infrared field sampling measurement device. This name is adopted for the spectrometer designed to measure the electric field of the mid-infrared laser.

Chapter 2

Theoretical Background

Advancements in spectroscopic technologies offer various tools and methods to study the interaction between electromagnetic radiation and fundamental molecular modes. Optical techniques interrogate the molecular sample by detecting the resonant vibrational response to infrared excitation. As molecules have unique vibrational eigenstates, when the molecular fragments are subjected to spectroscopic interrogation, their dephasing results in sample-specific temporal and spectral responses. These spectral fingerprints provide information about individual molecules, the sample's molecular composition and structure.

2.1 Mid-infrared absorption spectroscopy

Traditionally, the measurement of molecular absorption is performed by frequency resolved intensity attenuation of input radiation. The intensity noise of the source directly limits the minimum detectable signal for each spectral component and their reproducibility. Molecular absorption is detected when the intensity of the spectral component corresponding to the absorption is smaller than $I_0(1 - \sigma)$, where I_0 is the mean reference intensity and σ is the relative standard deviation for a given spectral component from measurement to measurement. For a propagation length z and absorption coefficient α, Beer's law reads

$$I_s = I_0 e^{-\alpha z}, \tag{2.1}$$

where I_s represents the spectral component intensity. The inequality $e^{-\alpha x} \leq 1 - \sigma$ needs to hold for an absorption to be detectable. This implies,

$$\alpha x \geq \ln\left(\frac{1}{1 - \sigma}\right) \tag{2.2}$$

This can be further approximated for small values of σ by Taylor expansion. This gives,

$$\ln\left(\frac{1}{1 - \sigma}\right) \approx \ln(1 + \sigma) \approx \sigma \tag{2.3}$$

So, the minimum detectable absorbance (MDA) is:

$$MDA_{FD} \approx \sigma \tag{2.4}$$

This relation holds for experimental schemes that measure time-integrated fields in the frequency domain. The relative standard deviation σ incorporates contributions from the excitation source noise, detection noise, and from the dynamic range of the measurement scheme.

2.2 Field resolved infrared spectroscopy

In this scheme, when a sample is subjected to excitation by an ultrashort infrared pulse, the emerging response is a superposition of the resonant and non-resonant fields. This can be modelled by solving the wave equation semi-classically[*]. The linear interaction of the infrared excitation pulse with the electric field amplitude envelope $E_0(t) = E(z = 0, t)$ propagating through the medium with absorption coefficient α_1 for the non-resonant interaction in the z-direction. The resonant absorption, can be described as a Lorentzian-shaped absorption band with a dephasing time T_L and peak absorption α_2. Here, we consider this band to be centred at the carrier frequency of the infrared excitation pulse, so the intensity of this pulse is attenuated by $\exp[(\alpha_1 + \alpha_2)z]$. The dephasing time can be estimated by $T_L = (\pi c \delta v)^{-1}$, where δv is the full-width at half depth of the power spectral density absorption line, and c is the speed of light. Assuming that the pulse duration of the infrared pulse is smaller than T_L, the time-domain electric field envelope is given by:

$$E(z, t) = E_0(t) \exp\left(-\frac{1}{2}\alpha_1 z\right) - \varepsilon \cdot \exp\left(-\frac{1}{2}\alpha_1 z - \frac{t - t_{max}}{T_L}\right)$$
$$\cdot \frac{J_1\left(\sqrt{2\varepsilon(t - t_{max})}\right)}{\sqrt{2\varepsilon(t - t_{max})}} \int_{-\infty}^{t} E_0(t')dt', \quad (2.5)$$

where t_{max} denotes the time at the maximum of $E_0(t)$, J_1 denotes the first-order Bessel function and $\varepsilon = \frac{\alpha_2 z}{T_2}$. For a weak resonant absorption, the term $\alpha_2 z \ll 1$, and the term $\frac{J_1\left(\sqrt{2\varepsilon(t - t_{max})}\right)}{\sqrt{2\varepsilon(t - t_{max})}}$ can be approximated to $\frac{1}{2}$.

$$E(z, t) \approx E_{inst}(z, t) - \frac{1}{2}\frac{\alpha_2 z}{T_L} \exp\left(-\frac{t - t_{max}}{T_L}\right) \cdot \int_{-\infty}^{t} E_{inst}(z, t')dt' \quad (2.6)$$

The first term $E_{inst}(z, t) = E_0(t) \exp\left(-\frac{1}{2}\alpha_1 z\right)$, corresponds to the non-resonant sample response. The envelope decays quickly in time due to the ultrashort duration of the infrared excitation pulse. The second term corresponds to the ensemble-integrated macroscopic

---

[*] The formulism presented here is in close analogy to Ref. [31], and were calculated for the field-resolved infrared spectroscopy in Ref. [37].

electric field emitted by the coherent oscillations of the resonantly excited molecular dipoles. These oscillations decay exponentially with T_L and their strength is proportional to the number of emitters (i.e. $\alpha_2 z$). The negative sign in the second term shows that the phase of the resonant response is opposite to that of the nonresonant response. This appears as a Lorentzian absorption dip in the frequency domain representation of the total field.

Along with a weak resonant absorption, assuming that on the time scale of the infrared excitation pulse, the field is not attenuated by the resonant absorption, Eq. (2.6) becomes

$$E(z,t) \approx E_{inst}(z,t) - \frac{1}{2}\frac{\alpha_2 z}{T_L}\Theta(t - t_{max})\exp\left(-\frac{t - t_{max}}{T_L}\right)$$
$$\cdot \int_{-\infty}^{\infty} E_{inst}(z,t')dt', \tag{2.7}$$

where $\Theta(t)$ denotes the Heaviside step function. This holds well for an ultrashort infrared input pulse and a longer dephasing time. The second term on right side of the expression is a good approximation for the field emitted by resonantly excited polarization. This corresponds to Lorentzian emission with a spectral maximum of $\frac{1}{2}\alpha_2 zC$, where $C = \int_{-\infty}^{\infty} E_{inst}(z,t')dt'$.

The resonant response of the sample also overlaps in time with the non-resonant response. The effect of the non-resonant part can be minimized in the measured signal by applying a high-pass time filter at time t_B. This gives the resonant response in a background free manner. As the nonresonant contribution $E_{inst}(z,t)$ is negligible after time t_B, the time-filtered resonant response is given by:

$$\Theta(t - t_B)E(z,t) \approx -\frac{1}{2}\frac{\alpha_2 z}{T_L}\Theta(t - t_B)\exp\left(-\frac{t - t_B}{T_L}\right)\exp\left(-\frac{t_B}{T_2}\right)\cdot C. \tag{2.8}$$

This gives a good estimate of the Lorentzian emission line for the field delayed by time t_B and with spectral amplitude attenuated by $\exp\left(-\frac{t_B}{T_L}\right)$.

At the central frequency ($\omega = 0$ Hz, corresponding to 0 cm^{-1}), the magnitude of the Fourier transform of $E_{inst}(z,t)$ is:

$$\int_{-\infty}^{\infty} E_{inst}(z,t)\exp(-i\omega t)dt = \int_{-\infty}^{\infty} E_{inst}(z,t)dt = C$$

The magnitude ratio of the field envelope corresponding to the resonant response to that of the high-pass time-filtered instantaneous (nonresonant) response amounts to $\frac{1}{2}\alpha_2 z \exp\left(-\frac{t_B}{T_L}\right)$.

In field resolved spectroscopy, the oscillating electric field itself is the observable (rather than its envelope). For a carrier angular frequency ω_0, the electric field is related to its envelope $E(z,t)$, by multiplying the oscillating function $\cos(\omega_0 t)$ (the carrier-envelope phase is not considered here for simplicity). And the Fourier transform gives the two-sided spectrum with two copies of the $E(z,t)$ spectrum, at $-\omega_0$ and ω_0, with the magnitude of each component reduced by a factor of 0.5. The magnitude ratio remains unaffected, since this reduction applies for both the resonant and instantaneous non-resonant responses.

The minimum detectable absorbance for FRS will be when the signal S (high pass time filtered) of the resonant excitation equal to the background noise level N ($S/N = 1$). Normalization by the instantaneous field magnitude gives:

$$\frac{1}{2}\alpha_2 z \exp\left(-\frac{t_B}{T_L}\right) = \frac{1}{DR_E}, \tag{2.9}$$

where, the electric field dynamic range DR_E corresponds to the magnitude ratio of the instantaneous (nonresonant) field to the background in the frequency domain at the carrier frequency ω_0.

$$MDA_{FRS} = \frac{2}{DR_E} \exp\left(\frac{t_B}{T_L}\right) \tag{2.10}$$

This expression shows that the weakest detectable signal in an FRS measurement is largely immune to the intensity noise of the excitation pulse, for the time filtered signal. In the measurements, this time window is defined when the numerical difference between the two measurements reaches the detection noise floor. In a typical FRS measurement, for an aqueous sample (having a dephasing time on the order of a picosecond), this gives a minimum detectable absorbance[37] on the order of 10^{-6}. This criterion for estimation of the MDA can be extended to all optical frequencies of the excitation pulse, by extending the definition of DR_E, i.e. the magnitude ratio of the measured instantaneous response to the frequency dependent background level.

The intensity noise of the excitation pulse certainly puts a limit on the efficiency of the subtraction of measurements. But for an ultrashort pulse, the excitation pulse decays after a few hundreds of femtoseconds, down to the detection noise floor, while the signal from an aqueous sample has a dephasing time of several picoseconds. Thus, for the high

pass time filtered signal, the detection is mainly limited by the detection noise floor and not by the technical noise of the excitation pulse.

Chapter 3

Source of waveform-stable broadband infrared light

The generation and control of waveform-stable broadband light are of great interest[2] in both fundamental and applied research. Ultrashort near-infrared laser pulses with durations of a few femtoseconds have contributed to the observation and manipulation of chemical reactions[38,39], exploring highly nonlinear effects such as high-harmonic generation[40–42], current switching in solids[43], and field-resolved spectroscopy[26,37].

Mode-locked oscillators provide a train of temporally equidistant ultrashort pulses with durations in the range of a few hundred femtoseconds, and highly reproducible intensity envelopes. These ultrashort pulses enable many interesting applications in both the time and frequency domains. The two key ingredients required for most metrological applications are the broad bandwidth, to address a certain interaction in the material under observation, and high reproducibility of the electric field under the field envelope. The shot-to-shot reproducibility of the electric field requires different frequency modes locked with each other as well as phase-locked to the envelope of the electric field. This phase parameter is termed "carrier-envelope phase" (CEP). CEP stability is essential to achieve high reproducibility and a high signal-to-noise ratio in optical-field-sensitive measurements. For instance, strong-field effects depend on the instantaneous electric field rather than the intensity envelope, and this role becomes crucial for broadband sources, i.e., for few-cycle laser pulses.

The broad bandwidth is typically achieved by nonlinear mixing of the frequency components in a suitable medium, and the stability of the CEP is achieved by using either active[20,21] or passive schemes[23,24] (Figure 3.1). Active optical-phase stabilization is typically achieved by a phase measurement with an f-2f interferometer and providing the feedback via control electronics to the laser resonator. Passive stabilization is achieved in an all-optical scheme, such that CEP of mixing frequency components cancels out, resulting in the cancellation of shot-to-shot phase fluctuations. There are some clear advantages of the passive stabilization in comparison to active stabilization: (i) it is an all-optical technique; (ii) it uses a compact setup that directly produces a CEP-stable pulse train; (iii) it does not require feedback/control electronics. Furthermore, both of these schemes can be combined, noting that active stabilization provides constant phase for a limited frequency bandwidth, while passive stabilization provides a stable phase at the parametric output frequencies.
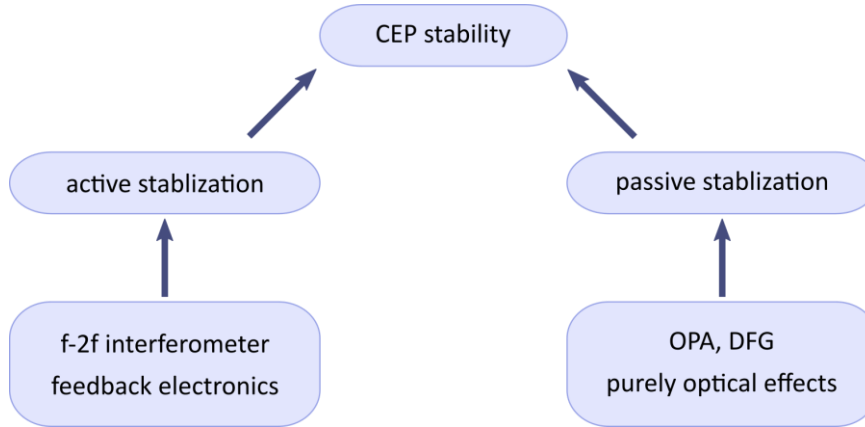
Figure 3.1 | Schematic representation of the CEP stabilization schemes.

This chapter describes the femtosecond front-end laser system used for the generation of passively waveform-stable mid-infrared light, in the frame of this thesis. Section 3.1 describes the femtosecond laser oscillator and the spectral compression needed to drive the parametric process. Section 3.2 presents the different schemes used to generate (nominally) waveform-stable mid-infrared pulses via optical parametric amplification and intra-pulse difference frequency generation, and a comparison between the two schemes.

3.1 Near-infrared femtosecond frontend

Most of the high-energy laser systems across the world are based on Ti:Sapphire technology, thanks to its unique properties as a laser medium, including large nonlinear index, high thermal conductivity, and broad gain bandwidth. However, it also has some limitations in terms of average and peak power scalability. This led to the development of a different family of femtosecond laser systems, based on Yb-doped active media, offering comparatively high average-power laser pulses[44–47]. The main drawback in Yb-based systems is the comparatively narrow gain bandwidth so that pulses with a duration of a few hundred femtoseconds are the shortest that have been achieved directly from the oscillator, so far. Extra-cavity nonlinear spectral broadening techniques provide a route to generate broadband ultrashort pulses from these high-average- and high-peak-power sources.

3.1.1 Yb:YAG Oscillator

The experiments presented in this thesis have been performed with three different Yb:YAG Kerr-lens mode-locked thin-disk (KLM TD) oscillators. For convenience, the first oscillator[47] is referred to as KLM-1, the second[48] as KLM-2 and the third[13,49] as KLM-3 throughout the thesis. An overview of the laser parameters of these oscillators is shown in Table 3.1.

Table 3.1 | Laser parameters of Kerr-lens mode-locked oscillators

Oscillator Name	Rep. rate (MHz)	Average power (W)	Pulse duration (fs)	Integrated RIN RMS (%)	Ave. power RMS (%)
KLM-1	37.5	50	230	0.1	0.16
KLM-2	100	70	250	0.1	-
KLM-3	28	120	220	0.07	< 0.1

The majority of the experiments presented in this thesis were performed with KLM-3, which offers the highest pulse energy, with higher stability and improved infrastructure as compared to the other two oscillators. Also, KLM-3 is used in the field-resolving spectrometer named InfraSampler 1.2, presented in detail in Chapter 5.

KLM-3 offers robust and turn-key laser operation. During the course of the experiments, only minor changes were required to improve the stability and handiness of the laser system. KLM-3 produces a train of pulses with a repetition rate of 28.3 MHz, full-width-half-maximum duration of 220 fs, and with an average power exceeding 120W. A picture of the setup is shown in Figure 3.2a. The laser cavity was built in a water-cooled monolithic aluminium housing resulting in relatively low thermal drifts. Laser housing and all optics mounts were water-cooled. For day-to-day operation, the output-coupling mirror, hard aperture, and end mirror were adjusted to reach the reference laser parameters without opening the housing. Inside the oscillator housing, a half-wave plate (HWP) followed by a thin-film polarizer is used, such that the rotation of the HWP defines the amount of laser power sent to the experiment. The rest is guided to a water-cooled thermal power meter.

Figure 3.2b shows the $sech^2$ fit to the autocorrelation (AC) measurement. The NIR beam has a nearly perfect Gaussian profile, as shown in the inset. Evaluating the measured AC width for 3.5 hours in steps of ~20 minutes, reveals a root-mean-square (RMS) deviation of 0.2%. The stability and reproducibility of the laser spectrum are crucial for the subsequent spectral broadening and temporal compression.

To further stabilize the frontend laser, active suppression of intensity noise based on an acousto-optic-modulator (AOM) in a configuration similar to Ref. [50] was implemented. Here, an error signal for the feedback loop was generated from the outer wing of the broadband NIR spectrum (presented in Section 3.1.3) using an indium gallium arsenide (InGaAs) amplified photodiode (Thorlabs, PDA20CS2). The signal of the photodiode was fed into ta PI^2D controller, which regulates the RF power of the AOM driver. The integrator parameters of the PI^2D controller were chosen to minimize noise at the lock-in detection frequency in electro-optic detection.

(a)

(b)
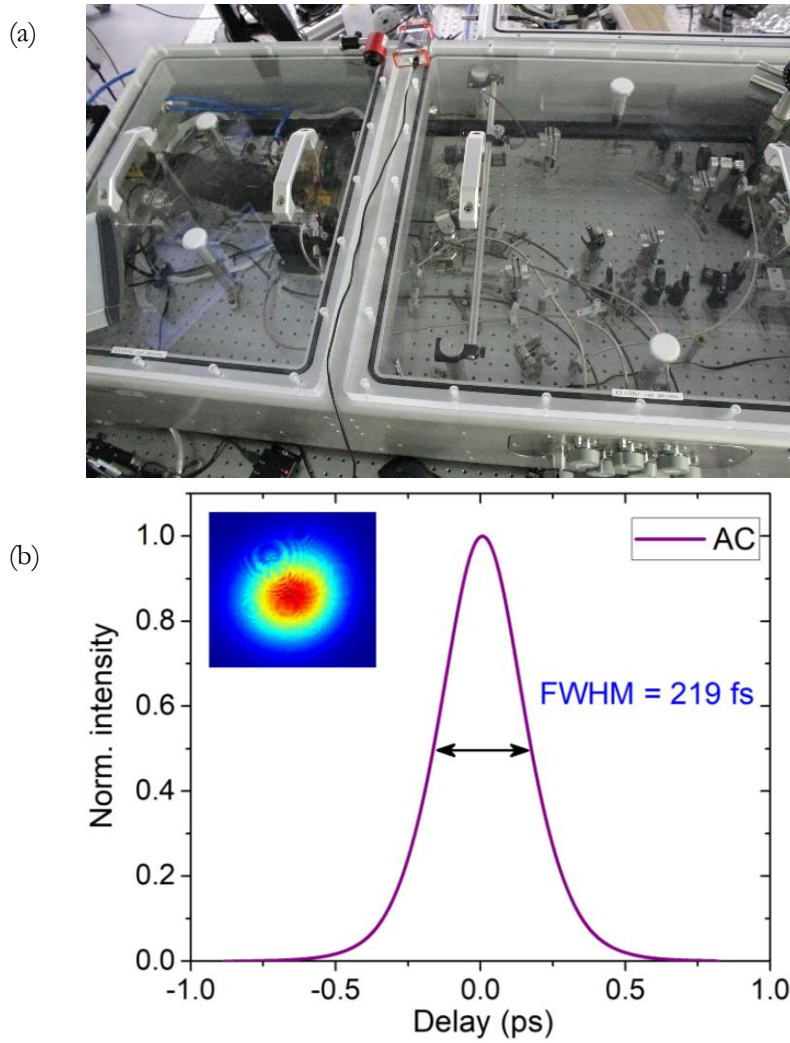
Figure 3.2 | Thin disk laser oscillator. a) Photograph of the laser oscillator. Lower right corner shows the remote knobs used to operate the position of the hard aperture, Kerr-medium, end-mirror, and half-wave plate. b) Autocorrelation measurement. The inset shows the intensity profile of the NIR beam output by the oscillator.

Relative intensity noise (RIN) measurements were taken by focusing the laser light on a similar InGaAs amplified photodiode. To this end, the laser beam was focused at the centre of the photodiode to minimize any noise coupling due to beam pointing drifts. This signal was recorded with a Fast Fourier Transform (FFT) spectrum analyser (Stanford Research, SR780) in four different bandwidth ranges (0-50 Hz, 0-800 Hz, 0-12.8 kHz, 0-102 kHz) to avoid low resolution at low frequencies, and the data was stitched together to obtain better resolution throughout the measurement bandwidth. The noise spectrum was normalized by the DC signal level to obtain the RIN spectrum S_{RIN} [in $Hz^{-0.5}$]. RIN measurements of short-time and long-time laser fluctuations are presented in Figure 3.3. The integrated RMS RIN value between the frequencies f_1 and f_2 for a given bandwidth was obtained by:

$$RMS\ RIN\ (f1, f2) = \sqrt{\int_{f_1}^{f_2} \left(S_{RIN}(f)\right)^2 df}$$

For the free-running oscillator, integrated RMS RIN from 1Hz to 102 kHz is 0.07 %, and it shows a typical 1/f noise behaviour. It is suppressed by more than a factor of two for the stabilized case, down to 0.03 % for the same bandwidth. The shape of the noise spectrum is modified due to the integrator parameters of the PI^{2}D controller, these parameters were adjusted for a minimum balanced detector noise for the lock-in detection at the chopping frequency (Section 4.5) . Long-term fluctuations were measured with a thermal power meter for 50 minutes, shown in Figure 3.3b. The sensitivity of the measurement here was limited by the noise of the thermal sensor used. The RMS relative to the mean is 0.097%. These sub-percent noise values play a central role in the experimental studies presented later on in this thesis.

These measurements were performed after the typical oscillator warm-up, to avoid any initial thermal drifts. The oscillator can typically be mode-locked after half an hour from switching on the system. It takes ~1 hour to reach thermal stability in mode-locked operation. To ensure long-term stability, various diagnostics[*] were used, so that any perturbation at a later stage could be diagnosed and fixed quickly. These includes monitoring the full width at half intensity maximum (FWHM) of Gaussian fit to the measured oscillator spectrum, pump spot on the thin-disk, and output power of the oscillator.
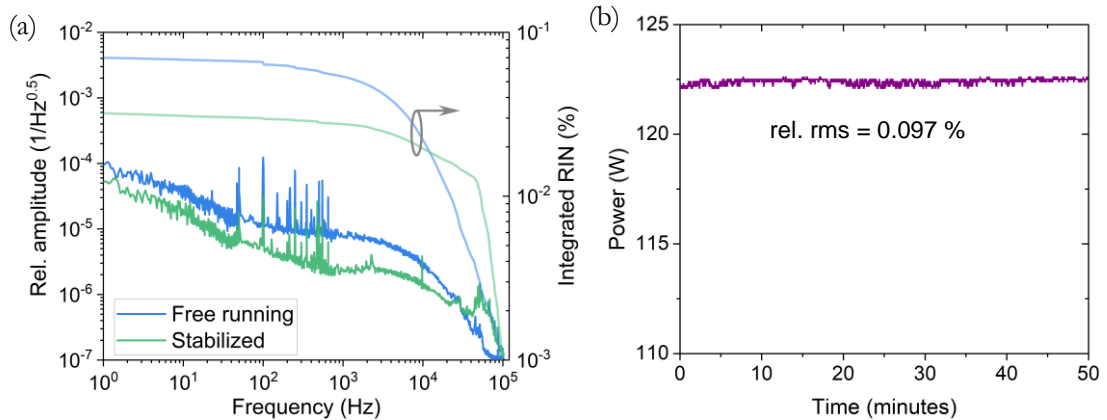
Figure 3.3 | Noise characteristics of the thin-disk oscillator. a) Relative intensity noise and integrated noise (in the bandwidth of 1Hz-102KHz) for free running and stabilized laser oscillator KLM-3. b) Power fluctuation measurements of laser oscillator KLM-3.

---

[*] At a later stage, a relative humidity control was installed *Wolfgang Schweinberger.*

To achieve further spectral broadening and compression, KLM-1 and KLM-2 rely on solid-core fiber based pulse compression, while bulk-based pulse compression was utilized with KLM-3, thanks to the availability of the higher pulse energies needed for bulk broadening.

3.1.2 Fiber-based pulse compression

Optical fibers with a solid core have been widely used to exploit self-phase modulation (SPM) to further broaden the laser spectrum[51–53], beyond the width achievable directly at the output of a modelocked laser. As mentioned earlier, Yb-doped gain media have lower gain bandwidth in comparison to the Ti:Sa medium, so that cavity-external techniques for spectral broadening are needed to access the few-cycle regime. Large-mode-area solid-core photonic crystal fibers offer spectral broadening by more than a factor of ten for laser pulses with several megawatts of peak power[54].

The laser beam is focused to the solid core of the photonic crystal fiber (PCF), and spectral broadening is achieved via SPM. Subsequently, negative group delay dispersion (GDD) is applied to obtain the compressed pulses. The material of the solid-core fiber puts an upper limit to the peak power at the input of the fiber facet, limiting the attainable spectral broadening. Figure 3.4 shows the spectral broadening obtained with a solid-core fiber for four different mode-field diameters (MFD), performed with KLM-1[55].
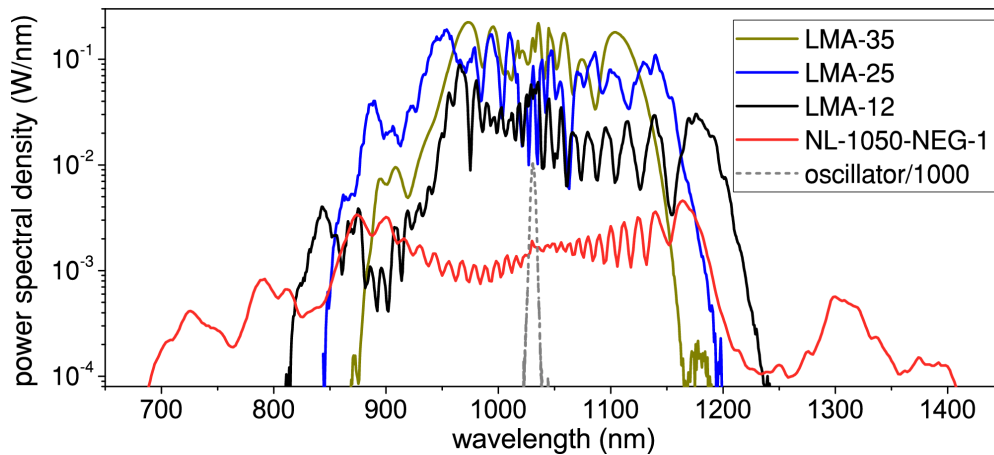
Figure 3.4 | Spectral broadening in photonic crystal fibers. Spectrum measured with an optical spectrum analyser (OSA), for four different fibers, is shown. LMA-35 has a MFD of about 26 µm, LMA-25 is of 20.9 µm, LMA-12 (also known as ESM-12) is of 10.3 µm and ANDi fiber (NL-1050-NEG-1) is of about 3 µm. Data taken from Ref. [55].

Table 3.2 | Broadening parameters of different PCF*.

Name	MFD (μm)	Broadening factor	Peak Irradiance (TW/cm²)	Peak power (MW)
LMA-35	26	19	0.73	1.93
LMA-25	20.9	24	0.97	1.67
LMA-12	10.3	28	1.3	0.55
NL-1050-NEG-1	3	51	2	0.07

The parameters of these fibers, along with the laser parameters used, are given in Table 3.2. With the given broadening factor, a Fourier transform limit (FTL) down to 10 fs can be achieved with LMA fibers. While the ANDi fiber with the smallest MFD leads to more than an octave-spanning spectrum, supporting sub-5-fs FTL. On one hand, this suggests the use of smaller MFD fibers to generate a broadband spectrum, while on the other hand the power spectral density is limited to a few mW/nm compared to ~200 mW/nm for the LMA fibers.

To couple the Gaussian laser beam into the fundamental fiber modes, a coupling lens is chosen in accordance with the equation[56]:

$$f = \frac{\pi D_{in} MFD}{4\lambda}$$

where f is the focal length of the input coupling lens, D_{in} is the diameter of the input collimated beam before the lens, and λ is the wavelength.

For the laser oscillator KLM-2, the setup for the fiber-based broadening is shown in Figure 3.5a. KLM-2 provides a pulse train of 100 MHz having a full width at half intensity maximum (FWHM) of 250 fs centred at 1030 nm, and an average power of 70W[48]. The pulses are sent to an 8-cm long LMA-35 PCF, followed by a set of dispersive mirrors, resulting in 20-fs FWHM pulses. To maintain stable operation of the system in the long term, only 40 W were sent to the fiber, resulting in 28 W of average power after the compressor being available for the experiment, corresponding to a compression efficiency of 70 %.

A Faraday isolator is used after the oscillator, before coupling to the fiber in order to avoid pulses reflected at the front facet of the fiber from coupling back to the oscillator, as this would interfere with the intra-cavity pulse and eventually force it out of mode-locking.

---

* Data taken from Ref. [55]

Figure 3.5b shows the normalized intensity of the generated broadband near-infrared (NIR) spectrum. These pulses are later used to drive the broadband pump optical parametric amplification (OPA) and intra-pulse difference frequency generation (IPDFG), presented in Section 3.2.2 and 0 respectively.

3.1.3 Bulk-based pulse compression

Although nonlinear pulse compression using a fiber-based setup offers good results in terms of broadening factors, beam quality, and throughput, the small coupling area makes fiber-based setups hard to align and limit their capability to handle beams with high average power and high peak power, due to material threshold. Another technological limitation of the fiber-based approach comprises of instabilities due to input beam pointing. Such instabilities lead to increased intensity noise as well as distortion in the output beam profile[57]. These limitations can be avoided in a bulk based broadening scheme to a certain extent.

In contrast to a single-pass geometry through the bulk medium, a multi-pass cell (MPC) can be utilized[58,59]. Furthermore, these MPCs can be cascaded to exploit moderate nonlinearities in each cell. In our setup, three Herriot type MPCs serve as a broadening setup, as shown in a schematic Figure 3.6a. The input beam was mode matched before entering the MPC so that a single broadening medium could be used for multiple passes in a compact fashion. Out of the available > 100 W of power, only 100 W were sent to the broadening stages (for a stable long-term operation). Each of the three stages comprises an antireflection-coated fused silica nonlinear broadening medium, and curved dispersive mirrors designed to compensate for the material dispersion of the broadening medium.

The first two stages have 1-inch dispersive mirrors with a radius of curvature (ROC) of 300 mm and a mirror separation of 560 mm with 12 passes, while the third stage has dispersive mirrors with a ROC of 500 mm and a separation of 894 mm with 38 passes. After each broadening stage, the pulses were compressed by a set of dispersive mirrors. This resulted in compressed pulses with durations of 84 fs, 43 fs, and 16 fs respectively after each stage, with an average power of 82 W, 74 W and 60 W. Figure 3.6 b-c shows the retrieved spectrum and pulse obtained with a second harmonic frequency-resolved optical gating (FROG) measurement. The retrieved spectrum shows a nice agreement with the spectrum measured using an optical spectrum analyser (OSA). This setup was built by *Kilian Fritsch*[49] and was slightly modified and optimized over the course of several months for stable operation over the long term, as required for the field-resolved measurements presented in Chapter 5.
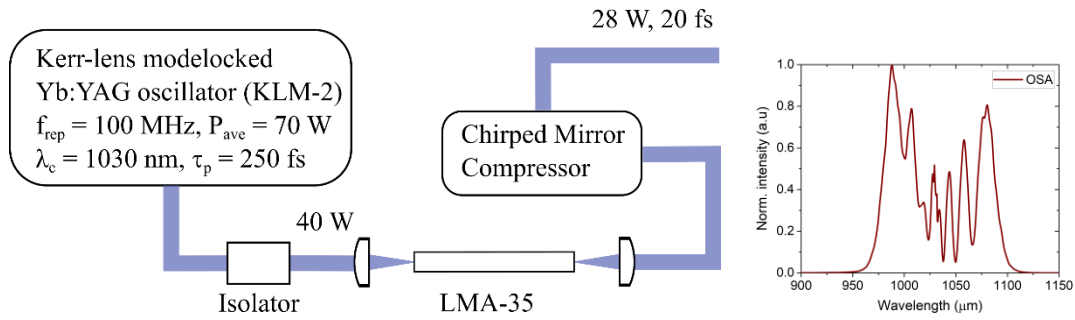
Figure 3.5 | Fiber-based spectral broadening. Schematic diagram of the broadening setup. A faraday rotator is used before the fiber to avoid any back reflection going back to the oscillator. Right panel shows the spectrum of the broadband NIR in LMA-35.
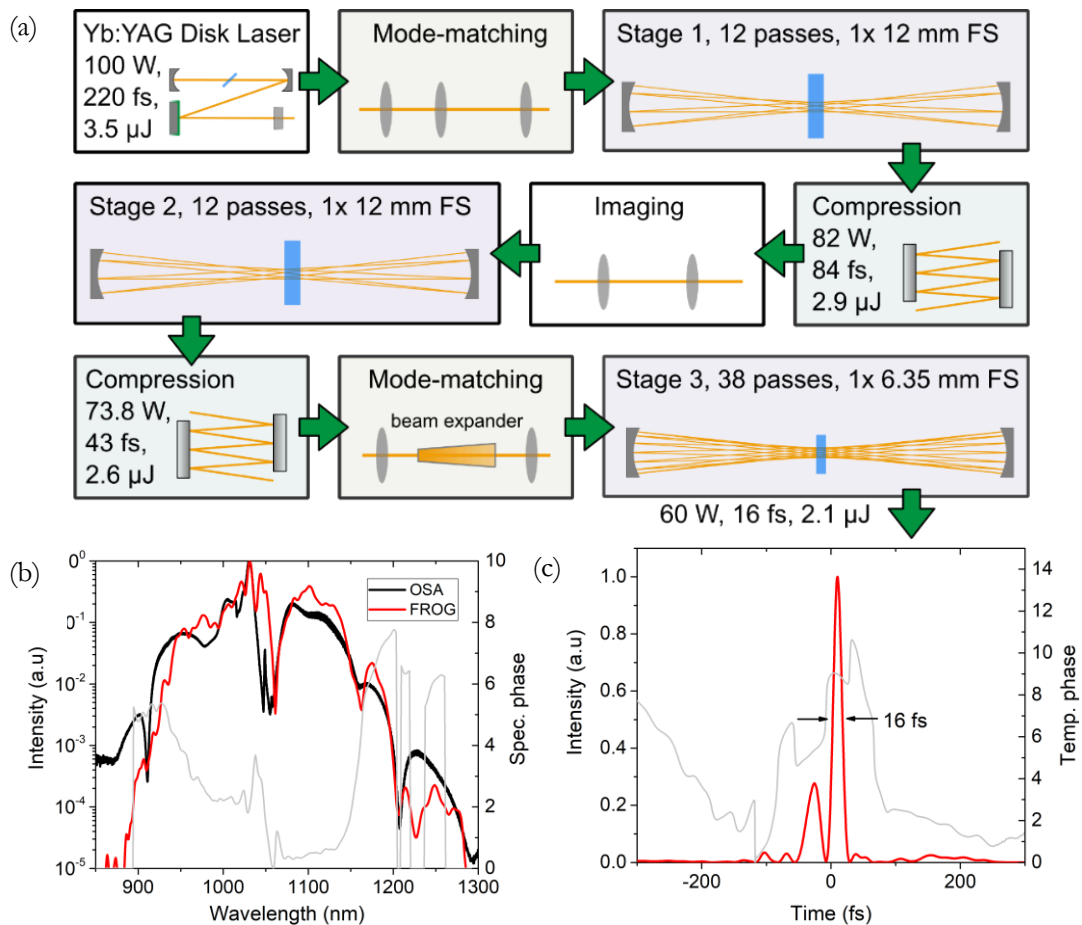
Figure 3.6 | Bulk-based spectral broadening scheme. a) Schematic of the multi-pass broadening scheme. The oscillator and the first two broadening stages were operated in a closed environment, while the third broadening stage was operated in vacuum. b) Spectrum measured with OSA and retrieved spectral intensity and phase from FROG. c) Temporal intensity and phase. Sketch of setup is adopted from Ref. [49]
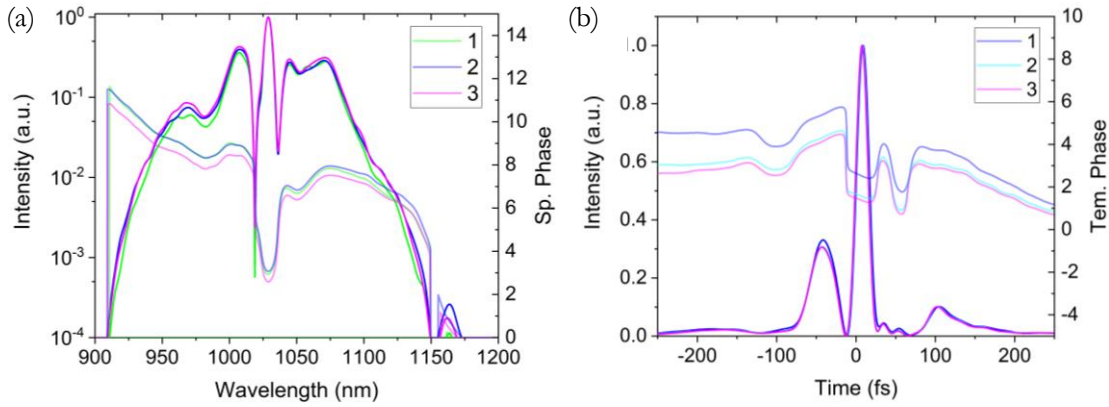
Figure 3.7 | Reproducibility measurements for broadband NIR. Retrieved spectrum and pulse from a FROG measurement for three consecutive days.

To further characterize the system, a series of FROG measurements was done on subsequent days at a moderate vacuum level. Figure 3.7 shows that the day-to-day reproducibility was good. The fluctuations in the oscillator power also directly translate into the nonlinear broadening. The residual oscillator power and NIR power were measured with a thermal power meter for 30 minutes, since this NIR would be used further for the MIR generation, where the wings of the driving NIR plays a central role. A long-pass filter at 1100 nm (Thorlabs, FEL1100) was used for measuring NIR power fluctuations. The oscillator power measurement was limited by the digitization of the thermal sensor used, nevertheless a clear correlation could be observed, as shown in Figure 3.8 (a correlation with MIR power is shown in Figure 3.26). This reinforces the importance of the active stabilization of NIR presented in Section 3.1.1. A vacuum level of 10 mbar was maintained for the third stage, while both power meters were placed in air.
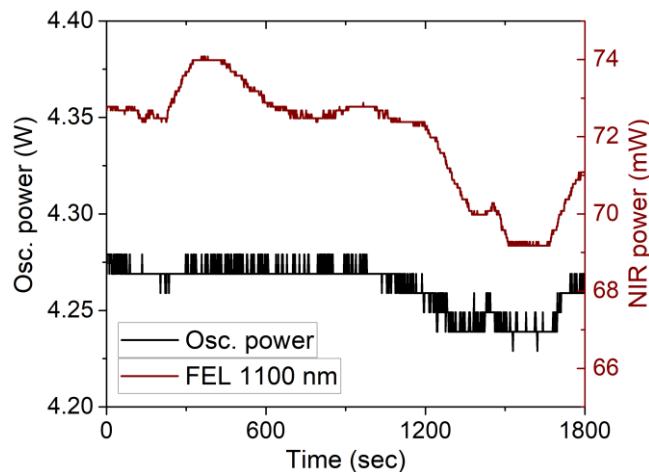
Figure 3.8 | Correlation in the power fluctuations of the oscillator and at the wing of the broadened NIR.

The effect of intensity noise was also measured for short-term fluctuations, as shown in Figure 3.9, as per the procedure presented in Section 3.1.1. The measurements were

performed for the oscillator, broadband NIR, and also for the wing of the NIR, by using a short pass filter at 925 nm (this filter is chosen in accordance with the spectral filter used in electro optic sampling (EOS), presented in Chapter 5).
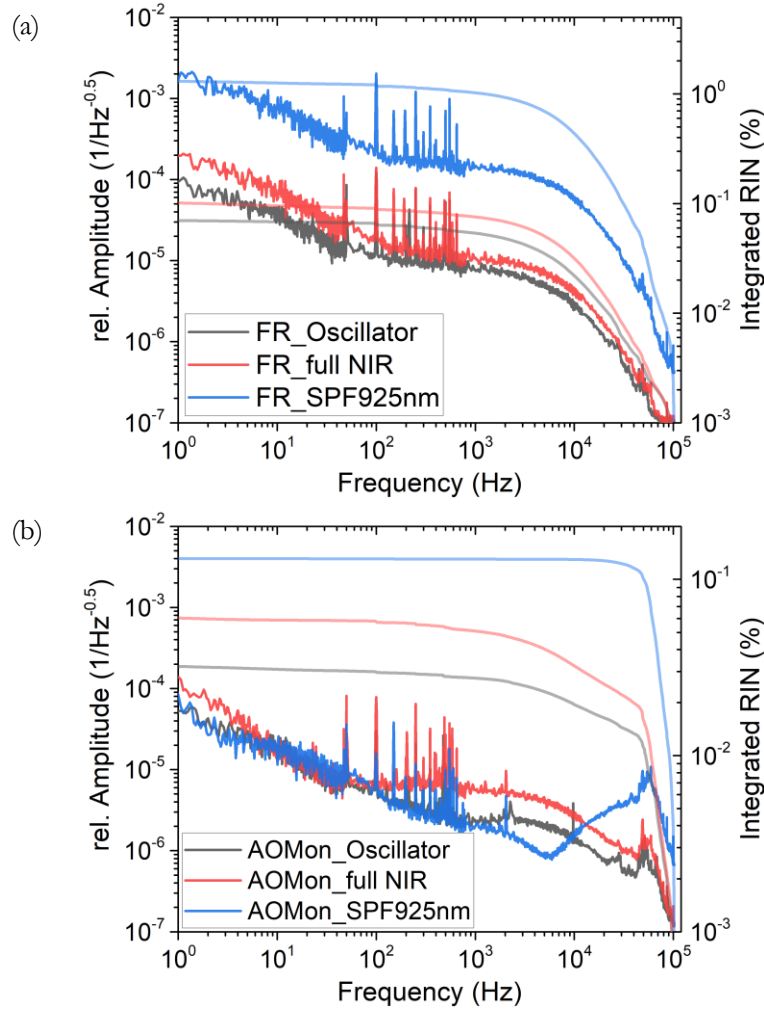
Figure 3.9 | Relative intensity noise measurements for the oscillator, full broadband NIR and spectral wing of the NIR. In the a) free-running case and b) stabilized case.

For a free-running mode, the oscillator has a relative RIN of 0.07 %, broadband NIR has 0.1 %, and the spectral wing beyond 925 nm has 1.3 %. The reason behind the higher RIN value for the full broadband NIR was not clearly understood. This result is in contrast to the RIN measurements for bulk compression in air[60] and for PCF based compression[50], while an increase in the RIN for the compressed NIR has been reported for a gas-filled Kagome-type hollow-core photonic crystal fiber in Ref. [61,62] The increase in RIN for the spectral wing, however, is expected, as reported in Ref. [50,63]. Also, the increase in RIN for the spectral wing is a factor of 13 higher than the full broadband NIR RIN, which is almost the same as the broadening factor achieved with the setup. For the stabilized case, where the AOM was switched ON, integrator parameters are chosen to minimize the noise at lower

frequencies for the blue spectral wing of the NIR. This corresponds to a 0.03 % integrated RIN for the oscillator, 0.06% for the full broadband NIR, and 0.13 % for the NIR spectral wing. For this chosen spectral wing of NIR, RIN suppression by a factor of ten is achieved.
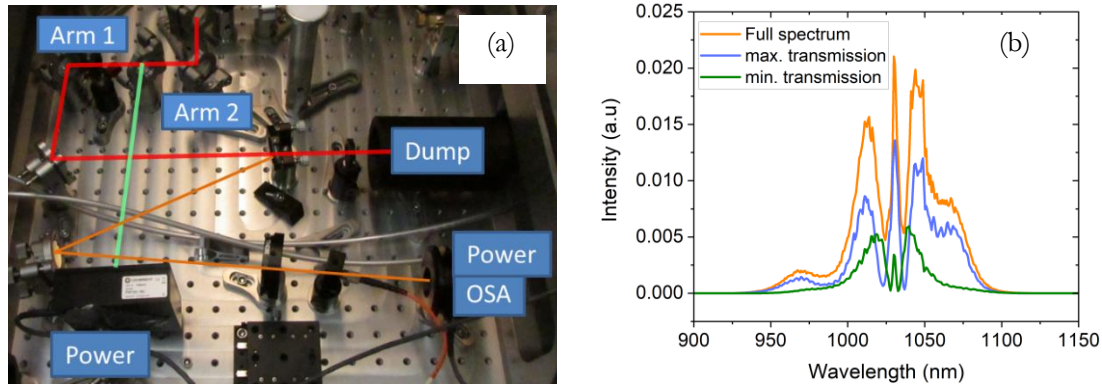
Figure 3.10 | Polarization characterization of the MPC output. a) Picture of the setup b) OSA measurement for the full spectrum, minimum and maximum transmission through the polarizer

The beam goes to multiple reflections in the MPC in a circular fashion, exploiting the SPM nonlinearity in the broadening medium. The polarization at the output of the third MPC was analyzed using a simple setup (shown in Figure 3.10). A 45° custom-designed 50-50 beam splitter was used to the divide the beam into two arms, for characterization. The reflected beam was directed to a thermal power meter. The transmitted beam was picked by a FS wedge and analyzed using a wire-grid linear polarizer (Thorlabs, WP25M-UB). The spectrum and power after the polarizer were measured with an OSA and a thermal power meter. At an input power of 100 W from the oscillator, the beam had a de-polarization of 40%, and almost similar spectral components in each arm, as shown in Figure 3.10b. The polarization was manipulated by a combination of polarization optics. A Glan-Taylor polarizer was used to clean the polarization after the oscillator. A half-wave plate and a quarter-wave plate were also placed after the second and third MPCs respectively. The rotation of the two wave-plates was chosen such that both arms have the same power on increasing the input power from the oscillator. This gives an extinction ratio of less than 2% for an input power up to 100 W, as shown in Figure 3.11. The percentage is calculated by taking the ratio of the minimum to maximum transmitted power through the polarizer. A clean polarization is a necessity for the IPDFG presented in Section 0.
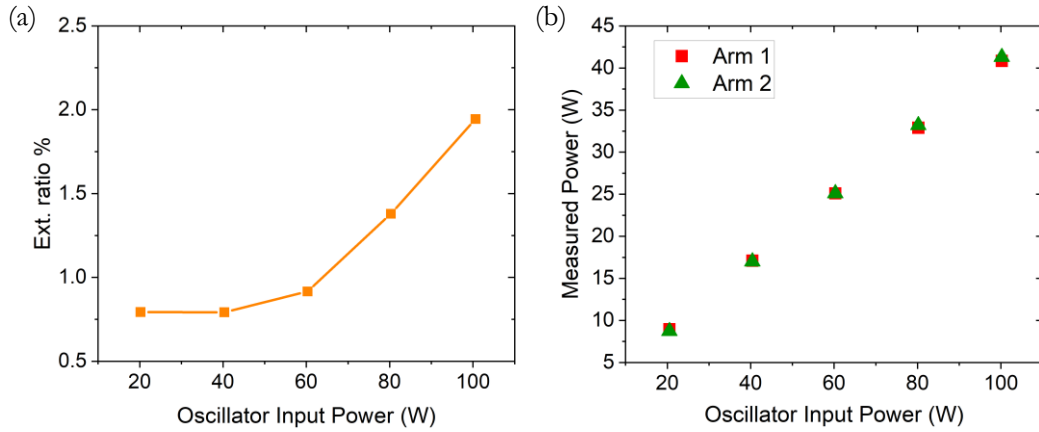
Figure 3.11 | Polarization extinction ratio measurement as a function of input power to MPC setup. a) Extinction ratio measurement, and b) measured power in each arm as a function of input power. The measurements were performed in air at atmospheric pressure.

3.2 Mid-infrared generation

Optical parametric processes offer a robust way for the generation of broadband and tuneable mid-infrared radiation. In these processes, the energy and momentum of the interacting waves remain conserved. In this thesis, frequency down-conversion is achieved via three-wave mixing, as optical parametric amplification (OPA) and difference frequency (DFG). Figure 3.12 shows a typical sketch for such schemes. In OPA, a strong beam, commonly termed as the pump beam with frequency ω_p, interacts in a thick $\chi^{(2)}$ crystal with a weak beam, termed as the seed beam with frequency ω_s, resulting in a third beam, termed as the idler beam with frequency ω_i. Here the weak seed beam undergoes a coherent build up process in a thick $\chi^{(2)}$ crystal, resulting in high conversion efficiencies. On the other hand, DFG processes utilize a strong seed beam in a relatively thin $\chi^{(2)}$ crystal, so that broadband idler can be generated at the cost of a reduced conversion efficiency[29,64]. The mathematical description of these processes can be found in Ref. [25,64,65].

Briefly, during an OPA process, a pump photon of frequency ω_p is absorbed by a virtual level in the nonlinear crystal, and two photons, one at the signal frequency ω_s and another at the idler frequency ω_i are emitted. In this process, both energy conservation $\omega_p = \omega_s + \omega_i$ and momentum conservation $k_p = k_s + k_i$ are fulfilled. The phases of the three waves are linked by $\varphi_p - \varphi_s - \varphi_i = constant$. Both OPA and DFG results in a passively stabilized CEP. The momentum conservation, also known as the "phase-matching condition", is to be fulfilled in the nonlinear crystal for efficient energy transfer between the three interacting beams. In addition, the nonlinear crystal needs to be non-centrosymmetric, transparent, having good optical quality and a high nonlinear coefficient. Although a large number of nonlinear crystals are available, only a few crystals can be efficiently utilized for a given laser system. Two different schemes for OPA that have been realized using KLM-1

and KLM-2 are presented in the next section, following which an intra-pulse difference frequency setup based on KLM-3 has been described.
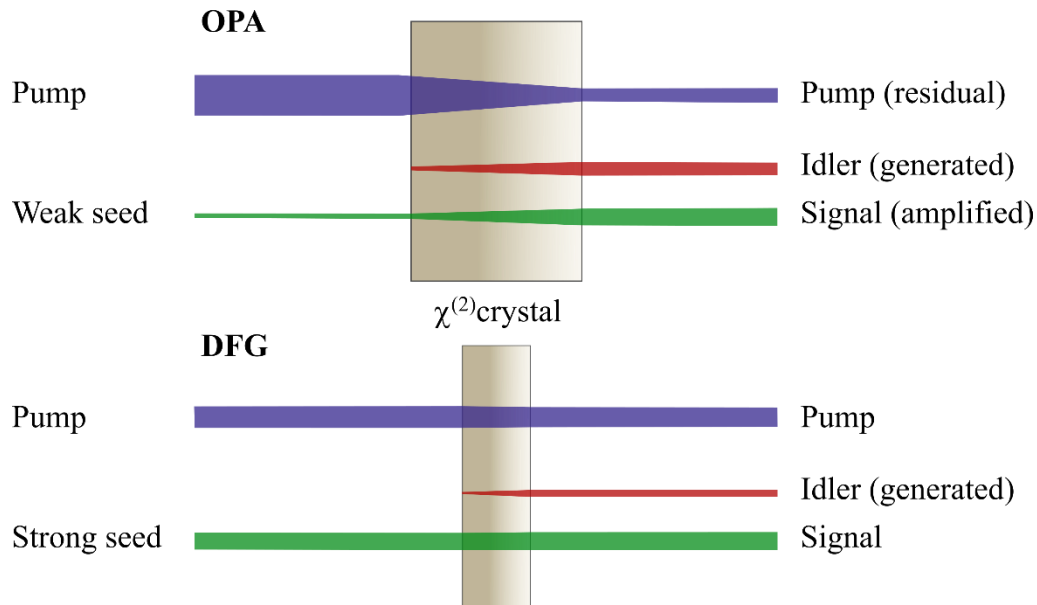
Figure 3.12 | Sketch of frequency down-conversion process via three-wave mixing. Figure is inspired by Ref. [64]

3.2.1 Narrowband pump OPA

In this setup, KLM-1 serves as the front-end oscillator delivering ~ 50 W of average power, 230 fs pulses at a repetition rate of 37.5 MHz. The output of the oscillator directly serves as the pump source, while the seed is generated in an ANDi fiber[*] having a mode field diameter of about 3 μm. A dichroic mirror was used as a beam combiner for pump and seed, reflecting only the long wavelengths of the seed spectrum.

The transmitted pump and long wavelength of seed beam were focused on a nonlinear crystal in a collinear fashion, such that the generated MIR beam is free from spatial chirp. The polarization of each of the two beams was optimized for higher MIR output. The setup is shown in Figure 3.13a, and the design parameters are described in detail in Ref [29]. Properties of the generated MIR beam, separated by a beam splitter, were evaluated using a Fourier transform infrared spectrometer (FTIR) and a thermal power meter.

---

[*] This setup was built in High-repetition-rate Femtosecond Source (HFS) group, by *Marcus Seidel*. I built the LGS based OPA setup presented here, and supported OPA noise characterization presented in Ref. [29]
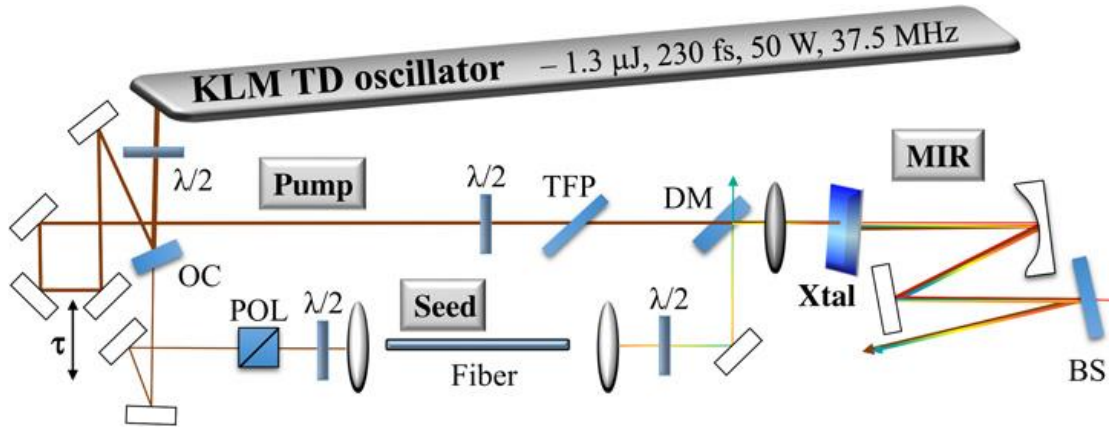
Figure 3.13 | Sketch of OPA setup based on KLM-1. $\lambda/2$, half-wave plate; OC, output coupler; POL, polarizer; TFP, thin-film polarizer; DM, dichroic mirror; Xtal, LGS crystal; BS, beam splitter. Figure is taken from Ref.[29]

The continuum generated in the ANDi fiber is very broadband and fairly symmetric, as shown in Figure 3.14. An output coupler transmits 3% of the power from the oscillator to the seed arm. The polarization is cleaned in front of the fiber to suppress cross-phase modulation. At full-power operation, 1.5 W were sent to the fiber. At this power, the broadening is almost saturated, as shown in Figure 3.14. The top axis of the plot of the seed spectrum shows values of the difference wavelength (λ_i) that could be generated, considering the central pump wavelength (λ_p) to be 1030 nm, for the seed wavelengths (λ_s) displayed along the bottom axis, such that $\lambda_i^{-1} = \left|\lambda_p^{-1} - \lambda_s^{-1}\right|$. These beams were focused on lithium gallium sulphide (LGS) crystal for type I phase matching. The availability of broadband seed allows for tunability of the central wavelength of the generated idler beam, at the cost of phase matching efficiency. For the generation of shorter wavelengths, the phase-matching conditions become strict and a significant drop in the idler was observed.
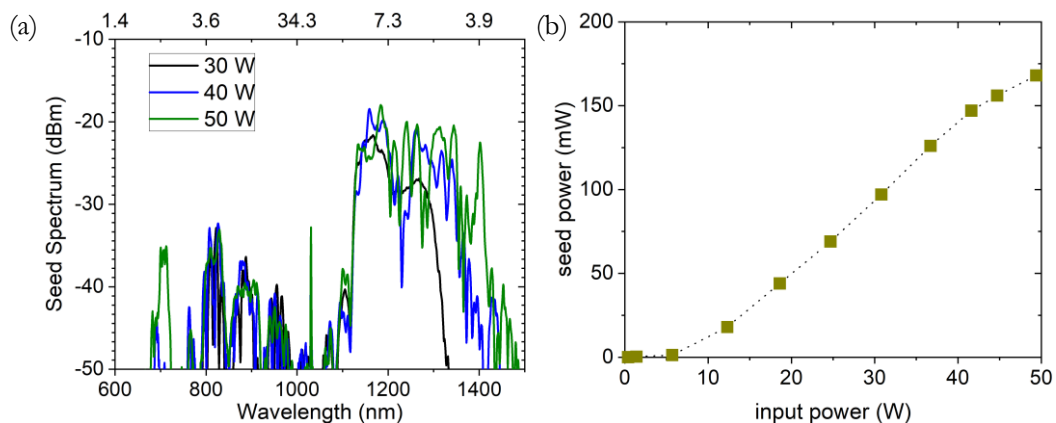
Figure 3.14 | Seed spectrum and power for narrowband pump OPA. Measured a) spectrum and, b) power of the seed beam after dichroic mirror at different input power from the oscillator.

(a)

(b)
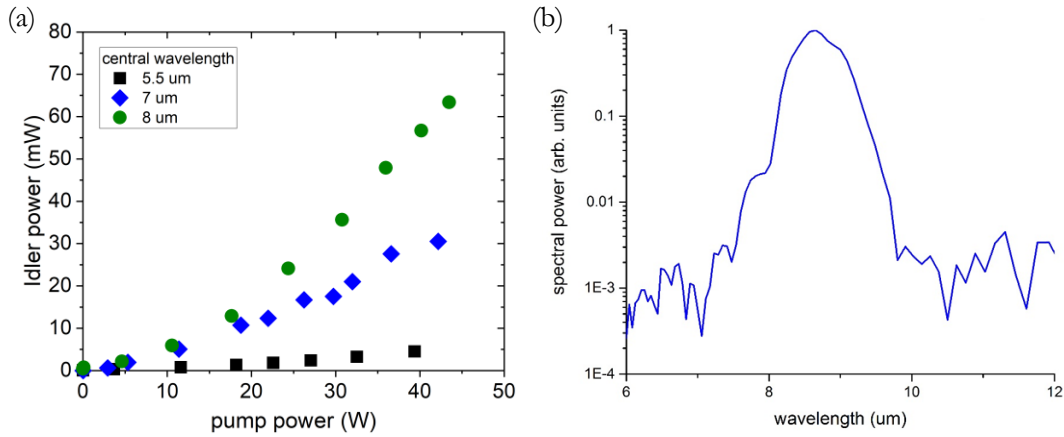
Figure 3.15 | Generated idler power and spectrum in narrowband pump OPA. a) Measured idler power for different pump powers. b) Measured spectrum of the idler beam at a central wavelength of 8.7 μm.

3.2.2 Broadband pump OPA

In order to explore the generation of broadband idler radiation and its noise characteristics, the setup was designed to use a broadband pump source to drive the OPA. The frontend shown in Figure 3.5 was utilized for this purpose. For an input of 40 W to the fiber compressor, 20-fs NIR pulses with an average power of 28 W are generated. A small fraction is picked off with an uncoated fused silica wedge, and used as a probe beam for electro-optic sampling. An uncoated sapphire wedge reflects 7% of the incoming beam for the seed generation, resulting in 22 W of power being available for use as the pump beam. The setup is sketched in Figure 3.16.
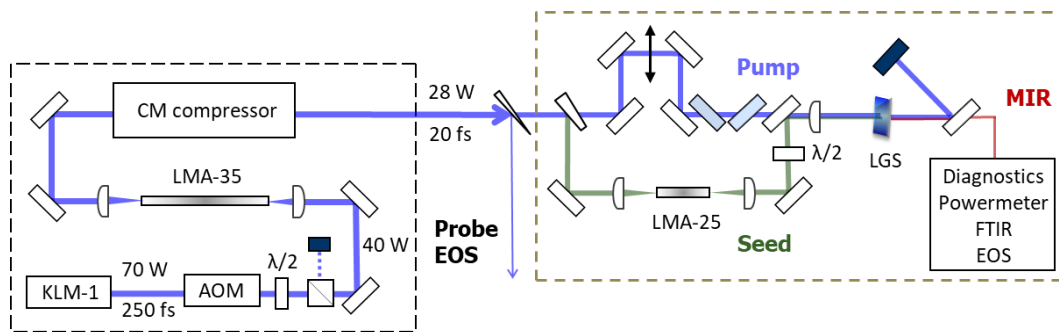
Figure 3.16 | Sketch of the broadband pump-driven OPA setup. The frontend delivers 20 fs pulses with an average power of 28W, out of which 22W were available for utilization as a pump beam.

For the seed generation, a 20-mm long second photonic crystal fibre with a mode field diameter of 20.9 μm was used. The fibre was placed on a fibre clamp (Thorlabs, HFF003) and a 50-mm lens placed on a three-dimensional stage was used to focus the beam into the fiber. An off-axis parabolic mirror was used to collimate the beam. A fiber of such

a small size is difficult to handle and align. A picture of the fiber setup, the front facet of the cleaved fiber, and the output beam profile are shown in Figure 3.17.
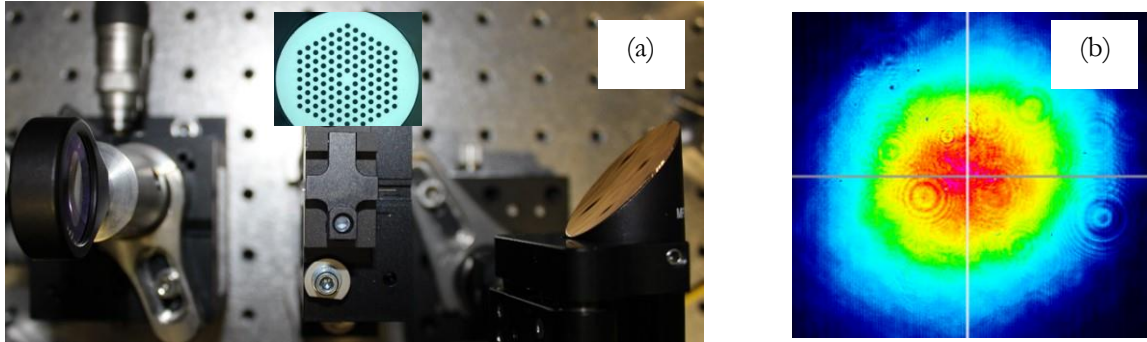
Figure 3.17 | Seed generation in photonic crystal fibre. a) Picture of the setup, 20-mm long fibre was placed on a fibre groove and a plano-convex lens on a 3D stage was used to focus the NIR beam into the fibre. An off-axis parabolic mirror was used collimated the beam. Inset shows the front facet of the fibre, b) output beam profile after collimation.
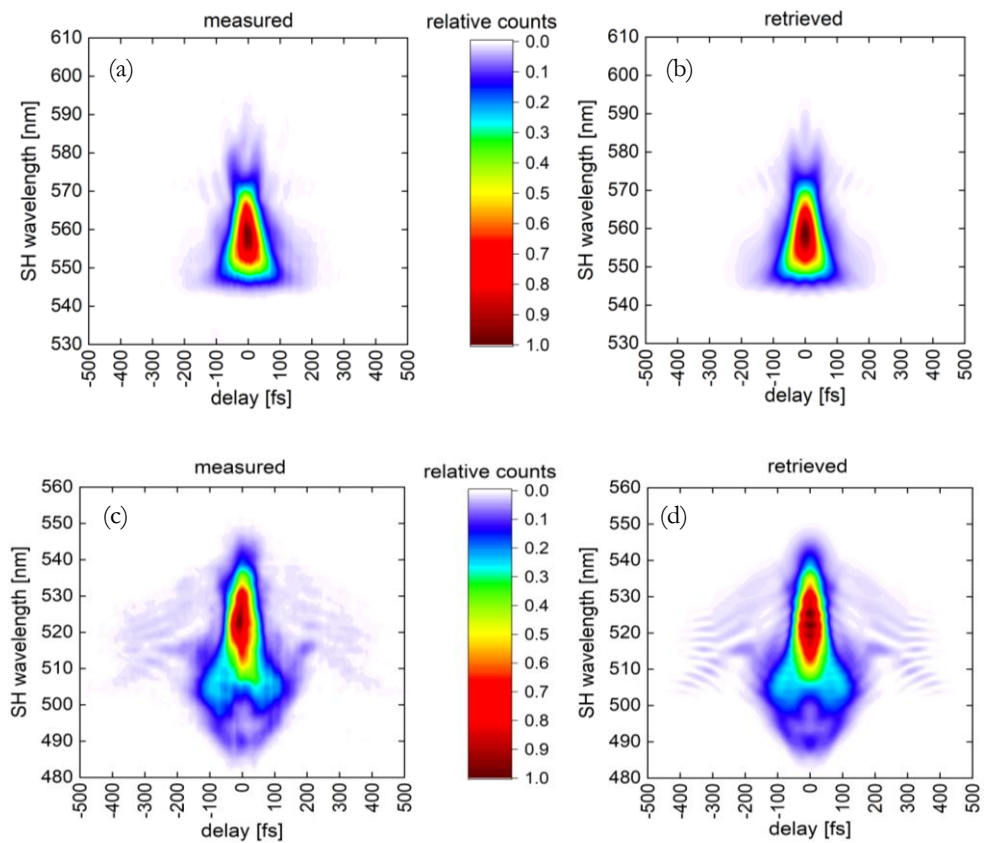
Figure 3.18 | FROG measurements of seed and pump beams. a) Measured and, b) retrieved trace of the seed beam. c) measured and, d) retrieved trace of the pump beam.

The seed beam was not compressed after the fibre. A second harmonic FROG measurement was done to characterize the seed beam, giving out a pulse duration of 59 fs. The pump beam was transmitted through a half-wave plate (HWP) and Glan-Taylor Calcite Polarizer (Thorlabs, GT10-B), used to control the pump power sent for the OPA. As the pump beam of 20 fs would lead to overlap of limited frequency components, resulting in gain narrowing and lower pulse energy[23,66]. In order to increase the pulse overlap and interaction length, pump pulses were stretched to a pulse duration of 49 fs using two 6-mm thick Infrasil windows additionally so that a better overlap between the seed and pump beam could be achieved in the nonlinear crystal. Figure 3.18 shows the measured and retrieved FROG traces for the pump and seed beams. In principle, if broadband phase matching is satisfied, the pulse duration of an OPA does not depend on the pulse duration of OPA. But to ensure the temporal overlap, the seed pulse duration should be at least comparable to the pump pulse duration[66].
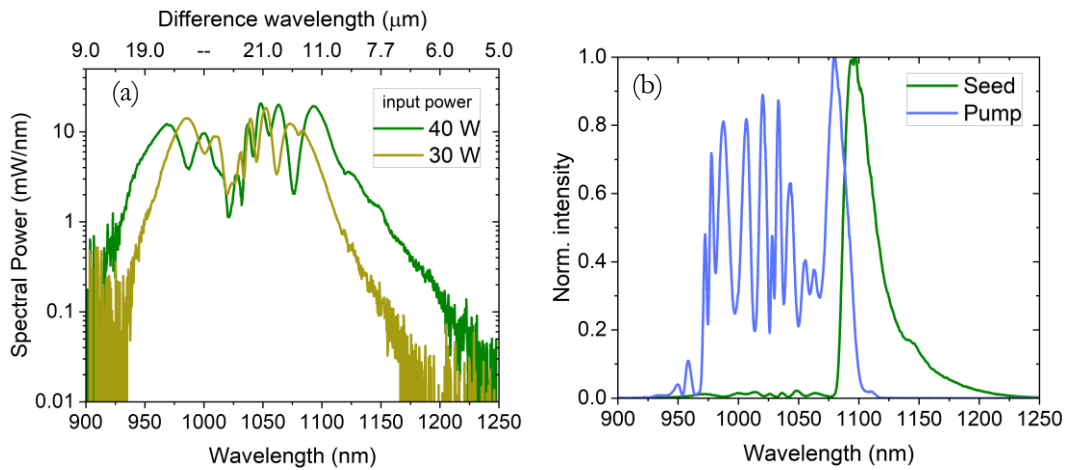
Figure 3.19 | Spectrum of the seed and pump beam for broadband pump OPA. a) Spectral power of the seed beam for different input power sent to the frontend fibre. b) Normalized pump and seed spectrum after the beam combiner, used for the OPA. The pump beam in transmission and seed beam in reflection, both have sharp wavelength cut-off due to the dichroic mirror used for combining both beams.

Figure 3.19a shows the evolution in spectral power of seed beam for two input power at the front end LMA-35 fibre. For an input power of 30 W and 40 W, average powers of 1.16 W and 1.56 W were sent to the seed LMA-25 fibre, respectively. The top axis shows the difference wavelength that corresponds to these seed wavelengths, considering a central wavelength of 1030 nm for the pump seed. The pump beam with an average power of 22 W goes to a delay stage, used for optimization of the temporal overlap. A dichroic short pass filter with a cut-off wavelength of 1100 nm (Edmund Optics, #86-691) was used as a beam combiner for the two beams, such that the pump beam below the cut-off wavelength is transmitted and the seed beam above the cut-off wavelength was reflected from the filter.

As, the filter response was polarization-dependent, both the p-polarized pump beam and s-polarized seed beam see slightly different filter cut-off wavelength as shown in Figure 3.19b.

These beams were focused on an LGS crystal for MIR generation. It is important to mention here that the purpose of this proof-of-principle experiment was to study the bandwidth and noise characteristics of the generated MIR, and to have enough MIR power to characterize it with EOS. It has been found that a thicker LGS crystal seems to suffer damage at lower intensities[29], compared to the damage threshold reported in the literature for thinner LGS crystals[26].
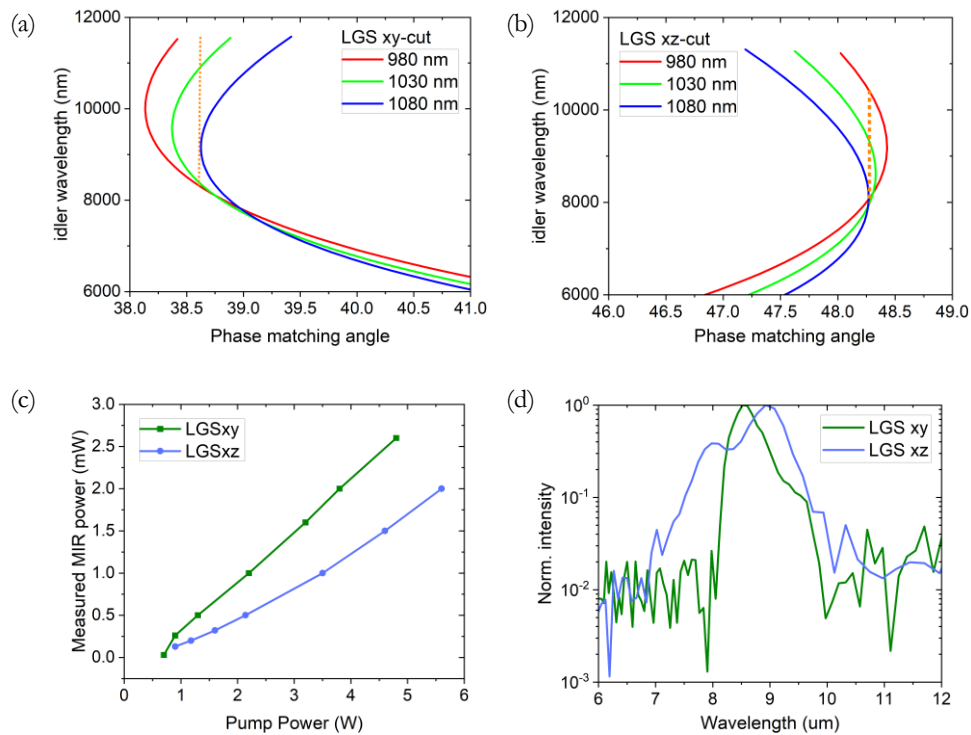
Figure 3.20 | Phase matching for LGS crystal. Calculated idler wavelength for a) xy-cut crystal, b) xz-cut crystals for different pump wavelengths. Experimental results for the c) measured MIR power as a function of pump power d) measured MIR spectrum with FTIR for xy-cut and xz-cut LGS crsytal.

Moreover, in the course of these experiments, no replacement for the LGS crystal was available[*]. The OPA in this setup was driven only at low pump powers. Two LGS crystals were used in these experiments, an xy-cut LGS ($\theta = 90°, \phi = 38.6°$) which allows for type-II phase matching and an xz-cut LGS with ($\theta = 48.3°, \phi = 0°$) which allows for type-I phase matching. For a central wavelength of 1.03 μm, xy-cut LGS crystals have a higher nonlinear coefficient ($d_{eff} \approx 6.0 \, pm/V$) compared to xz-cut LGS crystal ($d_{eff} \approx$

---

[*] The LGS crystals used in the experiments were ordered from the company ASCUT, and their delivery time for the new crystals is rather quit long, more than three months typically.

$-4.6\,pm/V$). For both crystals, phase matching calculations were done using SNLO[67], considering three different pump wavelengths of 980, 1030, 1080 nm, which correspond to seed wavelengths of 1099, 1163, and 1227 nm respectively, for an idler generation of 9000 nm. The phase-matching curves are shown in Figure 3.20 a,b. The turning points of these curves indicate that a very broadband phase-matching can be achieved at the respective phase-matching angles for pump wavelengths around 1 μm.

After the LGS crystal, the beams were separated by using a custom in-house designed dichroic filter that reflects the pump and seed beams and transmits the generated MIR, which was collimated by an off-axis gold parabolic mirror. The MIR beam after collimation goes to the diagnostics that measure the power with a thermal power meter and the spectrum with an FTIR spectrometer. Both of the findings predicted by SNLO were observed in the experiment as shown in Figure 3.20 c,d. While type-II phase matching resulted in a higher MIR power, a broader MIR spectrum was generated by type-I phase matching.
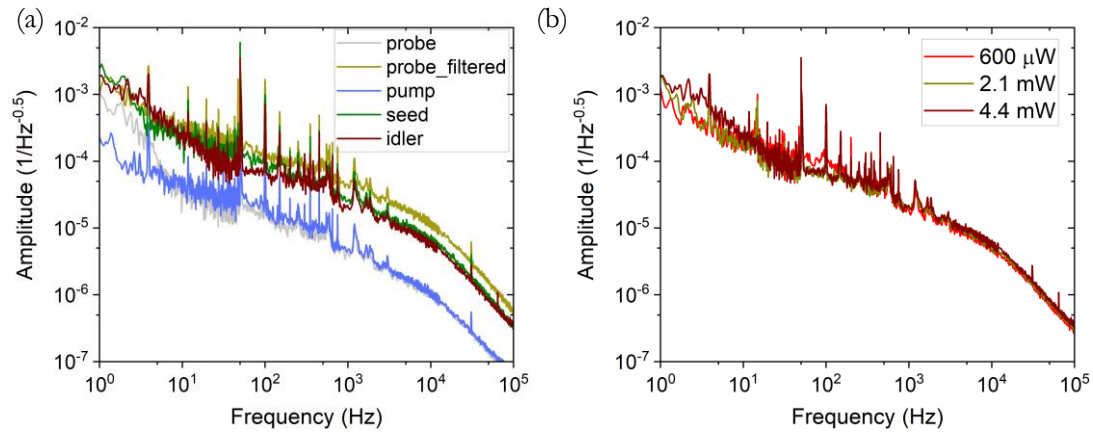
Figure 3.21 | RIN measurements of the OPA beams. a) Measured RIN of the full probe beam, probe filtered with a bandpass filter of 1100 nm, seed, pump, and idler beams. b) RIN for different idler powers.

The noise characteristics of OPA were analysed by performing relative intensity noise measurements, and are shown in Figure 3.21. The probe and pump beams (grey and blue curve) exhibit similar noise characteristics, since both originate from the first fibre compressor. The seed beam (green curve) exhibits a higher noise than the pump beam. The noise of the idler beam (brown curve) almost follows the seed noise. The RIN of the probe beam was also measured with a bandpass filter (Thorlabs, FB1100-10) with a central wavelength of 1100 nm (±10 nm). Both the seed and the red part of the probe beam (yellow curve) have higher noise since these beams are form only a part of the full spectrum, and the fact that the outer wings of broadened components have higher noise has been reported in literature[50,63]. Under these conditions of operation, no change in the RIN of the idler beam was observed on increasing pump power (shown in Figure 3.21b), corresponding to

measured idler power levels of 0.6, 2.1 and 4.4 mW. The idler pulses were also characterized using EOS, and are presented in Section 3.3.

3.2.3 Intra-pulse difference frequency generation

Intra-pulse difference frequency generation (IPDFG) relies on mixing the different frequency components within a single broadband driving pulse. It is a slight variant of the widely used technique known as inter-pulse DFG or simply DFG, where the mixing frequency components come from two different beams. In IPDFG, the nonlinear optical mechanism is a similar effect reported in terahertz generation as optical rectification. As, both the pump and seed photons come from the same pulse, the need for temporal and spatial overlap are eliminated, which are required in inter-pulse DFG and OPA. The idler photons are generated by the mixing of the outer wings of the driving pulse, so that the idler bandwidth is defined by the available spectral width of the driving pulse and by the phase-matching conditions of the nonlinear crystal. In addition, the generated idler pulse gets a fixed phase, due to the subtraction of the equal phase of the pump and seed spectral components of the driving pulse[23,24]. All these factors combined lead to some unique features in IPDFG including optical synchronisation, a compact experimental setup, intrinsically locked CEP, and broadband idler generation.

MIR generation via IPDFG was realized for both NIR sources frontend presented in Section 3.1.2 and 3.1.3. The MIR generation from NIR driving beam based on fiber-based compression is described briefly here, while a detailed description is presented for the bulk-based compression setup. As the later source was used in the final configuration of the field-resolved spectrometer (Chapter 5).
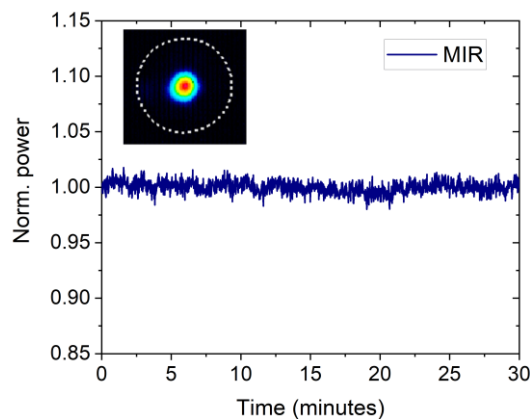
Figure 3.22 | Measured MIR power for 30 minutes. The slow fluctuations are due to temperature fluctuations of cooling water. Inset shows the beam profile of the NIR focus at the LGS crystal.

The NIR frontend (see Figure 3.5) provides 20-fs pulses with an average power of 28 W, and an uncoated fused-silica (FS) wedge reflects a small portion of this beam for the

electro-optic detection setup, presented in Section 4.4. The transmitted NIR pulses were focused onto the LGS crystal for Type-I phasematching with a 250-mm focal-length lens for IPDFG. The focusing was chosen such that the peak intensity at the 75-μm focus (l/e2-intensity-radius) was 1.38×10^{11} W/cm² , which is an almost an order of magnitude below the intensity damage threshold[26]. This circumvents thermal effects in the LGS crystal and provides long term stability of the MIR power. Figure 3.22 shows the measured MIR power normalized to the mean, inset shows the NIR focus at the DFG crystal. The generated MIR beam was separated from the driving NIR beam, and detected via electro-optic sampling presented in Section 4.4.

The broadband pulses presented in Section 3.1.3, based on bulk-based compression were utilized for the MIR generation. Since metallic mirrors are prone to damage at such high levels of power and pulse energy, in order to steer the beam for IPDFG without adding any dispersion, custom designed 45° high reflective mirrors (HR502) were used. The reflectivity and group delay dispersion of these mirrors for s-polarization are shown in Figure 3.23. The design simulations suggest a slightly different GDD behaviour for an odd and even number of layers.
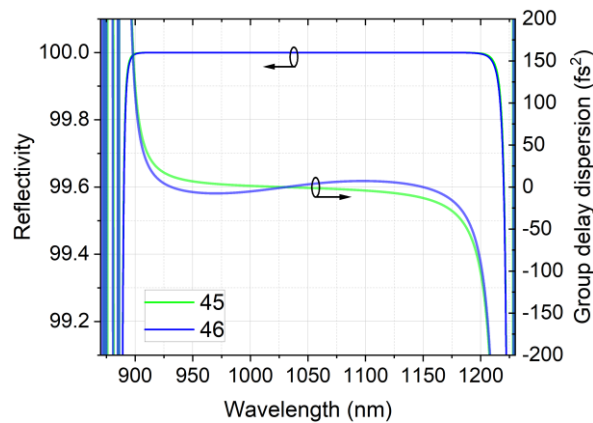
Figure 3.23 | Design curves for reflectivity and group delay dispersion of customized HR mirrors for 45 and 46 layers. (Courtesy: *Michael Trubetskov*).

The oscillator and the first two MPC were in closed chambers, while the third MPC and the IPDFG were operated at a few millibar vacuum level. The setup is sketched in Figure 3.24. For an input power of 100 W from the oscillator, the third MPC provides 16 fs pulses with an average power of 60W, corresponding to a pulse energy of 2.1μJ. Each MPC has an additional set of dispersive mirrors for optimized compression. These NIR pulses were focused down to 330-μm ($1/e^2$-intensity diameter) using a 700-mm focusing lens, corresponding to a peak intensity of 180 GW/cm², onto a 1-mm thick LGS crystal. The crystal was anti-reflection coated on the front surface for the NIR. A half-wave plate before the focusing lens was used to rotate the polarization of the NIR beam such that the beam

on the LGS was distributed evenly between the ordinary and extraordinary axis, for achieving type I phase matching.
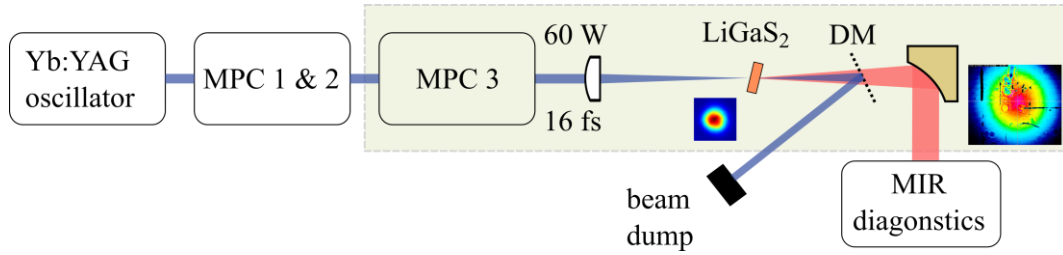
Figure 3.24 | Sketch of the setup used to generate MIR using IPDFG[*]. The shaded region indicates vacuum environment. The beam profile for the NIR focus at the crystal and collimated MIR beam after the parabolic mirror are shown. DM, dichroic mirror.
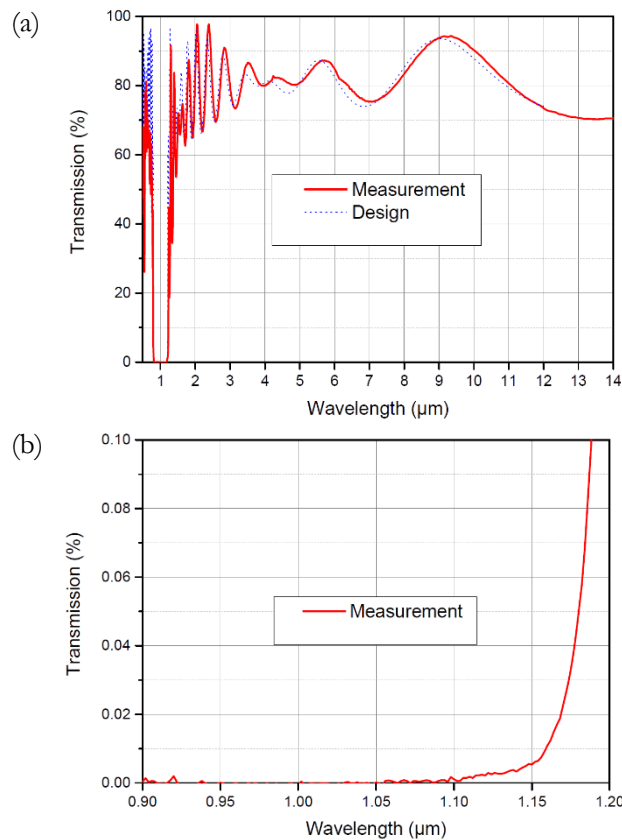
Figure 3.25 | Design and FTIR measurements of the NIR/MIR dichroic filter. The NIR beam is reflected while MIR beam is transmitted through the filter. a) Measured transmission for the full spectral range, b) magnified view of transmission for the NIR region. (Courtesy: *Florian Habel*).

---

[*] A detailed sketch of the setup is presented in Section 5.1

The NIR and MIR beams were separated after the crystal with a custom-designed dichroic filter on a 1 mm thick zinc selenide (ZnSe) substrate. The transmission performance of this filter (S161108) is shown in Figure 3.25. The NIR beam was reflected back from the front surface with total reflection > 99 %, and the MIR beam was transmitted with average transmission > 80 %. The MIR beam was collimated with an off-axis gold parabolic mirror. The collimated MIR beam was guided outside of the vacuum chamber for further diagnostics.

Fluctuations in the laser front end translate directly into the MIR power. For an input power of 100W from the oscillator, the residual power at the oscillator, power in the red wing of the NIR spectrum, and the power of the generated MIR were measured simultaneously. Figure 3.26 shows that the noise in the oscillator power directly translates into the MIR intensity noise (similar measurement to already shown in Figure 3.8). This reveals the need for intensity noise suppression, represented in Section 3.1.3, for sensitive measurements.
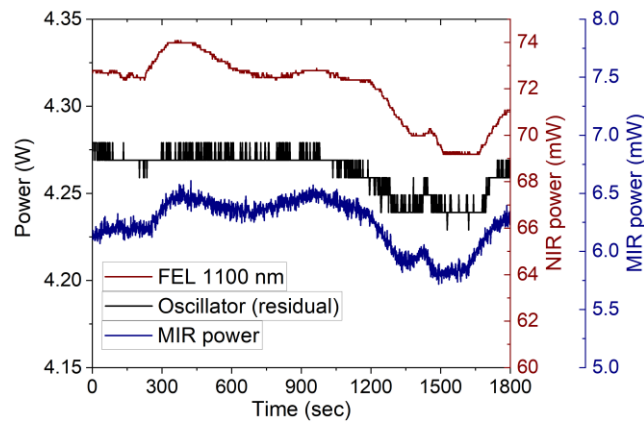
Figure 3.26 | Correlation in power fluctuations. Measured for the residual power at the oscillator (black curve), spectral wing of NIR (red curve) and generated MIR (purple curve). The power of the oscillator was measured with a water cooled thermal power meter, the broadened NIR and MIR power were measured with air cooled power meters.

Broadband NIR pulses allow for a wide phase-matching bandwidth to be exploited in the type I configuration of the biaxial LGS crystal. In addition to the phase-matching angle of the crystal, the dispersion of the NIR beam and the polarization of the NIR were also utilized for the MIR spectrum shown in Figure 3.27. The MIR spectrum was measured with an FTIR spectrometer (Lasnix L-FTS). The MIR has a beam path of less than 500 cm in air. The dispersion of the NIR beam was tuned by adding an additional bounce on the set of dispersive mirrors and then by adding bulk fused silica in the beam path. The polarization of the NIR was manipulated with a combination of a QWP and a HWP. In Figure 3.27, for all configurations except 5, the measured MIR power was around 80 mW. The blue tuned spectra (curve 5) has a factor of four less power. The NIR beam had an additional bounce on the set of dispersive mirrors, and bulk fused silica was added in combination of crystal

phase matching angle tuning for the generation of the spectra shown in curve 2, 3, and 5 in Figure 3.27. The spectra in curves 1 and 4 were generated with the optimization of the crystal phase-matching angle. The polarization of the input NIR beam was optimized for all configurations. All of the four broadband MIR spectra (curve 1-4) shown have bandwidths which are clearly broader than the MIR spectra generated in the OPA schemes described earlier.
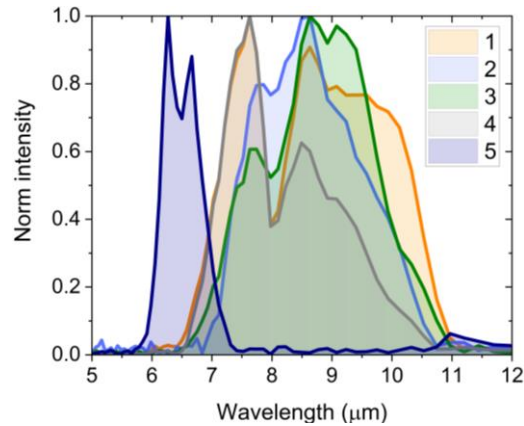
Figure 3.27 | Spectral tuning of the generated MIR spectrum in IPDFG, measured with FTIR. These measurements were done by changing the dispersion of the driving NIR beam as well as the phase matching of the LGS crystal. See text for description

3.3 Comparison of OPA with IPDFG

The OPA scheme offers a high conversion efficiency, enabling the generation of MIR pulses with higher pulse energies and peak power. As the pump and seed beam come from different pulses, with a typically narrowband pump it is only the seed beam that needs to be broadened. Moreover, the high pump intensities can be utilized without crystal damage. The control over the full pump and seed spectra give more flexibility for the required application. A large nonlinear crystal can be used for a typically narrowband pump. The IPDFG scheme driven by a single beam is insensitive to slight beam misalignments, ensures temporal and spatial overlap. The timing jitter of the pump and seed beam is eliminated, due to synchronization. IPDFG requires broadband driving pulses, so that the driving short pulses are prone to pulse stretching due to group velocity dispersion (GVD), causing a decrease in peak irradiance of the three-wave mixing process, resulting in a lower efficiency. In addition, the interaction length is limited due to temporal walk-off, so that thin nonlinear crystals are a preferred choice for IPDFG. This results in a trade-off between the bandwidth and conversion efficiency. In an OPA setup, on the other hand, the slight misalignment in the pump and seed beam could lead to lower efficiency as well cause angular dispersion of the idler beam. Any instability in the experimental setup would cause timing jitter and therefore cause CEP fluctuations in the idler.

Both schemes have their advantages and disadvantages, depending on the application of interest. Here, the MIR pulses were meant to be utilized in a field resolved measurement, where the issue of timing jitter is of central importance. To explore this, the MIR pulses generated in the broadband pump OPA setup were analysed by EOS detection (EOS detection is described in detail in chapter 4). The measured EOS field and spectra for ten measurements are shown in Figure 3.28. The inset shows the fluctuations at the centre of the EOS field. The RMS fluctuation of the zero-crossing is 1.73 fs, which is a factor of 12 higher than that for a similar IPDFG setup.
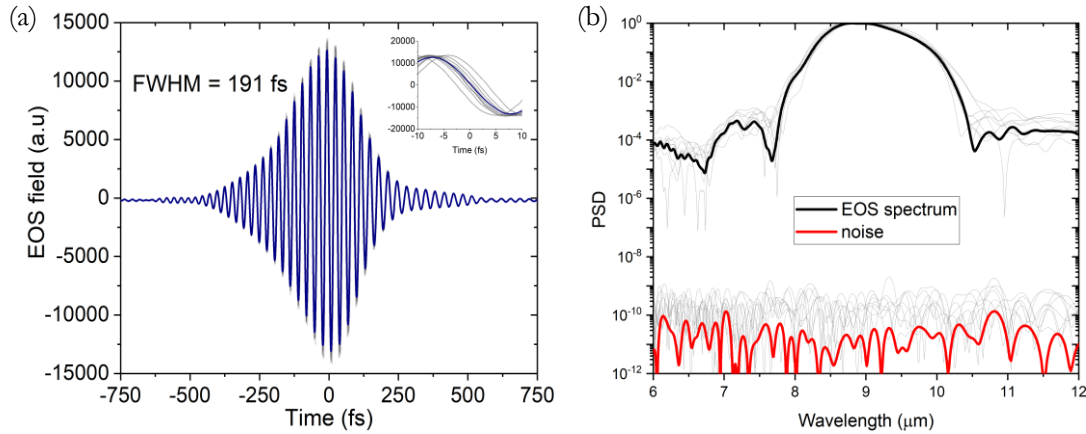
Figure 3.28 | EOS measurements of the MIR beam generated in broadband pump OPA.
a) EOS field for ten measurements, and b) corresponding power spectral density of MIR spectrum. The bold lines shows the averaged data. The noise floor was measured with MIR blocked to the EOS setup.

Since the driving pulse in IPDFG has a single-polarization, and the driving electric field is projected onto the slow and fast axes of the nonlinear crystal, only half of the photons contribute to the three-wave mixing process. This issue can be tackled with the help of custom-designed optics that rotate the polarization of only half of the spectral components of the beam, resulting in an increase in power by a factor of two for the generated MIR beam. Figure 3.29 shows the calculate data for the design for such a wave-plate for the IPDFG driving pulse presented in Section 0. The polarization of blue side of the NIR spectrum is not effected by the wave plate, while for red side of the spectrum (1150-1250 nm) it acts like a conventional achromatic half wave plate. Figure 3.29c shows the transmission through the wave plate when placed between parallel (0 degree) and crossed polarizer (90 degree). The magnified plots (dotted line) shows polarization loss is less than one percent in the centre of either wing of the spectrum.
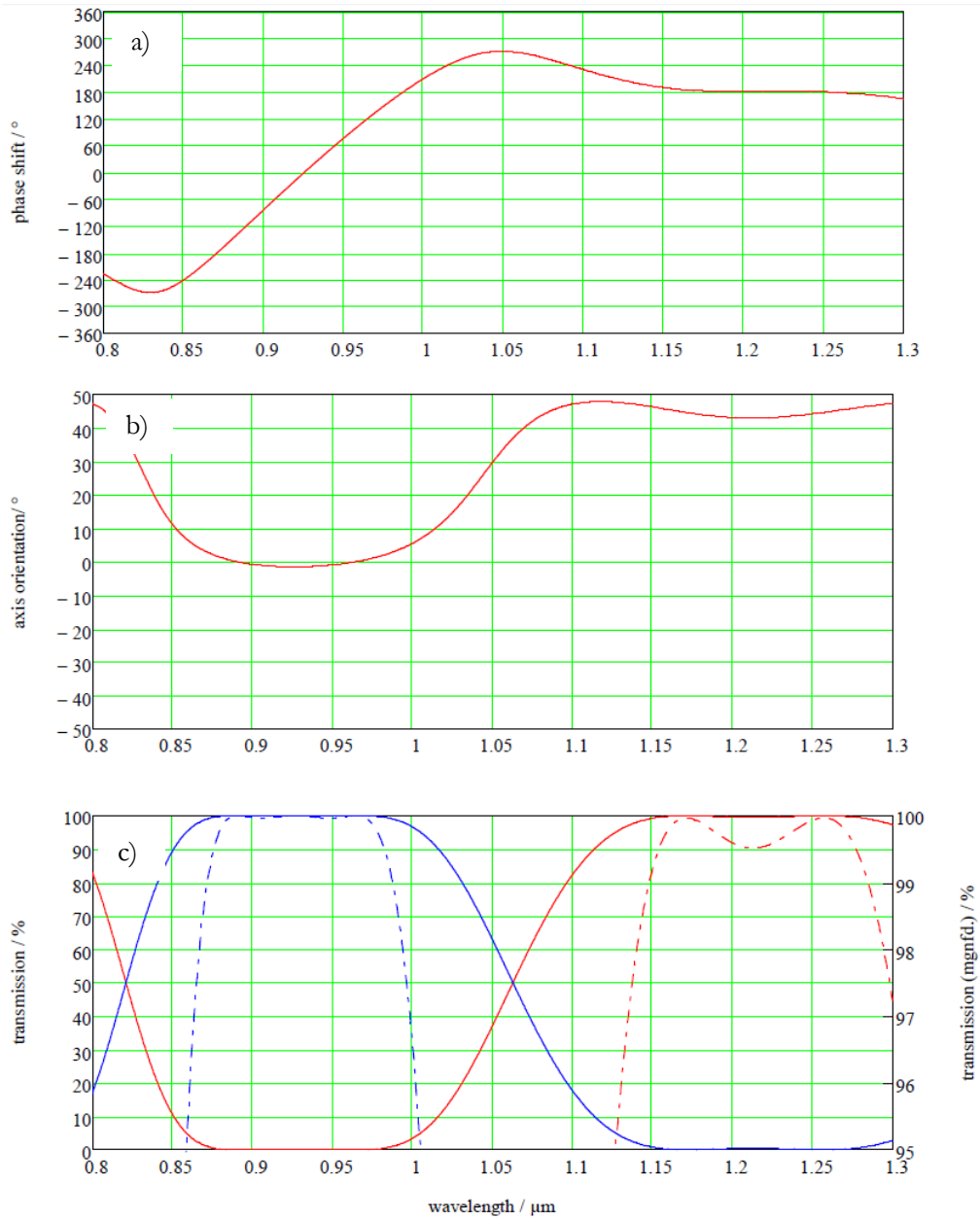
Figure 3.29 | Design of the custom wave-plate for partial polarization rotation. a) phase shift b) axis orientation c) transmission through a set of polarizers. (Courtesy : B.Halle Nachfl. GmbH)

Chapter 4

Electro-optic sampling

Electro-optic sampling (EOS) is a powerful scheme to obtain complete temporal information of the laser electric field, providing access to the amplitude of the pulses with a high temporal resolution and the phase with high accuracy. Since its first demonstration, a few decades ago, the scheme has seen several improvements, thanks to developments in laser sources and nonlinear crystals. While initial experiments were limited to the measurement of localized field[68], the technique has been extended to coherent detection of freely propagating THz radiation[69,70], and subsequently to the mid-infrared[71–74] and near-infrared regions[75].

In EOS, an external field (to be examined) interacts with a short probe pulse in an electro-optic crystal. The field information is obtained by detecting the delay-dependent polarization rotation of the probe pulse. The working principle of EOS is explained in Section 4.1, and the design characteristics are discussed in Section 4.2. The effect of various parameters associated with the process were studied with the help of numerical models and are presented in Section 4.3. Two experimental configurations were explored to study the broadband spectrum generated via IPDFG and detected with EOS, and are discussed in Sections 4.4 and 4.5. A more detailed description of the characterization of broadband MIR waveform stability with EOS is presented in Chapter 5.2.

4.1 Working concept

The working principle of EOS is the second-order nonlinear interaction between an external low-frequency field and a higher-frequency probing field in a nonlinear crystal. In the THz community, this is widely interpreted in terms of the Pockels effect. The linearly polarized probe pulse co-propagates with the external field inside the nonlinear crystal, preferably satisfying phase matching conditions. If the probe pulse duration is much shorter than a half-cycle of oscillation of the external field, the latter appears as a quasi-static field during the interaction in the crystal. The external field induces a change in birefringence of the EO crystal, i.e. different axes of the crystal exhibit different refractive indices for the polarized light. This induced birefringence causes a change in the polarization of the probe beam, causing the initially linearly polarized beam to become elliptically polarized. This change in polarization depends on the delay between external field and the probe beam, and also on the strength of the external field. The two orthogonal polarization components are separated in an ellipsometer and sent to a pair of balanced photodetectors, as sketched in Figure 4.1. Balanced detection suppresses the common laser noise and enhances the signal-

to-noise ratio of the measurement. The temporal waveform of the external field is measured by varying the relative time delay between the external field and the probe beam.
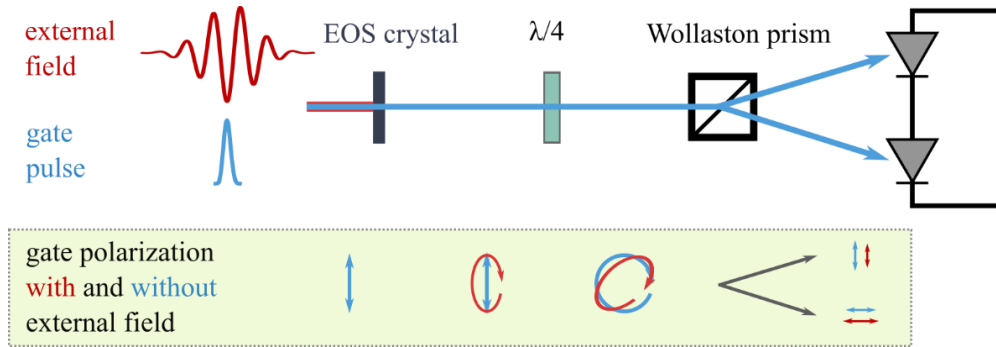
Figure 4.1 | Schematic diagram of EOS process as optical-field-induced polarization rotation.

The above description of EOS is valid when the frequency of the external field is much smaller than the bandwidth of the probe spectrum[76,77]. For a high frequency, broadband external field (referred to as MIR field in the following section), the detection process is better described in the frequency domain[78,79]. The interaction of the MIR field with the probe beam in the EO crystal causes the generation of phase-coherent sidebands through DFG and sum-frequency generation (SFG). Here, we describe only the SFG case, in accordance with the experimental conditions presented later in this chapter.

The incident MIR field and probe beam are linearly polarized, with the axes of polarization being perpendicular to each other. Their interaction for the given phase matching conditions results in an orthogonally polarized newly generated field, spectrally overlapping with the probe pulse. For the case of SFG signal, the newly generated spectrum overlaps with the probe spectrum on the high frequency side (short wavelengths) of the spectrum. The interference of the original probe photons with SFG photons results in the EOS signal.

The signal is detected in an ellipsometer consisting of a phase retarder (typically a quarter-wave plate) and a Wollaston prism. The EOS signal is measured using a pair of balanced photodetectors. The orientation of the phase retarder is chosen such that the balanced photodetector signal vanishes in the absence of MIR field. In principle, a single half-wave plate, or a single quarter-wave plate or a combination of both could be used, such that a better suppression of laser intensity noise at the output of the balanced photodetector in the absence of MIR field is achieved. This description of EOS process brings about some interesting implications on the detection process, such as enhancing the signal-to-ratio of the detection[79], and extension of the detection bandwidth[75].

4.2 Design considerations

In this section, various aspects related to the design of a state-of-the-art EOS setup are discussed, while a more rigorous simulation of the EOS process is presented in Section 4.3, followed by the experimental results in Sections 4.4 and 4.5.

- **Spectral Filtering**

Shot-noise-limited detection can, in principle, be achieved by the suppression of technical noise in balanced detection. The shot-noise limitation arises from the non-deterministic quantum distribution of the number of photons incident on each of the two detectors. The EOS signal scales linearly with the average power of the sampling pulse P_s, while shot noise scales with the square root of this power. Thus, the signal-to-noise ratio (SNR) for shot-noise-limited balancing scales with the square root of the sampling pulse power as:

$$SNR \sim \frac{P_s}{\sqrt{P_s}} = \sqrt{P_s} \tag{4.1}$$

An upper limit to this scaling is set by the available power of the sampling pulse or undesired nonlinear process in the EOS crystal, which could eventually lead to crystal damage.

EOS signal is generated by interference in the overlapping spectral region of the sampling pulse and the up-converted phase-coherent signal. This spectral overlap region depends on the central frequency of the MIR spectrum v_{MIR} and the bandwidth of the probe spectrum δ_s. If v_{MIR} is comparable to δ_s, the overlap occurs only on the outer wings of the sampling pulse spectrum. The spectral components beyond this region contribute to the shot noise, and not to the signal in the detection. A spectral filter can be inserted to the beam path that allows the photons in the overlap region to pass through it, while blocking the spectral regions not contributing to signal.

Assuming perfect phase matching for the SFG, bandwidth-limited pulse duration, and a frequency-independent susceptibility $\chi^{(2)}$, the spectral density of the electro-optic signal[79] for a given MIR frequency v_{MIR} is proportional to $vA(v)A(v - v_{MIR})$, where $A(v)$ denotes the sampling pulse spectrum, and $A(v - v_{MIR})$ denotes the SFG spectrum resulting from the given MIR frequency. Figure 4.2 shows a schematic description of the three spectra. Integration over frequency v yields the electro-optic response as a function of the MIR frequency v_{MIR}. For the spectrally filtered sampling pulse with a high-pass optical filter, cut-on frequency v_{HP} defines the lower boundary for integration. The spectral signal amplitude is given by the relation:

$$S(\nu_{MIR}) \propto A_{MIR}(\nu_{MIR}) \int_{\nu_{HP}}^{\infty} \nu A(\nu)A(\nu - \nu_{MIR})d\nu \tag{4.2}$$

The shot noise recorded with the spectral filter amounts to

$$\Delta_S \propto \sqrt{\int_{\nu_{HP}}^{\infty} \left((1-\eta)|A(\nu)|^2 + \eta|A(\nu - \nu_{MIR})|^2\right)d\nu} \tag{4.3}$$

Figure 4.2 compares the signal S and shot noise Δ_S as a function of filter cut-on frequency ν_{HP} for $\nu_{MIR} = 33$ THz, $\nu_s = 291$ THz, and assuming quantum efficiency $\eta = 0.0001$ (processing in close analogy to Ref. [79]). The electro-optic signal S has a fixed value for cut-on frequencies smaller than the central frequency of sampling pulse, and it starts to decrease through the overlap region between the sampling pulse spectrum and SFG spectrum. The noise, on the other hand, drops faster with increasing cut-on frequency. The SNR, defined by the ratio of the two, exhibits a maximum before it drops to zero. The peak at 317 THz defines the cut-on frequency of the high pass filter for maximum SNR, if no other noise sources are present.

- **Power scaling**

For a given time delay τ, the EOS signal emerging from the interference of the sampling pulse and the SFG pulse can be written as:

$$S(\tau) \propto E_s(t - \tau) \times E_{SFG}(t - \tau) \tag{4.4}$$

The SFG amplitude depends on the amplitude of the sampling pulse and the MIR pulse. So,

$$E_{SFG}(t - \tau) \propto E_s(t - \tau) \times E_{MIR}(t) \tag{4.5}$$

Thus,

$$S(\tau) \propto E_s{}^2(t - \tau) \times E_{MIR}(t) \tag{4.6}$$

This implies that the EOS signal is proportional to the intensity of the sampling field and the amplitude of the incident MIR field. The EOS signal scales accordingly, depending upon the available power in the sampling and MIR fields. A hard upper limit for increasing

the sampling field[*] is set by undesired nonlinear processes in the EOS crystal, eventually culminating in damage of the crystal.
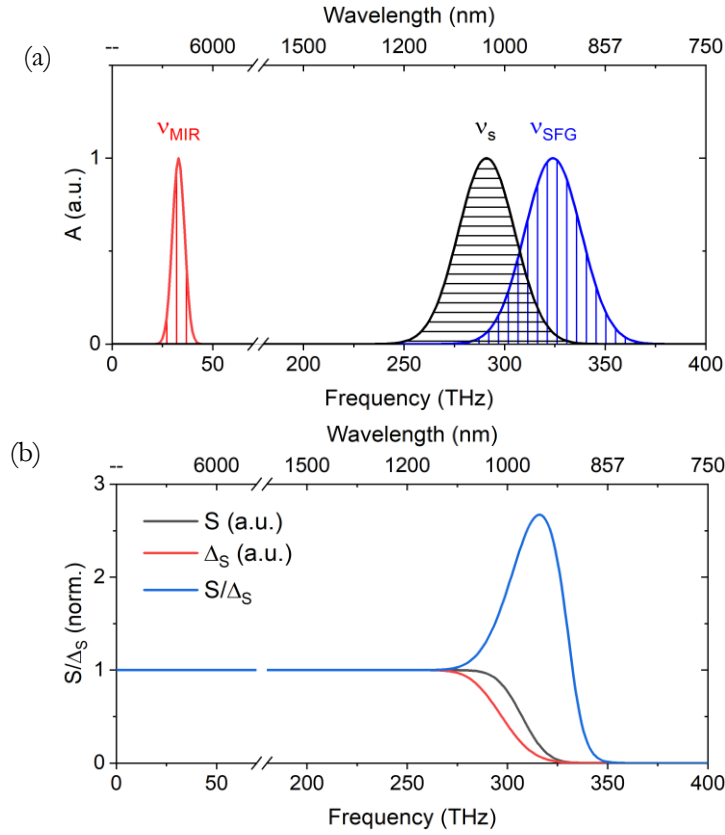
Figure 4.2 | Analytical EOS calculations. For the case when central frequency of the MIR is comparable to the spectral width of the sampling spectrum. a) Scheme of EOS according to sum-frequency generation description, b) Spectrally integrated signal S, and shot-noise level Δ_S as a function of cut-on frequency of the spectral filter. Light blue line: normalized ratio of S and Δ_S.

- **Focus size**

The geometric overlap between the sampling and MIR beams is crucial for efficient EOS signal generation[†]. The focus waist of the incident sampling and MIR beams should be chosen for an efficient generation of the SFG signal. The MIR frequency whose spot size spatially overlaps with the sampling beam will be detected with higher efficiency. The overlap integral for the concentric Gaussian beams[80] is

---

[*] The undesired nonlinear processes in the EOS crystal a result of high sampling power degrades the balancing in the detection process.
[†] The efficient heterodyne detection at the photodiode requires a constant modulation depth across the focus, so the mode size of the sampling and the SFG beams would be same. Too small waists size leads to short Rayleigh length and interaction length, thus lowering the conversion efficiency. Too larger waist size, on the other hand, also lowers the efficiency due to less peak intensity.

$$T_{overlap}(\nu) \sim \sqrt{\frac{\omega_s^2 \omega_{MIR}^2(\nu)}{\omega_s^2 + 2\omega_{MIR}^2(\nu)}} \tag{4.7}$$

where, ω_s and ω_{MIR} denote the beam waists of the sampling beam and the MIR beam respectively. Figure 4.3 shows this relationship for various beam waists.

- **Lock-in detection**

The output of the balanced detector is typically fed to a lock-in amplifier for the detection of the modulated signal. A mechanical chopper is used to modulate the MIR beam, typically at a frequency of a few kHz. For detection in high frequency range, various other methods, such as photoelastic modulator[81,82], acousto optic modulator[83,84] and other fast-scan methods[85] can be used. A lock-in detection based on the piezoelectric modulation at 104 kHz was realized, and is presented in Section 4.4.
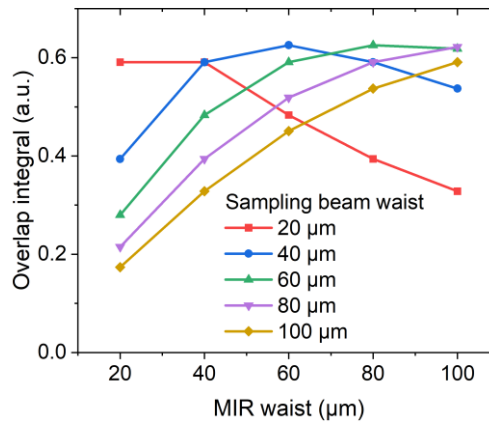
Figure 4.3 | Calculated overlap integral for different sampling beam and MIR waist.

- **Sampling pulse duration**

The frequency domain description of EOS, presented earlier in this chapter requires the sampling pulse duration to be shorter than a half-cycle of the MIR pulse. The EOS signal tends to become distorted (as it deviates substantially from the actual electric field) if this condition is not fulfilled. Also, the use of a spectral filter in the EOS detection[79] not only selects the photons that contribute to the EOS signal and suppresses the noise contribution, but also reshapes the response function of the EOS detection[75]. Thus, signal detection can be pushed towards higher frequencies for the given pulse duration of the sampling beam.

4.3 Simulations

Simulations of the EOS process were performed, based on a first-order propagation equation in the slowly-evolving wave approximation[75,86], expressed in the frequency domain as

$$\frac{\partial E_\omega(z)}{\partial z} = -ik_\omega E_\omega(z) - \frac{i\omega}{2n(\omega)\varepsilon_o c} P_\omega^{NL}(z) \qquad (4.8)$$

where E_ω is the complex amplitude of a spectral component of frequency ω, propagating in the z direction with wave-vector k_ω, $n(\omega)$ is the frequency dependent refractive index, and P_ω^{NL} is the nonlinear polarization of the EOS crystal. The simulations were performed in MATLAB, using modified Euler algorithm. The nonlinear polarization was calculated in the time domain, and transformed back to the frequency domain via Fourier transformation. The frequency dependent refractive index was calculated by using the Sellmeier equation for the EOS crystal.

Simulations were performed as a qualitative analysis of EOS detection for the MIR source from the fiber-based setup, presented in Section 0. Transform-limited Gaussian spectra (analogous to the experimental conditions) for NIR and MIR were employed as the input to the simulations, to calculate the SFG signal for 1D propagation in gallium selenide (GaSe) for type-II phase matching. The EOS signal was simulated for various values corresponding to the crystal thickness, sampling pulse duration, and spectral filtering.
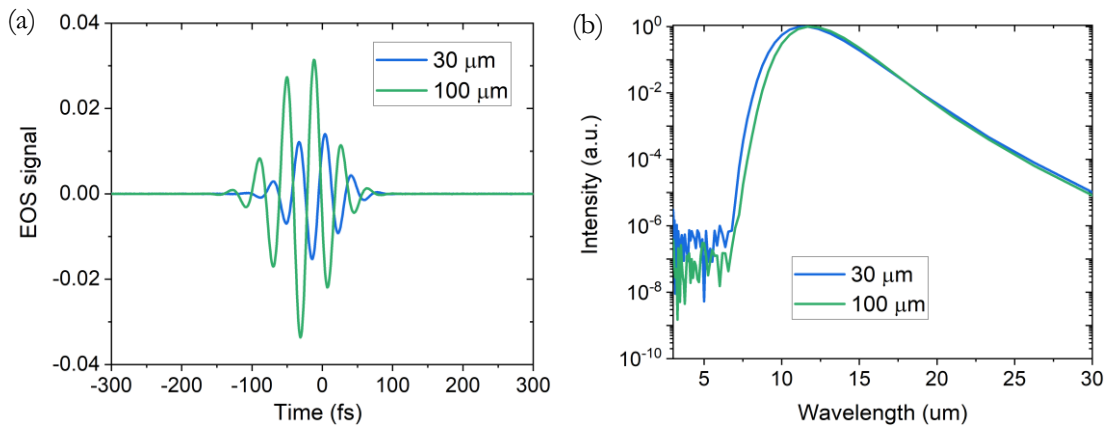
Figure 4.4 | EOS simulations for different crystal thickness. a) EOS signal and b) EOS spectrum.

Figure 4.4 shows the EOS signal for a crystal thickness of 30 μm and 100 μm. Thin crystals support relatively broader detection bandwidth especially on the blue side of the spectrum. An increase in crystal thickness leads to the increase of the SFG signal due to a

longer interaction length between the sampling and MIR beams. The EOS signal is almost a factor of 2.5 higher for the 100-µm crystal.
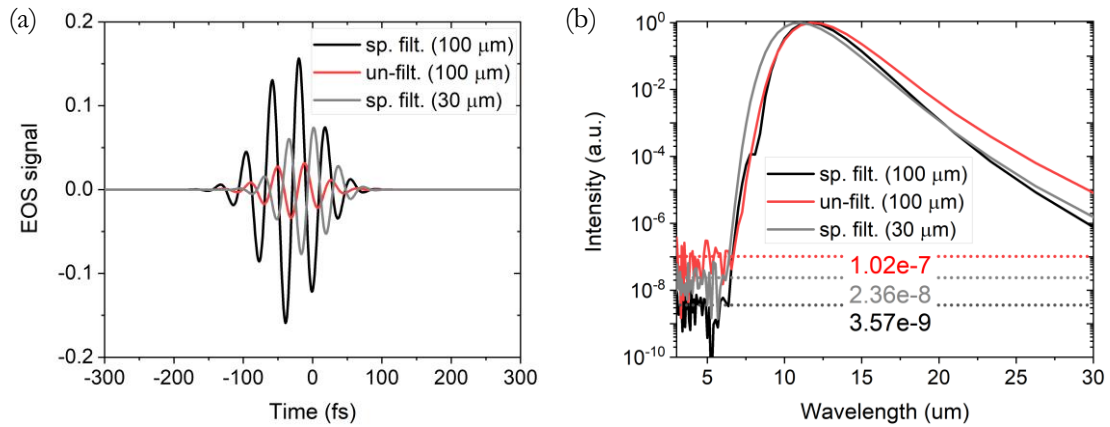
Figure 4.5 | EOS simulations for unfiltered and filtered case. a) EOS signal and b) EOS spectrum for a 100-µm thick GaSe crystal. The results for 30-µm GaSe thick crystal are also shown for comparison. The dotted lines show the respective noise floor, calculated as a mean value in the wavelength range from 3 to 5.5 µm.

Figure 4.5 shows the effect of spectral filter on the simulated EOS signal. A short pass spectral filter with cut-off wavelength of 950-nm (Thorlabs, FES0950) was used to filter the sampling pulse spectrum before detection. For a crystal thickness of 100-µm, the filtered signal is almost a factor of 5 higher than the un-filtered case. The spectrum for the filtered case is reduced on the longer wavelength side, but slightly enhanced on the short wavelength side. For comparison, the filtered case for 30-µm thick EOS crystal is also shown. The EOS signal is a factor of 2.3 higher than the unfiltered signal, and it supports more blue components in detection. The noise floor (dashed line in Figure 4.5 b) is calculated as a mean value for the wavelength range from 3 to 5.5 µm for the spectrum shown. This implies that the intensity dynamic range is higher by a factor of 28 for the filtered case.

The simulations were performed for different spectral filters to identify the optimum spectral filter, considering the options available from different industrial suppliers. We considered three different short pass filters with cut-off wavelengths of 912 nm (Semrock, FF01-950/SP-25), 930 nm (Asahi-spectra, XIS0930), and 950 nm (Thorlabs, FES0950). The EOS simulation results and the transmission curves for these filters are shown in Figure 4.6. These results indicate an increase in the dynamic range as well as the enhanced detection of the shorter MIR wavelengths with strong spectral filtering. Further, in order to study the effect of the duration of the sampling pulse, the EOS signal was simulated for 20-fs and 12-fs sampling pulses in a 30-µm thick EOS crystal, while keeping the peak intensity constant for both cases. Using a spectral filter with a cut-off wavelength of 950-nm, sampling with 12-fs pulses results in a slightly higher dynamic range compared to using 20-fs pulses, as shown in Figure 4.7. For the un-filtered case, the EOS signal for 12-fs gating pulses is only marginally better than for 20-fs pulses, implying that the increase in dynamic range is mainly

due to spectral filtering for the earlier. The spectrum for unfiltered EOS is similar in both the cases. Besides the EOS signal strength, a shorter sampling pulse also helps reduce noise on the balanced detector in a shot-noise limited detection setup[87].
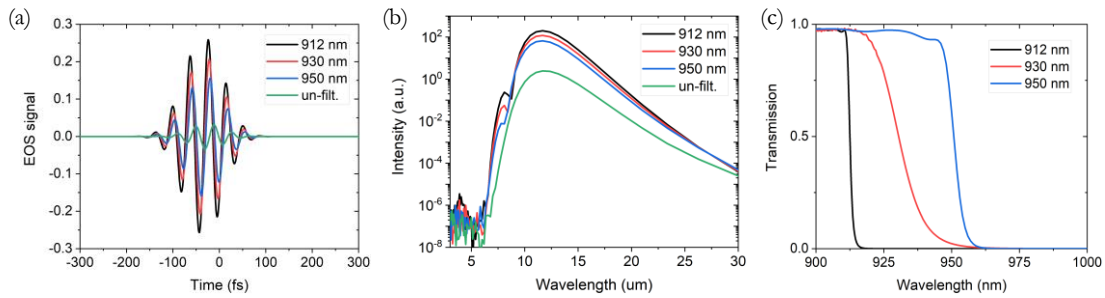
Figure 4.6 | EOS simulations for different spectral filter. a) EOS signal, b) EOS spectrum, and c) transmission curve of the spectral filters. The data for the spectral filter 912 nm, 930 nm, and 950 nm is taken from Ref.[88], Ref. [89], and Ref. [90] respectively.
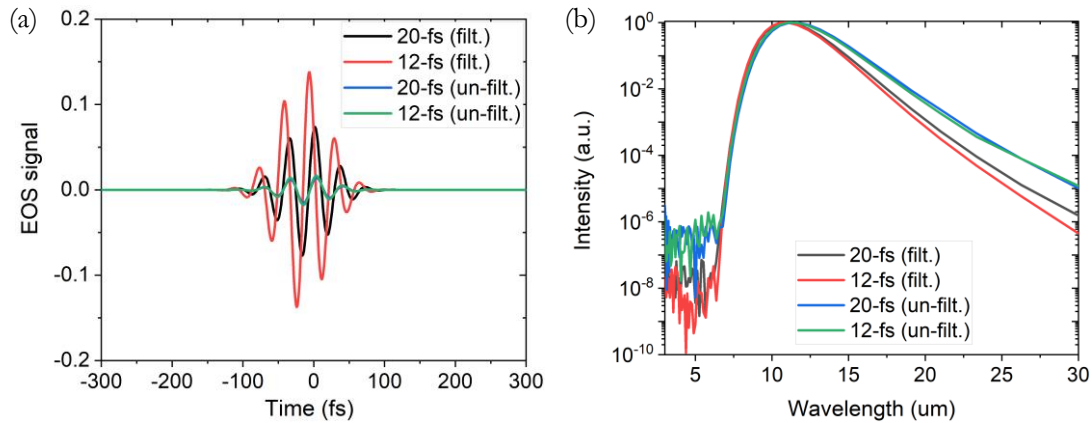
Figure 4.7 | EOS simulations for different sampling pulse durations. a) EOS signal, and b) EOS spectrum for different sampling pulse durations with and without spectral filtering in a 30-μm thick GaSe crystal.

The simulations presented in this section give a good qualitative estimate for various parameters in the EOS process for enhancing the detection efficiency[*]. These insights play an important role in improving the EOS detection, as presented in the next section. Also, these simulations show an overestimate of the long wavelength spectrum. This would have to be taken into consideration for quantitative analysis.

---

[*] A careful simulation study would be needed while designing EOS setup with a short sampling pulse (~15-fs or less) and a thicker EOS crystal. Since dispersion will play a critical role in determining the EOS signal strength and detection bandwidth.

4.4 Infrasampler 1.1

The field-resolved detection in the setup based on fiber compression (Section 3.1.2) is referred to as Infrasampler 1.1 (IS 1.1). The schematic diagram of the setup is shown in Figure 4.8.
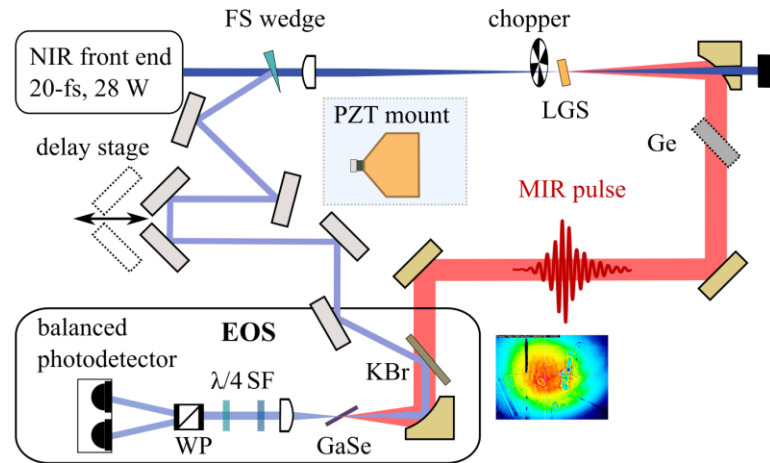
Figure 4.8 | Schematic setup of the Infrasampler 1.1. A beam profile of MIR beam before EOS is shown. The dotted box in the middle shows a sketch of the PZT mount assembly, small silver mirror and a piezo actuator are glued on a big copper block of cylindrical-cone shape.

A fraction of the beam after the NIR compressor, separated by means of an uncoated fused-silica wedge, serves as a sampling beam in the EOS detection. The NIR beam is focused onto an LGS crystal for MIR generation. A mechanical chopper at 4.2 kHz is used in front of the LGS crystal for lock-in detection. This frequency was chosen to avoid any access mechanical vibration noise of the chopper wheel. The generated MIR beam propagates collinearly with driving NIR beam transmitted through LGS crystal. A perforated parabolic mirror was used, such that the NIR beam passes through the hole of the mirror to the beam dump, and the collimated MIR beam is reflected. Any remaining NIR beam was filtered by a germanium (Ge) window after the collimation parabola. A potassium bromide (KBr) window was used as a beam combiner. The sampling NIR beam and MIR beam propagate collinearly and were focused to a 100-µm thick GaSe crystal for EOS detection. A short-pass spectral filter with a cut-off wavelength of 950 nm was used before the quarter-wave plate and the Wollaston prism. The experimentally measured EOS amplitude and spectrum with and without spectral filter are shown in Figure 4.9. For the unfiltered case, a neutral density filter was used such that the NIR power incident on the photodiode is similar to that of the filtered case. As predicted in the simulations, the filtered measurements show enhanced short-wavelength components in the MIR spectrum and a higher dynamic range. On the long-wavelength side, a CO_2 absorption dip around 15 µm is clearly visible in both cases. On the short-wavelength side, the filtered spectrum shows many ripples due to water vapor absorption between 6 µm and 7 µm.
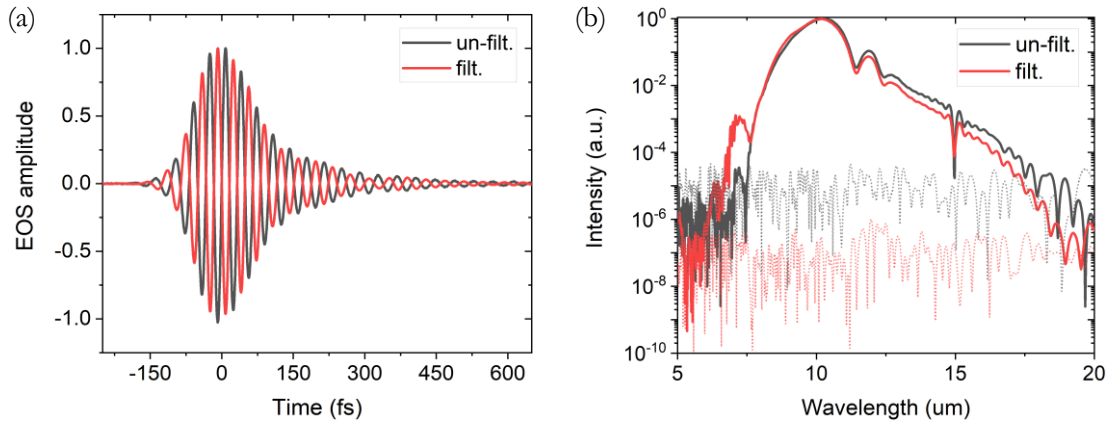
Figure 4.9 | EOS measurement with and without spectral filtering. a) EOS amplitude (normalized), and b) EOS spectrum. The dotted lines represent the noise floor as an average of five measurements with the MIR beam blocked to the EOS setup.

Typically, the MIR spectrum is tuned by choosing a different phase-matching angle at the MIR generation crystal. In principle, such spectral tuning can also be achieved in the detection crystal. The interaction geometry of the NIR and MIR beams, and the orientation of the EOS crystal affect the polarization state of the sampling beam. This leads to a change in balancing at the photo-diode, and thus, a relatively higher noise in certain cases. EOS measurements were performed for three different phase-matching angles The orientation of $20°$ resulted in the highest dynamic range with broadband detection, as shown in Figure 4.10. The noise floor is calculated by taking the average of spectra in the range from 3 to 4 μm of the respective measurements.
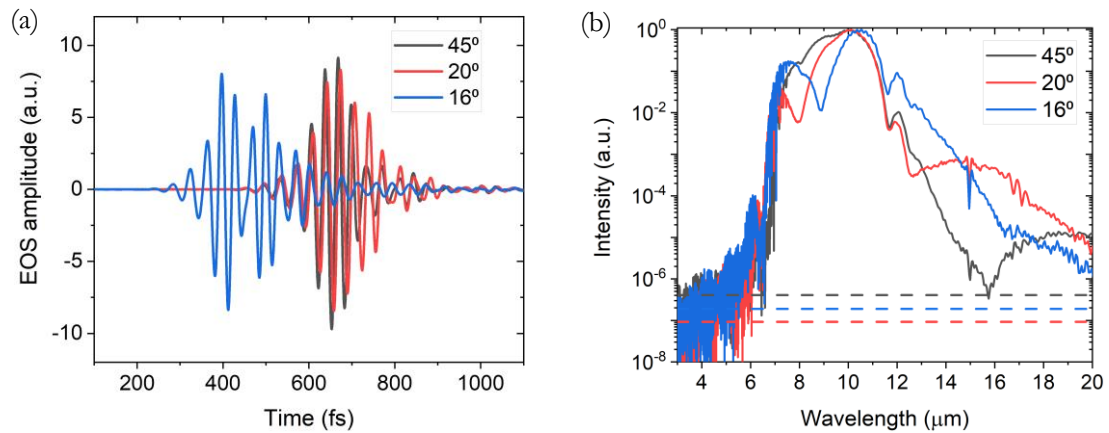
Figure 4.10 | EOS measurement for different phase-matching angles of EOS crystal. a) EOS amplitude and b) EOS spectrum. The dashed lines indicate the respective noise floor levels calculated from the spectra in the range from 3 to 4 μm.

The EOS measurements reported above were performed with lock-in detection using a mechanical chopper, which is typically limited to the range of few kHz. A proof-of-concept experiment was performed for detection at higher frequencies, by modulating the length of the sampling beam path by means by a piezo actuator at its resonance frequency.
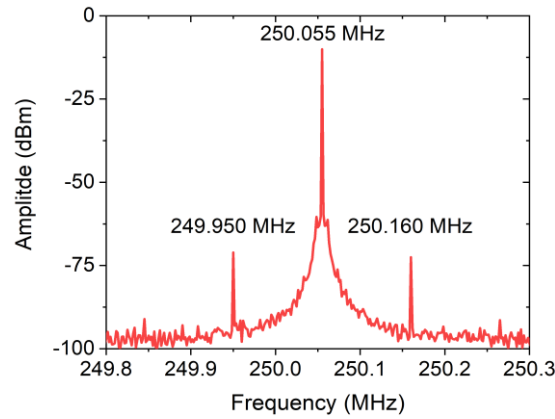
Figure 4.11 | Characterization of the PZT assembly. The side-bands shows resonance frequency of the PZT assembly.

The piezo actuator (PI, PL033.3x) was attached to a big cylindrical cone shaped copper block[*], and a small silver mirror (thickness = 1 mm, diameter = 3mm) was attached on the other side with Torseal. The sketch of the assembly is shown Figure 4.8. A sinusoidal signal of 10 V_{pp} from a signal generator was applied to the actuator. This assembly gives a resonance frequency of 105 kHz, characterized with a spectrum analyzer, as shown in Figure 4.11. The central peak shows the repetition rate of the laser used for the characterization, while the side-bands across the central peak show the resonance frequency of the PZT assembly.

The EOS measurement with a mechanical chopper at 4.2 kHz were compared with the PZT-based modulation at 105-kHz, and the results are shown in Figure 4.12. The time-axis of the chopper-based amplitude is shifted such that central part of the EOS amplitude overlaps for the two cases. The EOS amplitudes and the corresponding spectra for both cases are quite similar. For fifty consecutive EOS scans, the PZT-based measurement shows an increase by a factor of 3 in SNR compared to that with the chopper. This increase is possibly due to the fact that the typical noise sources lies in the range of few kHz, and the effect is largely reduced at higher frequencies.

The PZT-based setup faced two problems, but further characterization was not performed due to the course of the planned experiments on the setup. The first issue was that the NIR beam profile at EOS balanced photo-diode get distorted. This could be due to the beam movement in the large angle of incidence geometry of the PZT mount. Possibly, a decreased angle of incidence and a careful alignment would help to overcome this problem. Secondly, the PZT amplitude showed a phase slightly different from the chopper phase, so a careful analysis of the effect of PZT phase modulation in an EOS measurement would be

---

[*] The weight and size of the mirror are crucial to get a uniform modulation for a given piezo actuator. Moreover, the shape and material of the holding adapter also plays an important role regarding noise attributes.

need to use this scheme in a field-resolved measurement. In principle, such a modulation scheme offers an attractive route to fast-scan applications, and high SNR measurements by avoiding noise/drifts on slow time scales.
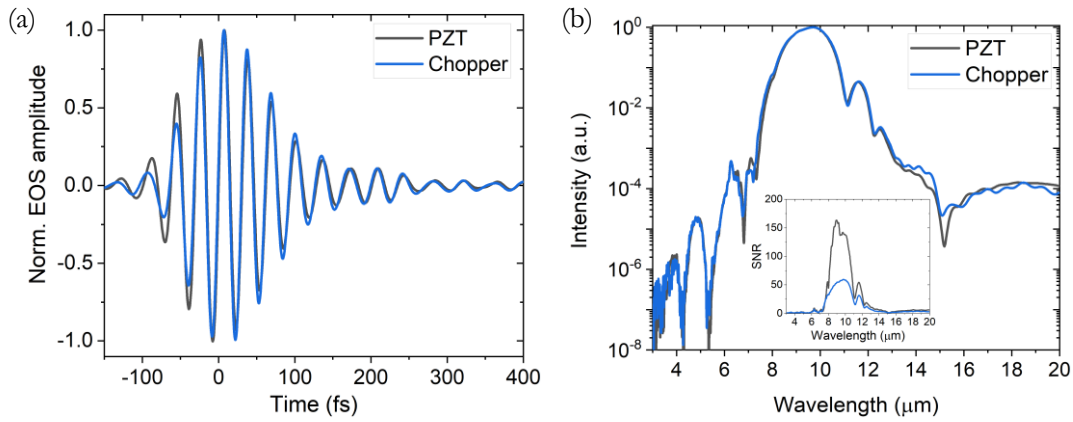
Figure 4.12 | EOS measurement for different chopping techniques. a) EOS amplitude (normalized), and b) EOS spectrum measured by using mechanical chopper and PZT-based modulation.

Another proof-of-principle experiment was performed to test if a short pulse duration could improve the EOS detection. A scheme based on cross-polarized wave generation[91,92] (XPW) was implemented, as it can lead to compression by a factor of $\sqrt{3}$. For an efficient conversion considering negligible dispersion and nicely compressed input pulses, this would lead to ~12-fs sampling pulse instead of the 20-fs pulse.
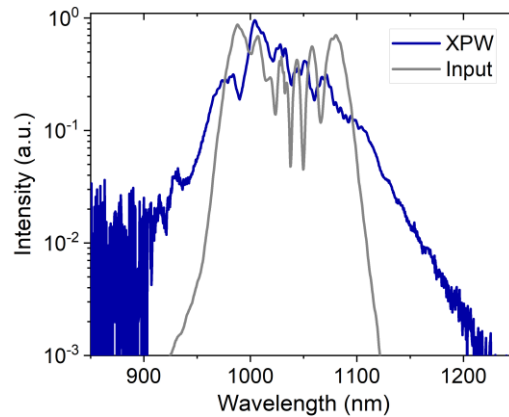
Figure 4.13 | OSA measurement of the XPW output. The input spectrum is shown for reference.

A sapphire wedge was used instead of the fused-silica wedge that reflects ~ 7% of the incident power, after the fiber compressor. An additional set of chirped mirrors with a wedge-pair was used to optimize the pulse compression. An off-axis parabolic mirror was used to focus the NIR beam to a 1-mm thick BaF2 crystal (z-cut) for XPW broadening, and a second parabolic mirror was used to collimate the beam. As an XPW generated beam is

orthogonal to the original linear polarization, a Glan-Taylor polarizer was used to separate the input and XPW beams. Figure 4.13 shows the spectra of the input and XPW output, measured with OSA. The XPW process acts as a spatial and temporal filter to the input beam, so the XPW spectrum shows relatively less modulations as compared to the input spectrum. The output power of the XPW beam was limited to a few hundred micro-watt only. This scheme was not used in the EOS experiments as there was not sufficient power available to drive the third-order XPW process, and to use its output as a sampling beam in the EOS setup.

4.5 Infrasampler 1.2

The setup referred to as Infrasampler 1.2, utilizes the MIR beam generated by IPDFG based on bulk-compression presented in Section 0. A schematic diagram of the setup is shown in Figure 4.14. The NIR pulses were recycled and used to sample the MIR waveforms. The polarization of the NIR beam after the dichroic mirror was cleaned by reflecting it off a fused-silica wedge at Brewster's angle. The pulses were recompressed with chirped mirrors and a custom designed beam splitter was used to further attenuate the power for optimum gating conditions in the EOS detection. The sampling pulse power was adjusted just below the damage threshold of GaSe. This corresponds to an average power of 420 mW at the crystal.

The delay between the NIR beam and MIR waveform was achieved with a mechanical stage (PI-Micos, L-511). The NIR beam size was adjusted with a two-lens telescope before the beam combiner. A germanium window was used as a beam combiner, to spatially recombine the NIR and MIR beams. The MIR beam was chopped before the beam combiner, at a frequency of 7.5 kHz. The NIR sampling beam was reflected off the Ge plate and the MIR beam was transmitted at Brewster's angle. Both beams were focused to the EOS crystal using a 50-mm focal-length off-axis parabolic mirror. MIR beam profile along the beam path is also shown in Figure 4.14.

- **Delay Tracking:**

To reduce phase artefacts due to the variations in the mutual delay between MIR field and the NIR sampling pulse, we track this delay interferometrically, by using an auxiliary continuous-wave laser. A beam from a frequency-controlled distributed-feedback laser diode at 1550 nm was co-propagated along the MIR and NIR paths, after being split at the dichroic mirror (green line in Figure 4.14). Interferometric delay tracking[93] was achieved by modulating the frequency of the laser and by demodulating the resulting interference signal at two different frequencies that can be phase shifted with respect to each other to construct a quadrature signal. In contrast to a simple interference signal, this allows for a constant position sensitivity and for a directionality of the measurement. The implemented system

was based on a commercial interferometer (Smaract PICOSCALE). All data was taken with a common clock. Synchronization of the EOS and delay information was realized by recording forward and backward scans, and then shifting the entire data sets by a constant time value such that the forward and backward traces become congruent.
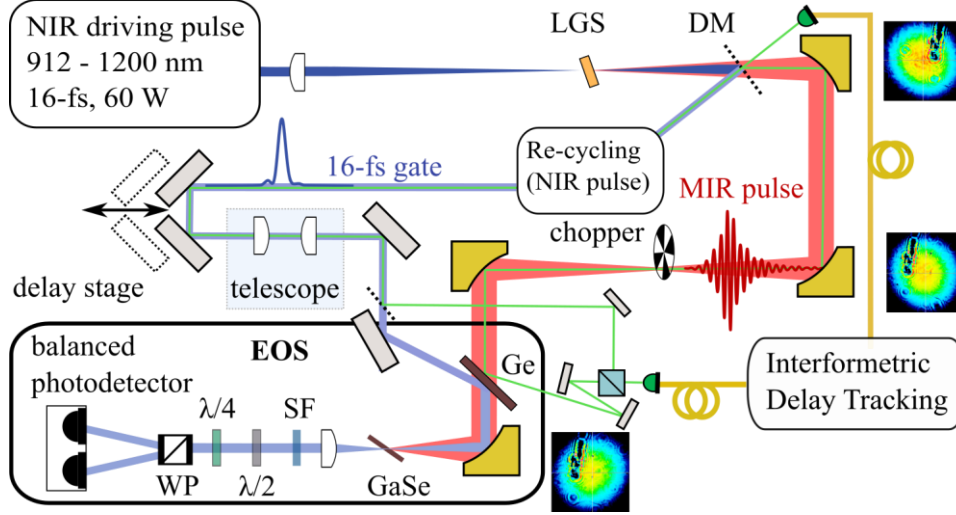
Figure 4.14 | Schematic setup of Infrasampler 1.2. NIR pulse drive IPDFG in LGS, and a dichroic mirror (DM) separates the two beams. NIR beam (blue) was recompressed with chirped mirror, and its power and size was optimized for EOS. MIR beam (red) was chopped recombined with germanium (Ge) window for EOS detection. An auxiliary continuous-wave laser beam (green) co-propagates to track the beam path. MIR beam profile at various positions is also shown. SF, spectral filter; $\lambda/2$, half-wave plate; $\lambda/4$, quarter-wave plate.

- **Spectral Filter and balanced detection:**

The combination of a spectral filter, a half-wave plate and a quarter-wave plate was used to balance the photodiodes after the Wollaston prism. A short-pass filter at 912 nm was used for enhancing the SNR[79] of the EOS. The signal was detected with a self-built balanced detector, consisting of two photodiodes (first sensor, series 7, chip PC10-7), followed by a low-noise current amplifier (femto DLPCA-200). The diodes were reverse-biased with 15 V and the amplification was set as high as possible without saturating the lock-in amplifier (integration time 186 μs with 6th-order filtering at a chopping frequency of 7.5 kHz). The resulting noise floor was a factor of 1.6 above the shot noise level of the NIR beam, as shown in Figure 4.15. Assuming a DC signal due to averaging over several pulses, the theoretical value for the single-sided linear spectral density s_q of the relative quantum power noise was calculated as

$$s_q = 1.9 \times 10^{-8} \mathrm{Hz}^{-\frac{1}{2}} \times \sqrt{\frac{1\mathrm{mW}}{P}} \times \sqrt{\frac{1064\mathrm{nm}}{\lambda}} \tag{4.9}$$

where P is the optical power incident on the detector, λ is the wavelength of the radiation (the detector quantum efficiency was assumed to be 1).
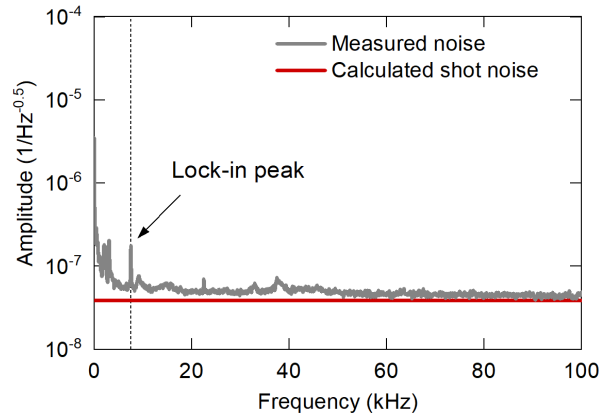
Figure 4.15 | Frequency-resolved measurement of the noise in EOS setup. Noise at balance detector (black), and calculated shot noise (red). The lock-in frequency is indicated by dotted line. Figure is taken from Ref. [37].

- **Conversion efficiency optimization:**

The parameters of the NIR beam were optimized for efficient sum-frequency generation (SFG) and EOS detection. The telescope in the NIR beam path was adjusted to achieve a similar focal spot size as that of MIR beam (~80-µm) at the EOS crystal. The upconvesion can be optimized by monitoring either the SFG signal or the dip in the MIR power after the EOS crystal[94]. The measured NIR spectra after the EOS crystal is shown in Figure 4.16. The spectrum of the NIR beam (gray) that drives the MIR generation is shown for reference. The sampling beam spectrum (red) shows a stronger modulation on red side of the spectrum in comparison to the driving spectrum. The sampling and SFG spectra were measured by placing a polarizer in the beam path with orthogonal orientations. The SFG spectrum was measured with (light blue) and without (violet) a spectral filter (912 nm) after the 500-µm thick GaSe crystal used for EOS. The position of the delay stage and phase matching were adjusted to obtain maximum power in the sum-frequency spectrum. A background measurement, performed by moving the GaSe crystal out of focus, shows that the central components of sampling beam are still present in the orthogonal polarization state. This could either be due to the limited extinction ratio of the polarizer or due to the birefringence in the GaSe crystal. A dip measurement of MIR depletion shows a frequency up-conversion efficiency of 2.2% for a 500 µm thick crystal, and 0.3% for an 85 µm thick crystal[37,94]. The dip measurement was performed by measuring the delay dependent MIR power after the EOS crystal.
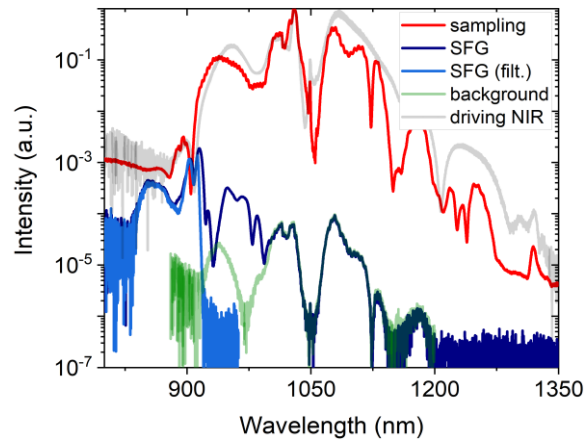
Figure 4.16 | OSA measurement of NIR spectra after the EOS crystal. A typical spectrum of driving NIR beam (grey curve) is shown for reference.

- **Dynamic range and spectral tuning:**

The higher conversion efficiency for the thicker crystal translates into a higher dynamic range, and the relatively lower efficiency for thin crystal translates into broad detection bandwidth at the cost of a lower dynamic range. A comparison of three different configurations is shown in Figure 4.17.
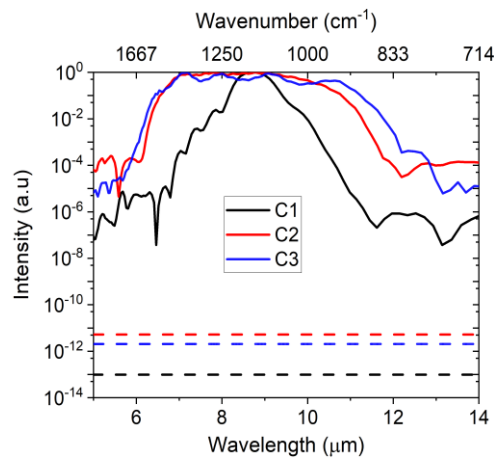
Figure 4.17 | Dynamic range for different crystal configurations. C1: using 1mm thick LGS crystal for DFG and 500-μm thick GaSe as EOS crystal, C2: using 0.7-mm thick LGS crystal for DFG and 30-μm thick GaSe as EOS crystal, C3: same as C2 but without liquid cuvette.

EOS detection was optimized with a liquid cuvette in the MIR beam path, and it consists of two parallel 2-mm ZnSe windows, enclosing a 34-μm-long propagation path through the liquid sample. This cuvette was used for field-resolved measurements of the liquid samples. For the black curve, MIR was generated in a 1-mm thick LGS crystal and a 500-μm thick GaSe was used for EOS. For the red curve, MIR was generated in a 0.7-mm thick LGS crystal and EOS detection was done using a 30-μm thick GaSe crystal. The blue

curve is the same as the red curve, except that the liquid cuvette was removed from the MIR beam path. The dashed lines show the corresponding noise floor levels. The broadband configuration represents almost an octave-spanning spectrum having a dynamic range of 12 orders of magnitude, making the system a one-of-a-kind instrument for spectroscopic applications.
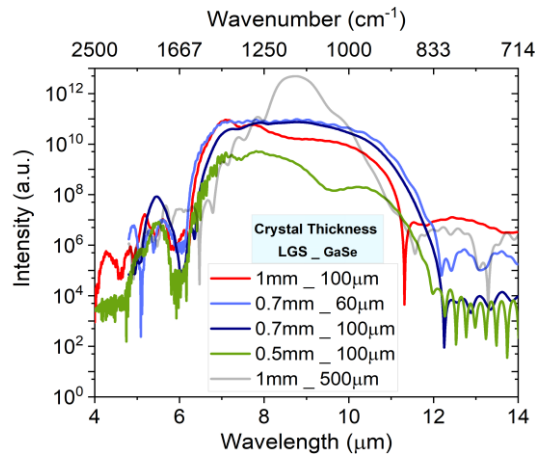
Figure 4.18 | Spectral tuning for different crystal configurations. The thickness of the MIR generation crystal (LGS) defines the generated MIR power and bandwidth. And, thickness of the EOS crystal (GaSe) defines the detection bandwidth and EOS signal strength.

The spectral tuning was further explored by using different combinations of the generation and detection crystals. A few different combinations are shown in Figure 4.18. Each of the spectra is normalized to its corresponding noise floor, such that curve shows its dynamic range. The thickness of each of the two (generation and detection) crystals exhibits a trade-off between the achievable spectral bandwidth and spectral power. All measurements were taken at a vacuum level of a few milli-bar, except the green curve which has almost one meter of its beam path in air and shows ripples in the spectrum due to absorption in water vapor around 6.5 µm. The green curve (0.5-mm thick LGS and 100-µm thick GaSe) is broader than the others, but with a lower dynamic range. The dynamic range and spectral bandwidth for the red (1-mm thick LGS and 100-µm thick GaSe), violet (0.7-mm thick LGS and 100-µm thick GaSe), and light blue (0.7-mm thick LGS and 60-µm thick GaSe) curves are similar. The latter (light blue curve) gives a good compromise between detection efficiency and bandwidth.

- **Source brilliance:**

Figure 4.19 shows the brilliance of the broadband configuration of IS 1.2 in comparison to conventional sources of radiation in the mid-IR. The table-top source presented here, across the available bandwidth, provides more than five orders of magnitude higher spectral brilliance compared to the conventional thermal sources (Globar), and more than two orders of magnitude higher spectral brilliance in comparison with 3rd-generation

synchrotron beamlines[95]. In this measurement configuration, the spectrum below 6-μm and above 12-μm are the artifacts more likely. Additionally, this MIR source maintains a high degree of spatial and temporal coherence and delivers pulses close to their temporal bandwidth limit.
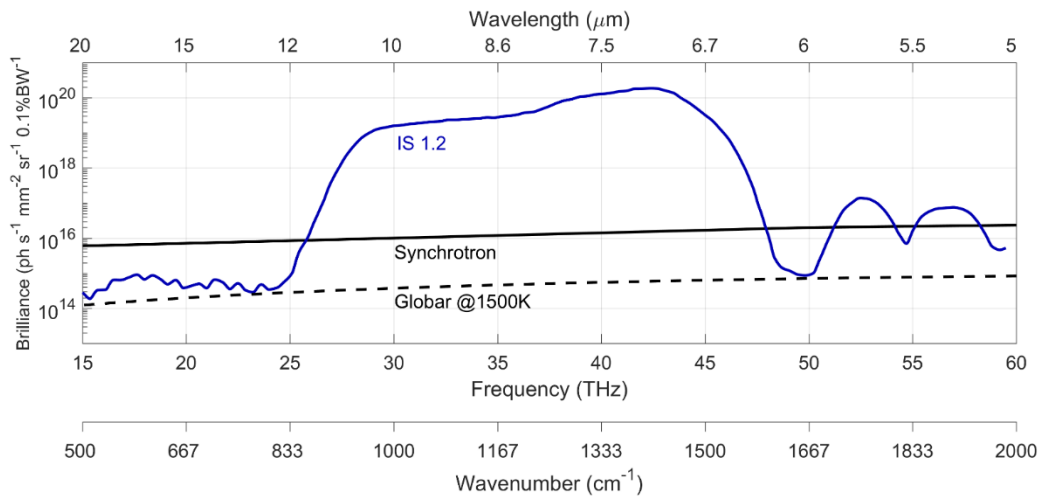
Figure 4.19 | Comparison of IS 1.2 source brilliance with conventional sources.

Chapter 5

Field-resolving spectrometer

The majority of table top, broadband MIR absorption spectroscopy measurements are performed with FTIR spectrometers employing thermal radiation sources[4,9,10]. Having matured over more than half a century, FTIR based setups have reached a performance plateau regarding dynamic range and sensitivity. Limitations relating to the poor coherence properties of thermal sources and the modest efficiency of broadband MIR detectors, as well as thermal background[96] render a significant further improvement of the performance of this technology rather unlikely.

Quantum cascade lasers (QCLs) and synchrotron sources, due to their high spectral brightness, have been shown to be advantageous over thermal radiation sources for use in vibrational spectroscopy of liquid samples[3,97]. However, QCL sources[98–100] have a limited coverage over the MIR spectral bandwidth due to their narrowband emission, while synchrotron sources[101,102], being extremely expensive to set up, are not readily accessible. In addition, the temporal coherence properties of both these sources are rather modest.

Field-resolved spectroscopy introduces the possibility of performing highly coherent, background-free, broadband molecular vibrational spectroscopy in a compact way. This scheme combines the experimental findings presented in chapters 3 and 4. The spectrometer employs a waveform-stable broadband femtosecond MIR source for the resonant excitation of molecules in a sample, and efficiently optimized EOS for field-resolved detection of the sample response. Section 5.1 describes the experimental implementation of the field-resolving spectrometer. The stability of the measured waveforms is characterized by EOS, and is presented in Section 5.2, and the utilization of the spectrometer for real-life applications is presented in Section 5.3.

5.1 Experimental setup

A detailed sketch of the experimental setup is shown in Figure 5.1. The NIR front-end is based on bulk compression in three stages (Section 0), in general providing better stability when compared to fiber-based compression schemes. The generation of broadband MIR based on IPDFG (Section 4.5) ensures high waveform stability, compared to OPA-based schemes employing separate pump and signal beams.
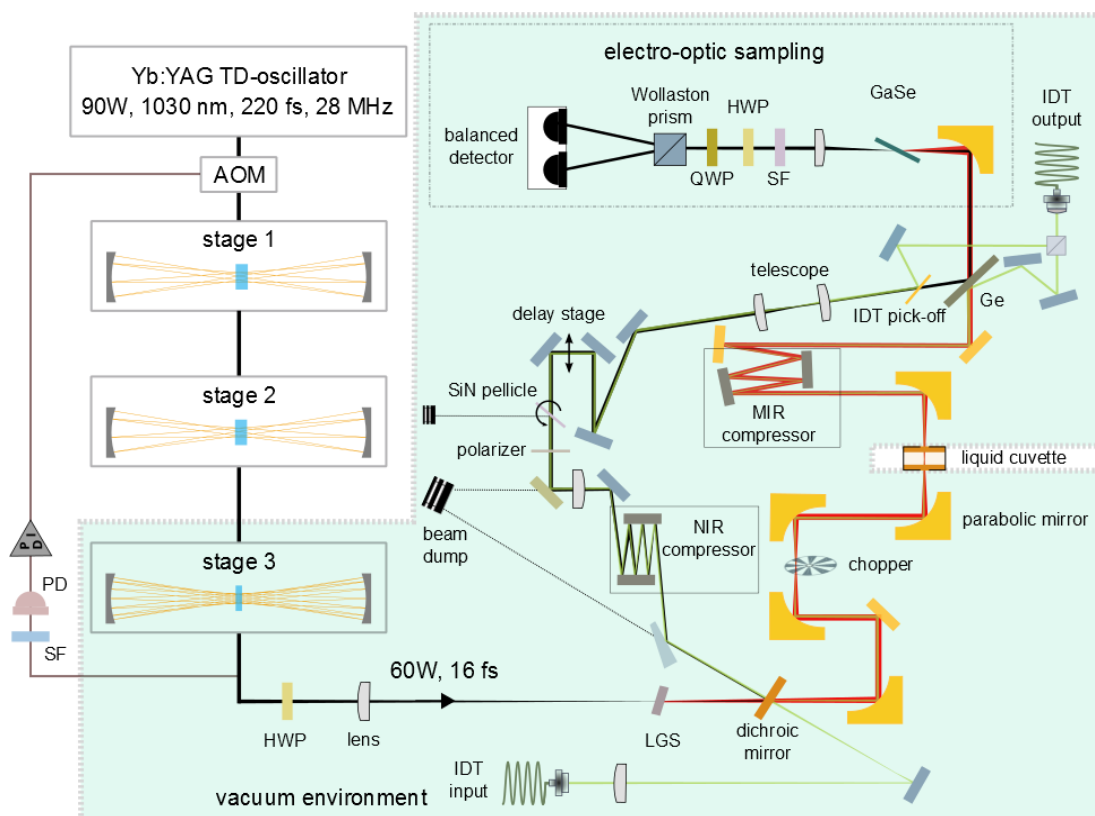
Figure 5.1 | Detailed sketch of experimental setup of the field-resolved spectrometer.
AOM, acousto-optic modulator; PD, photodiode; SF, spectral filter; HWP, half-wave plate;
IDT, interferometric delay tracking; SiN, Silicon Nitride; Ge, germanium beam combiner; GaSe,
gallium selenide; QWP, quarter-wave plate. For high power NIR beam after stage 3 custom
designed high-reflective mirrors were used, all mirrors in low power NIR beam after the dichroic
mirror were silver coated and bare-gold coated mirrors were used in the MIR beam path.

For the majority of the experiments presented in this chapter, 90 W of average power
were sent to the nonlinear compression stages, resulting in 16-fs pulses with 60 W of average
power available for MIR generation, at a repetition frequency of 28 MHz. The phase
matching of the IPDFG process resulted in an almost octave-spanning MIR spectrum
centred around 8.3 μm (1200 cm^{-1}). The MIR beam was chopped mechanically for lock-in
detection, and focused down for transmission through the liquid cuvette. The liquid cuvette
encloses a 34-μm long transmission path length for the liquid sample. For the liquid sample
subjected to the ultrashort MIR pulse, the impulsive excitation of the sample results in a
free-induction decay signal trailing the excitation pulse for several picoseconds.

5.1.1 Distinct features of FRS

FRS exhibits three distinct features as compared conventional absorption
spectroscopy techniques, namely a background-free advantage, detection in the NIR region,
and field scaling of the measured signal. These three features are discussed in the following.

a. Background-free advantage

The detection of molecular fingerprints in FRS is largely unaffected by MIR background, both from the radiation source and thermal background. The polarization response of molecules to an ultrashort, impulsive excitation can be described as the superposition of two contributions[31,103]: an instantaneous (non-resonant) part, characterized by a rapid amplitude decay owing to the impulsive excitation, and a resonant part induced by the dipoles oscillating coherently at the eigenfrequencies of the molecular sample, as a consequence of the impulsive excitation. The resonant part mainly contains sample-specific information and its decay time is given by the inverse linewidths of the excited molecular vibrations.

For the experimental setup, shown in Figure 5.1, the MIR beam accumulates dispersion from the IPDFG crystal, sample cuvetteand the germanium beam combiner, before EOS detection. The group delay (GD), and group delay dispersion (GDD) of the EOS pulse was evaluated for five EOS measurements from different days (Figure 5.2).
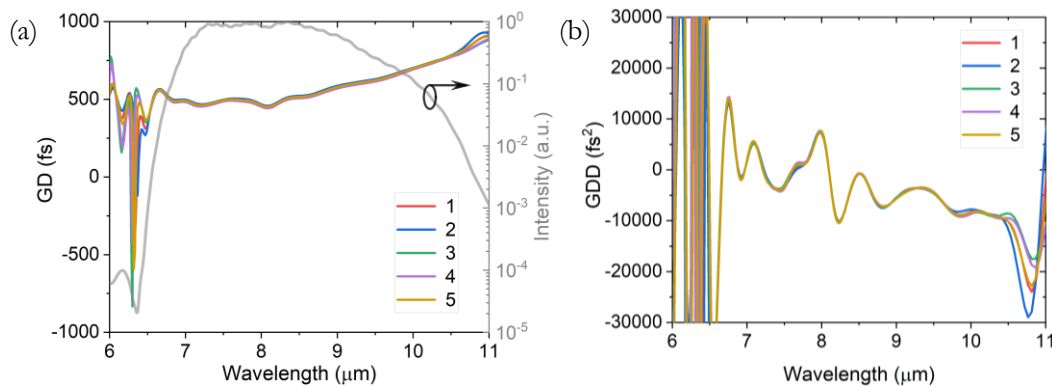
Figure 5.2 | MIR pulse dispersion. Group delay and group delay dispersion, evaluated from different EOS measurements. The grey curve shows the typical MIR spectrum for broadband detection.

A set of custom dispersive mirrors (DMs) based on multi-layers of Ge and YbF_3 were designed in house[104] to compensate the accumulated dispersion over the broadband MIR region. The choice of this combination of layer materials provides optimum performance in this spectral range. The commonly used combination of Ge/ZnS covers a rather narrow bandwidth[105], while a recently reported combination of ZnS/YbF_3 thin-film materials as a beam-splitter[106] is understood to be unsuitable for DM development, due to the ratio of their refractive index.

(a)

(b)
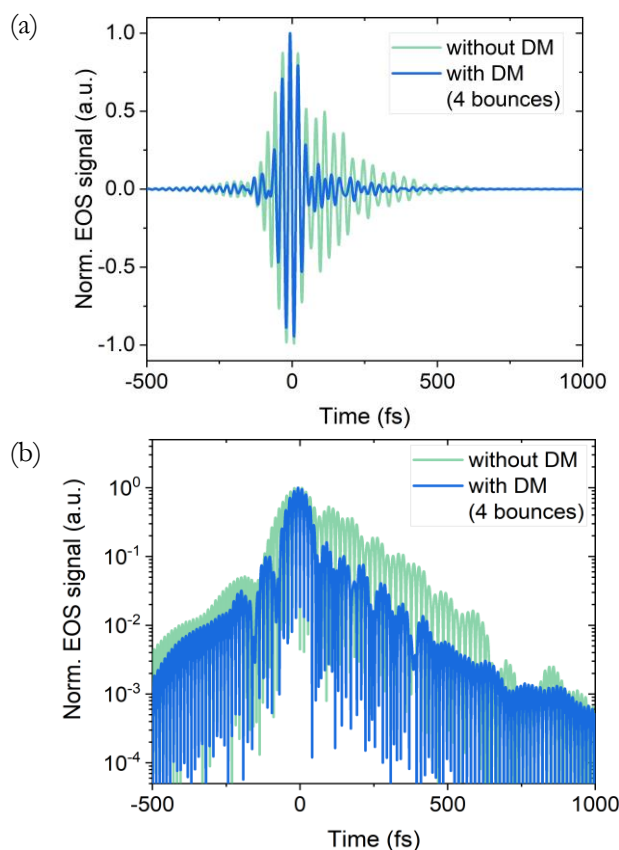
Figure 5.3 | MIR pulse compression. EOS signal with and without the MIR dispersive mirrors (DM), measured with an 85 μm-thick EOS crystal on a) linear scale, and b) logarithmic scale. The pulse was compressed from 85fs to 59 fs.

The thin-film combination employed here utilizes Ge as a high-refractive-index material and YbF_3 as a low-refractive index material. Four bounces over DMs were added to the beam path[*], for broadband EOS detection. The DMs enable the compensation of group delay variations of up to 400 fs over the spectral range from 6.5 to 11.5 μm. This resulted in a reduction in the full-width-at-half-maximum-intensity pulse duration from 85 fs to 59 fs (Figure 5.3). This compression of the instantaneous response results in a more prominent temporal separation of the molecular fingerprint signal from the excitation pulse, thus enabling the detection of weak molecular signals to be largely unaffected by the intensity noise of the excitation pulse.

b. Frequency up-conversion detection:

In EOS detection, the sample response is frequency up-converted to the NIR spectral region, and heterodyne measurement enables (close-to) shot-noise-limited detection of the NIR photons (Figure 4.15). The scheme thus avoids the use of relatively noisy MIR

---

[*] The implementation of the MIR chirped mirrors in the experimental setup was done by *Daniel Gerz*.

detectors, and benefits from the high-power NIR local oscillator, high detectivity and low noise semiconductor photodetectors at room temperature[107]. Furthermore, the up-conversion[78,79] of the fingerprint signal to the spectral range of the sampling pulse is confined to the duration of the interaction of the sampling pulse with sampled waveform in the EOS crystal, providing efficient temporal filtering against MIR thermal background.

c.   **Field scaling:**

Field-resolved detection in EOS gives access to the full temporal phase information of the MIR waveform. The signal strength scales linearly with the electric field of the measured MIR waveform instead of its intensity. For FTIR based spectroscopy, the transmitted path length is limited to <10 μm due to low source brightness and relatively noisy MIR detectors[108]. Relatively brighter sources, such as QCLs have limitations[98,99] in intensity noise and spectral bandwidth. This has important consequences for enhancing efficiency in measurements for strongly-attenuating and rapidly-dephasing molecular vibrations (e.g., in liquids etc.).

For a given analyte with absorption coefficient α and interacting length x, theoretical estimate shows a lower limit of detection for a wide range of interaction lengths (Figure 5.4). As the measured signal scales linearly with the electric field, it decreases with square root of the intensity attenuation. Field-scaling thus becomes increasingly advantageous for strong attenuations. Experimentally, this leads to sub-microgram per milliliter detection sensitivity for an 80-μm thick sample and a detection limit in the range of 10 micrograms per milliliter for 200-μm thick samples[34,37] for FRS measurement.

•   **Water background suppression:**

As MIR radiation is prone to interaction with water vapour and various other molecules present in the atmosphere, even a few centimetres of beam path in air will cause considerable background in the measurement. Figure 5.5 shows a 2D sonogram of the EOS measurement with a 500-μm thick EOS crystal. For a beam path of almost one meter, the measured signal exhibits a constant background signal around 7 μm, over several picoseconds. In order to suppress this unwanted molecular signal in the environmental background, the third NIR compression stage and subsequent stages of the beam path were pumped down and maintained at a vacuum level of a few millibar. This largely suppresses the water background signal (Figure 5.5b) in the wake of the impulsive excitation. Besides suppression of the water background, another benefit of keeping the beam path in vacuum is enhanced stability by avoiding air fluctuations.
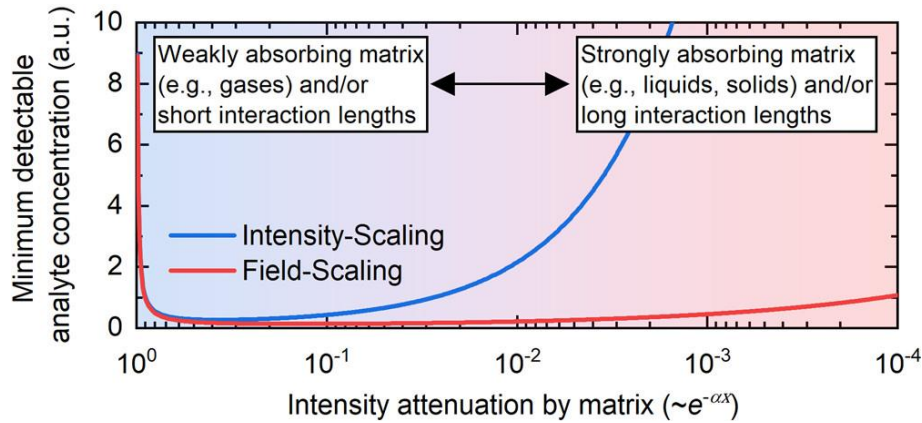
Figure 5.4 | Detection Limit with attenuation. Theoretical minimum detectable analyte concentration for field- and intensity scaling techniques. Figure is taken from Ref.[34].
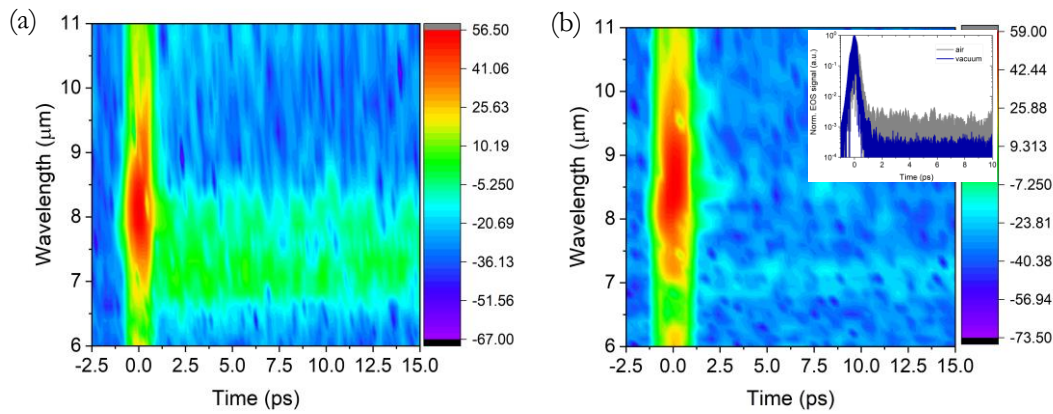
Figure 5.5 | Water background suppression. Contour map of EOS measurement in a) air and b) vacuum. The inset shows absolute normalized EOS signal for air and vacuum. After 1 ps from the maxima of the pulse, the background level is suppressed by almost an order of magnitude.

5.1.2 Sample cuvette

The sample cuvette is a commercially available unit (Micro Biolytics GmbH) consisting of two parallel 2-mm thick zinc selenide windows, along with an automated microfluidic delivery system. The original cuvette was supposed to be used in a free-standing form. In order to integrate the cuvette as a vacuum-compatible unit, homemade adapters (Figure 5.6) were designed to be glued onto the surface of cuvette window, and it was integrated between the two vacuum chambers along with MIR beam path. The air tightness of the cuvette limits the achievable vacuum level around 1mbar level, mainly due to the manual gluing process onto the small aperture of the cuvette window.
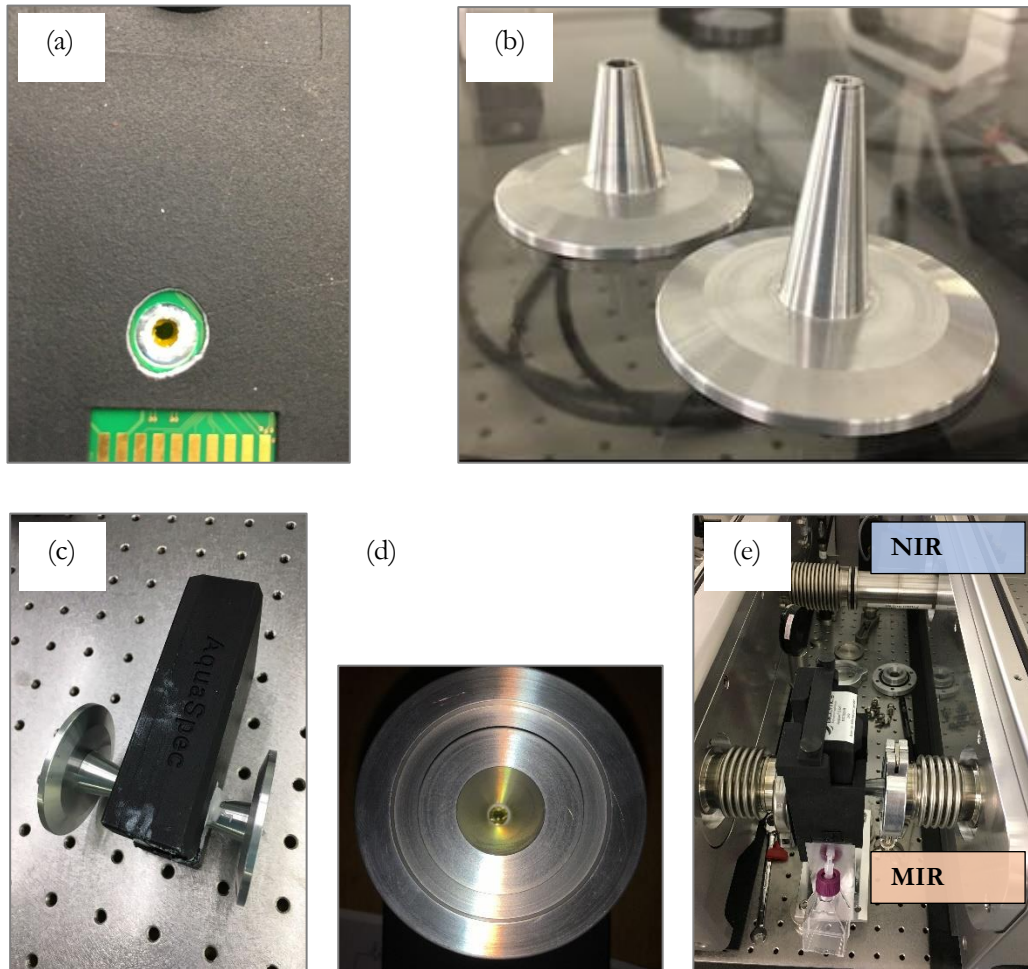
Figure 5.6 | Liquid cuvette and adapters for vacuum compatibility. a) Sample cuvette window with glue for connecting the adapter, b) homemade adapters with KF 40 flanges, each of the two sides has a slightly different design, c) side view of the cuvette with glued adapters, d) inward view through the glued adapter, and e) integrated liquid cuvette between the IPDFG and EOS vacuum chambers. The tunnel on top is for sampling the NIR beam. MIR beam was focused by using gold OAP mirrors on the liquid cuvette.

5.1.3 Instrument Linearity

The phase-matched frequency up-conversion process in EOS implies the existence of a trade-off between detected bandwidth and quantum efficiency. To demonstrate the capability to detect very weak signals, EOS was phase-matched at the central optical frequency in a 0.5-mm thick GaSe crystal. The thick detection crystal increases the detection efficiency, resulting in $\sim 10^{14}$ intensity dynamic range for a measurement time of 16 seconds. Additionally, the use of thicker EOS crystal also provides a larger measurement time window after the EOS pulse by avoiding internal reflections.

To demonstrate the linear response of the measurement, the MIR beam was attenuated using optical density filters (instead of the liquid cuvette). The instrument gives a

linear (in good approximation) instrument response over more than 10^7 in the electric field strength, and the intensity dynamic range scales in a linear fashion with measurement time (Figure 5.7). Dispersion in the OD filters causes slight variations in the pulse shape for different attenuations. The detection noise floor was obtained by blocking the MIR beam and the mean value of background noise was evaluated in the given spectral range. The noise floor also decreases linearly with measurement time. The demonstrated linear-response intensity dynamic range of ~10^{14} by sampling the MIR electric field instead of the average intensity, is several orders of magnitude higher than in typical infrared spectroscopy measurements[99].

Sampling the electric field along with high detection dynamic range enable highly efficient measurements for thick samples. This opens new avenues in vibrational spectroscopic applications involving biological samples such as bio fluids, living cells, and biological tissues.

5.2 Waveform stability of IPDFG with EOS

The control of phase of the optical carrier wave with respect to its intensity envelope brings high temporal and frequency resolution in optical experiments. The mode-locking mechanisms act on the optical intensity envelope rather than on the carrier electric field[109], such that the control of the latter requires additional measures. Phase control of ultrashort pulses is obtained either by actively-stabilised feed-back[20–22,110] or feed-forward[111–113] loops, or passively, via nonlinear optical conversion processes whose time-dependent polarisation follows the intensity evolution of the driving wave[23,114–116]. Active stabilization typically faces problems like complex experimental setups and limited bandwidths of the feedback loop. Furthermore, techniques like f-2f stabilization are affected by intensity fluctuations[117], since they rely on two nonlinear processes: supercontinuum generation and (second-)harmonic generation. Their use in a cascaded way results in a weak signal, limiting the measurement SNR. Additional optical gain is needed to improve the signal to noise ratio and thus the overall stability of the scheme[111].

The second-order (i.e., $\chi^{(2)}$) nonlinear process of IPDFG, intrinsically and passively performs this control, as the nonlinear polarization responsible for the emission of the difference-frequency wave follows the temporal intensity envelope of the driving pulse[23,25]. This has rendered IPDFG a preferred scheme for the generation of trains of waveform-stable ultrashort laser pulses and carrier-envelope-offset-frequency-controlled frequency combs in a number of applications[27,37,118].
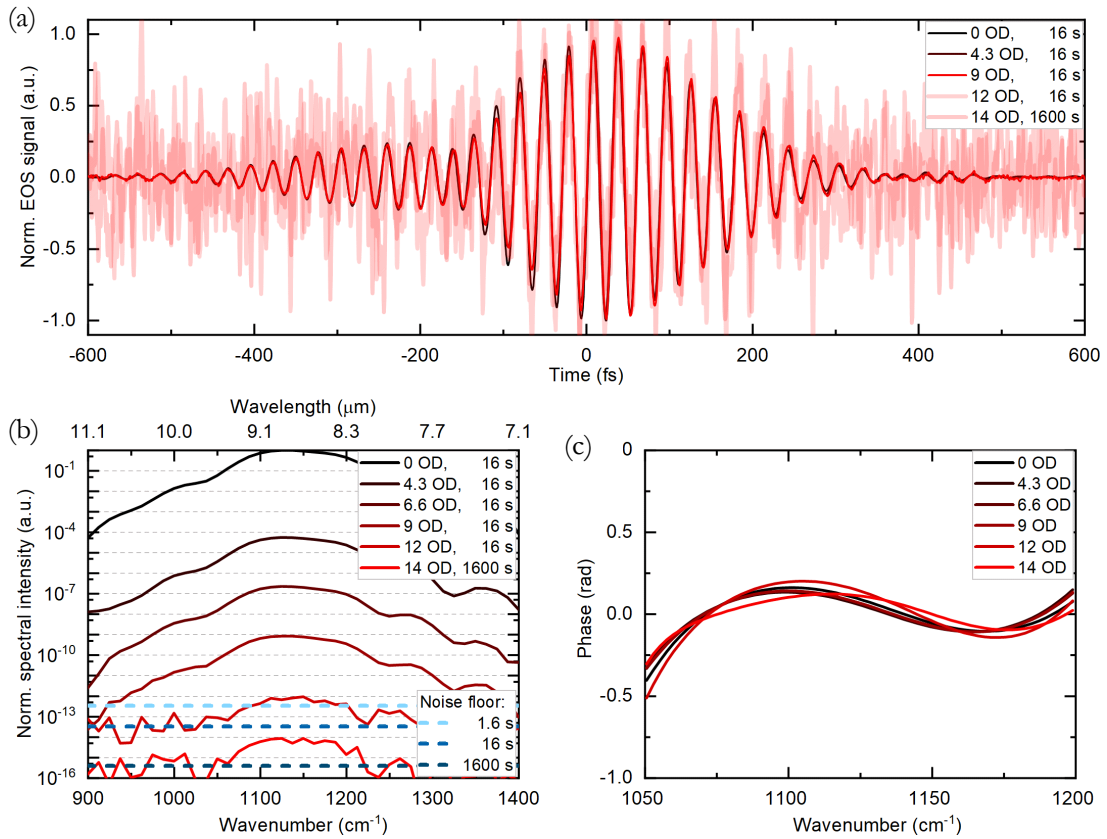
Figure 5.7 | EOS dynamic range and linear response of the spectrometer.[*] a) Normalized EOS pulse recorded with different optical density filters for a scan range of 1200 fs and with measurement time of 16s and 1600s. b) Normalized spectral intensity and noise floor for different measurement times, and c) corresponding phase.

To date, the values for the root-mean-square (RMS) carrier-envelope-phase (CEP) jitter reported in literature for laser pulses passively phase-stabilized via parametric processes lie in the range 20-220 mrad[24,119–122] and include the lowest reported for CEP-stable pulse trains. In light of the multiple (nonlinear conversion) processes used in the CEP noise measurement schemes, it seems likely that metrology itself has often represented a limitation, and that the waveform stability achievable with IPDFG can be orders of magnitude higher.

5.2.1 Measurement Principle

Here, we introduce EOS as a highly sensitive metrology technique for characterizing waveform stability, broadband both in the radio-frequency (RF) domain of the occurring noise/jitter, and in the optical domain of the laser pulses[123]. The direct measurement of optical waveforms, sampled with sub-optical-cycle temporal resolution grants access to both

---

[*] This measurement were taken and evaluated by *Ioachim Pupeza* and *Marinus Huber*, as presented in Ref [37].

the temporal jitter of the zero-crossings of the electric field of the carrier wave with respect to the gating pulse, and to the extrema of the field.

The intensity fluctuations of the front-end oscillator propagate through the self-phase modulation and IPDFG stages and are mainly responsible for the residual waveform noise of the resulting MIR pulses[124,125]. Because the wings of the near-infrared spectrum contribute most to the IPDFG process in a broadband phase-matching configuration, and their intensity is more susceptible to intensity fluctuations of the mode-locked oscillator output, a fraction of the blue part of the self-phase-modulation-broadened near-infrared spectrum was used to generate an error signal for active intensity-noise suppression with an AOM[50], presented in Section 3.1.1 and 3.1.3. The delay between the MIR and NIR pulses was tracked interferometrically with an auxiliary laser (IDT), with attosecond accuracy[93], explained in Section 4.5. This frequency-controlled distributed-feedback-diode-laser auxiliary beam at 1550 nm co-propagates along the interferometer arms with the exception of a ~10-cm distance necessary to circumvent the germanium beam combiner that is opaque at 1550 nm. The frequency-modulated beam allows the determination of the direction of delays, in contrast to a simple interference signal.
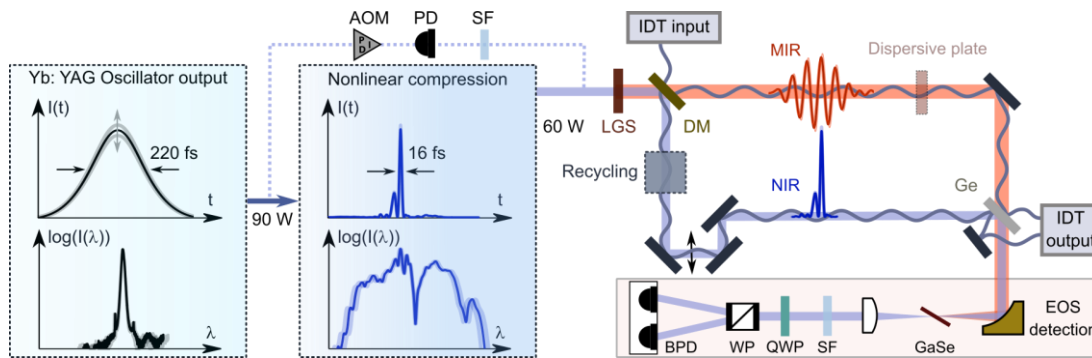
Figure 5.8 | Sketch of experimental setup for waveform stability measurements. Measured temporal intensity profile and spectrum of the Yb:YAG thin-disk oscillator output and the compressed NIR. 60 W of power in the NIR drives IPDFG in LGS. The NIR pulses are split from the emerging MIR beam with a dichroic mirror (DM), attenuated, recompressed and used as gate pulses for EOS detection; PD, photodiode; Ge, germanium; GaSe, gallium selenide; SF, spectral filter; QWP, quarter-wave plate; WP, Wollaston prism; BPD, balanced photodiode.

The experimental setup is sketched in Figure 5.8. IPDFG generates nearly-octave-spanning MIR waveforms spectrally centred at 8.1 μm with an average power in excess of 60 mW. For this characterisation, the liquid cuvette was removed from the setup. The 16-fs NIR pulses with an average power of 0.4 W and MIR beam with an average power of 20 mW were collinearly focused into an 85-μm-thick GaSe crystal for EOS detection. The heterodyne detection in EOS utilizes a short-pass-filter at 912 nm to increase the signal-to-noise-ratio[79]. The EOS data (output of the balanced photodetector) are taken with the IDT

electronics and, thus, with a common clock, such that the EOS and position data are automatically synchronised[93].
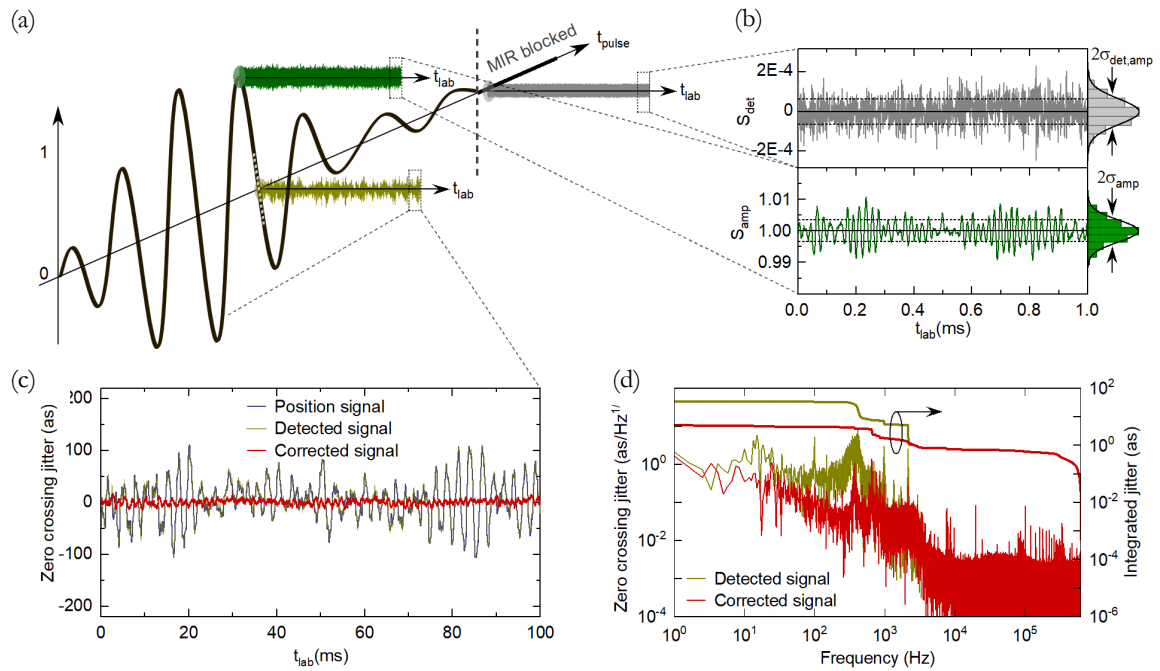
Figure 5.9 | Data acquisition and correction for waveform stability measurements. a) Typical EOS trace in the MIR pulse time frame (t_{pulse}). EOS data at fixed delays is measured for zero crossings (e.g., olive trace) and extrema (e.g., dark-green trace) in the laboratory time frame t_{lab}. For the blocked MIR beam, the detection noise is measured (grey trace). b) EOS data for the detector-noise signal, S_{det}, and a (local) amplitude-maximum signal, S_{amp} (the former was normalised to the mean of the latter), with their respective relative standard deviations $\sigma_{det,amp}$ and σ_{amp}. c) Measurement of the zero-crossing jitter: the EOS signal (olive) is corrected by the position signal (violet) via the EOS trace slope (gray-dotted line in a), yielding the zero-crossing jitter (red). d) Frequency-domain representation of the data for one-second measurement time. IDT position correction is applied below 3 kHz.

EOS traces of the MIR waveforms are recorded by varying the delay of the gate pulse (cf. axis t_{pulse} in Figure 5.9a), permitting the determination of the delay values for individual signal extrema and zero-crossings. At these fixed delay values of the waveform extrema and zero crossings, variations in EOS signal are recorded at a sampling rate of 1.25 MHz for one second (cf. axis t_{lab} in Figure 5.9a), limiting the maximum measurable frequency to 0.625 MHz (Nyquist theorem). For measurements at a zero-crossing, where the signal is most sensitive to delay variations in the interferometer, recording the interferometric delay/position (violet line in Figure 5.9c) in synchronization with the EOS signal (olive line in Figure 5.9c) shows a clear correlation between the two. The slope of the field at a specific zero crossing allows for a correction of the geometric path length jitter in the interferometer (red line in Figure 5.9c). For frequencies beyond 3 kHz, IDT position correction does not

improve zero-crossing statistics, such that the raw data (i.e., assuming a constant delay in the interferometer) is used for analysis above this frequency. Processing the time-domain data yields the RF-frequency-resolved noise, such as shown in Figure 5.9d for the example of the jitter of a field zero crossing.

5.2.2 Detection sensitivity

The high detection sensitivity for fluctuations of mid-infrared (MIR) waveforms results from the high dynamic range of the electro-optic sampling (EOS) detection setup. We determined the maximum detection sensitivity[*] (for the uncorrected data in the 10-kHz-to-0.625-MHz frequency band) as follows: Over the integration time per point (0.8 µs), given by the maximum sampling rate of the electronics (1.25 MHz), we measured the average amplitude values of the signal at the maximum of the EOS trace (i.e., delay $\tau = 0$), $\bar{S}_{\mathrm{max}}(0)$ (average: 4.8 V) and of the detection noise (average: 3×10^{-4} V), i.e. with blocked MIR beam. This results in an amplitude DR for the given measurement time of 16000. With both signals normalized to $\bar{S}_{\mathrm{max}}(0)$, the noise corresponds to the minimum detectable relative amplitude change $\sigma_{\mathrm{det,amp}}(0) = 6 \times 10^{-5}$, which is reduced for each extremum according to the normalized electric field envelope amplitude $\hat{A}(\tau)$: $\sigma_{\mathrm{det,amp}}(\tau) = \sigma_{\mathrm{det,amp}}(0)/\hat{A}(\tau)$. The timing jitter was measured by mapping the IDT-position-corrected amplitude jitter at a zero-crossing position to the time domain via the average slope of the optical waveform with angular frequency ω and amplitude A (approximation: $A \times \sin(\omega\tau) \approx A\omega\tau$ around the zero-crossing): $\Delta\hat{S}(\tau) = \hat{A}(\tau) \times \omega \times \Delta\tau$. Therefore, the minimum detectable timing- and amplitude-jitter values are related as follows: $\sigma_{\mathrm{det},\tau}(0) = \frac{\sigma_{\mathrm{det,amp}}(0)}{\omega}$, this gives $\sigma_{\mathrm{det},\tau}(0) \approx 0.5$ as.

To infer the fluctuations of the actual MIR field from EOS measurements, simulations were performed[†], to study the correspondence between the two. As the intensity noise of the oscillator propagates through the nonlinear optical process and causes phase noise in MIR pulses[124,125], we simulated the self-phase modulation based NIR pulse compression, IPDFG and EOS for various intensity levels of the soliton pulse emitted by the oscillator with the experimentally measured RIN value of 0.019 % (at >10 kHz). An absolute temporal reference for all fluctuations can therefore be given by the maximum-intensity instant of this soliton (while the experimental measurement gives the relative fluctuations of the MIR field and probe pulse). The simulations yielded two main conclusions:

---

[*] The mathematical formulism for sensitivity was derived by *Christina Hofer*.

[†] The simulations were performed mainly by *Christina Hofer* and *Maximilian Högner*.
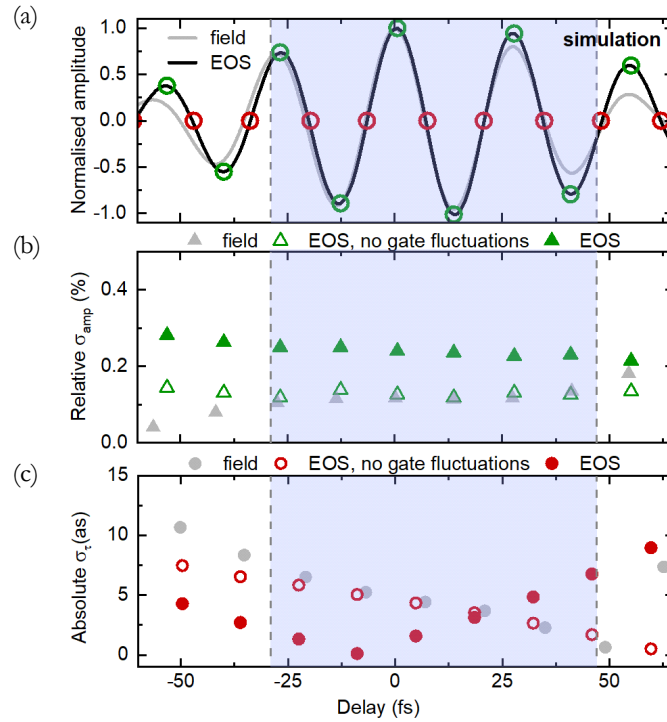
Figure 5.10 | Simulation of MIR electric field and EOS trace fluctuations. a) Electric field and EOS trace with typical spectral coverage (27 – 47 THz at -30 dB). The electric fields were calculated via IPDFG of 15-fs pulses emerging from a three-stage self-phase-modulation-based compression scheme. EOS was simulated with those fields and the same 15-fs pulses as a gate, in 85-µm thick GaSe rotated to 56.5°. This results in EOS spectra comparable to the experimental results. Empty circles: Selected extrema (green) and zero-crossings (red) for the jitter determination. b) Resulting relative amplitude fluctuations (relative standard deviation, σ_{amp}) of the field and of the EOS trace for an assumed RMS value of the soliton RIN of 0.019 %. Full triangles: gate pulse fluctuations on, empty triangles: gate pulse fluctuations off. c), Simulated absolute zero-crossing fluctuations for the field and EOS trace (absolute standard deviation, σ_τ) with gate pulse fluctuations on (full circles) and off (empty circles). The grey, dashed, vertical lines enclose the intensity-full-width-at-half-maximum duration of the MIR pulse (blue, shaded area). On average, the fluctuations of the gate pulses cause roughly a doubling of the fluctuations for our experimental EOS parameters. (Courtesy: Christina Hofer).

Firstly, for broadband EOS response functions (i.e., if the EOS trace closely resembles the IPDFG electric field) and assuming gate pulses to be free from fluctuations, there is an excellent agreement between the optical-field fluctuations and those of the EOS signal (Figure 5.10). *Secondly*, with gate pulse fluctuations included, the amplitude fluctuations are approximately doubled, most likely because both the EOS signal and the MIR field strength depend linearly on the gate pulse intensity[78]. As the MIR and gate pulses emerge from the same source, their fluctuations are correlated. This causes a minimum of the zero-crossing fluctuations, in this specific case close to the maximum of the EOS trace. The simulations predict average relative intensity and absolute timing jitter within the intensity-full-width-at-half-maximum of the MIR wave of 0.12 % and 4.45 as, respectively. This

implies a CEP-jitter of approximately 0.5 mrad. The order-of-magnitude increase of the amplitude jitter compared to the oscillator RIN can be attributed to the MIR wavelengths being generated by the wings of the broadened NIR spectrum that are more sensitive to changes in the oscillator intensity.

5.2.3 Compressed pulse characterization

For a temporally-compressed MIR pulse with a FWHM of 62 fs (Figure 5.11a), statistics for fluctuations at the waveform extrema and zero-crossings were obtained from five measurements at each delay point, and evaluated for frequencies up to 0.625 MHz as shown in Figure 5.11b,c respectively.

For the frequency band 10-kHz-to-0.625-MHz, we expect the interferometer jitter to be negligible, which is confirmed by the fact that interferometric delay tracking does not improve the zero-crossing statistics. For the cycles within the intensity FWHM, we obtain mean values of $\sigma_{amp} = 0.05$ % and $\sigma_\tau = 0.8$ as, respectively. These exceed by – on average – 5 and 1.8 times the detector sensitivity for the intensity and timing jitter, $\sigma_{det,amp}$ and $\sigma_{det,\tau}$ (grey shaded areas in Figure 5.11), respectively. The measured values agree reasonably well with those predicted in the simulations. The discrepancies between the two can be attributed to the wavelength selectivity of the AOM intensity stabilization (which was not taken into account in the simulations). From the correspondence between the jitter of the field and that of EOS traces discussed above, it can be inferred that the CEP fluctuations of the MIR electric field in our experiment are on the order of a few hundred µrad, which is significantly below the lowest values previously reported. Including the frequencies between 1 Hz and 10 kHz into the evaluation increases both the mean and the variation of the jitter values (Figure 5.11b, c). Most probably, this increase can be attributed to the influence of acoustic noise on the entire setup. Also, the detection sensitivity in this frequency range is limited by the accuracy of the IDT position data used for correction.

Furthermore, to study the effect of detection noise on the measurement, the EOS signal was attenuated electronically by a factor of ten, which leads to a reduction by a factor of three in amplitude dynamic range (due to different scaling of signal and noise with attenuation). For the full bandwidth (1-Hz-to-0.625-MHz), the attenuated measurement gave very similar values for zero-crossing and extrema in the centre of the pulse. In the wings of the attenuated pulse, the phase noise started to deviate when the EOS signal was a factor of 14 lower than at the maximum signal, while the relative amplitude noise stayed the same down to a factor of 30 in reduced signal. This shows, how a given dynamic range limits the detectable phase fluctuations more strictly then the amplitude changes.
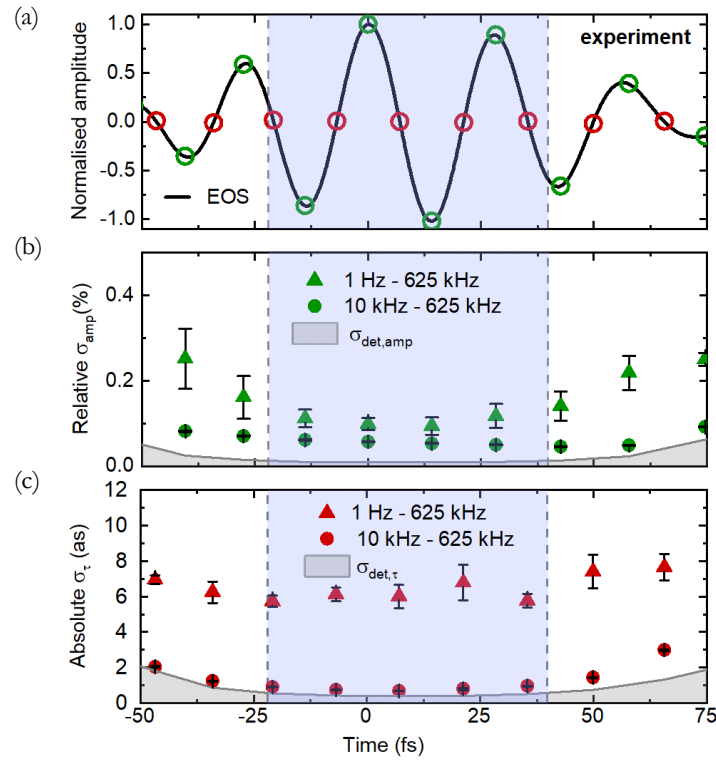
Figure 5.11 | Measurement of waveform fluctuations for a compressed MIR pulse. a, Measured few-cycle EOS trace. Empty circles: Selected zero crossings (red) and extrema (green). Blue shaded area: Range of intensity FWHM of the MIR pulse envelope. b, Measured amplitude noise across the pulse in the 1-Hz-to-0.625-MHz band (green triangles) and in the 10-kHz-to-0.625-MHz band (green circles). Grey shaded area: detection noise level (i.e., sensitivity) for the measurement of relative amplitude fluctuations, determined by the dynamic range of EOS detection. c, Temporal jitter for each selected zero-crossing of the EOS trace, in the 1-Hz-to-0.625-MHz band (red triangles), and in the 10-kHz-to-0.625-MHz band (red circles). Grey shaded area: Sensitivity for timing jitter measurements. For the 1-Hz-to-0.625-MHz band, the zero-crossing positions are corrected with the IDT position data up to 3 kHz, while for the 10-kHz-to-0.625-MHz band no correction was performed. The error bars in (b) and (c) indicate the standard deviation across five measurements each.

5.2.4 Chirped pulse characterization

To demonstrate the ability of our method to sensitively characterize waveform stability beyond the CEP model, we have inserted a 5-mm-thick CaF_2 plate in the MIR beam path, dispersing the short and long wavelengths along the (increased) pulse duration (Figure 5.12a,b). This grants access to the waveform fluctuations at different carrier wavelengths within the same pulse. For both the amplitude (Figure 5.12c, dark green) and zero-crossing fluctuations (Figure 5.12d, dark red), we observe a steady decrease with decreasing wavelength. We attribute this to the active intensity stabilization, whose error signal is derived from the blue part of the nonlinearly-broadened NIR spectrum, which in IPDFG contributes more to the short MIR wavelengths. This is confirmed by the result of turning

off the active intensity stabilisation, which increases both the amplitude and zero-crossing fluctuations predominantly for the shorter wavelengths (Figure 5.12c,d, light green/red). It is noteworthy that differences in the mean values of the zero-crossing jitter of less than 1 as can be measured in a wavelength-resolved fashion.
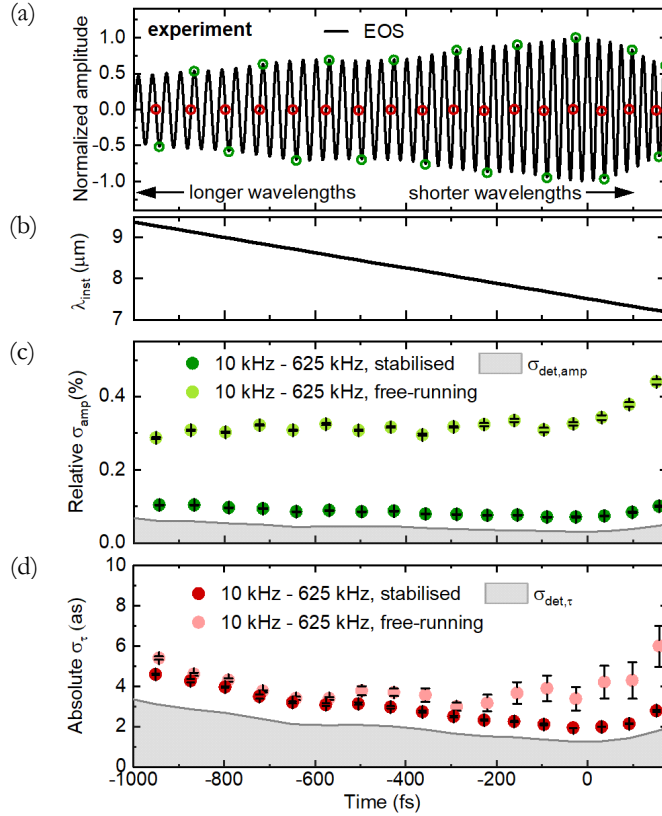
Figure 5.12 | Measurement of waveform fluctuations for a chirped MIR pulse. a) Measured EOS trace of a chirped pulse. Empty circles: selected zero-crossings (red) and extrema (green). b) λ_{inst}, Instantaneous wavelength variation over the chirped pulse. c) Measured amplitude noise across the pulse in the 10-kHz-to-0.625-MHz band, with AOM-stabilization on (dark green circles) and off (light green circles). d) Temporal jitter for each selected zero-crossing of the MIR waveform, in the 10-kHz-to-0.625-MHz band, with AOM-stabilization on (dark red circles) and off (light red circles). Grey shaded areas: detection limit, analogous to Figure 5.11.

These experiments validates high-dynamic-range EOS as a broadband – in both the radio- and the optical-frequency domains – and high-sensitivity measurement technique for optical-waveform stability. As a first application, we have confirmed the CEP stability of IPDFG with an order-of-magnitude improved sensitivity compared to previous reports. Furthermore, we have detected wavelength-dependent temporal jitter with variations on the order of 1 attosecond within an ultrashort mid-infrared pulse and explained their origin.

5.3 Towards real-world applications

The unprecedented passive waveform stability, confinement of the infrared field to sub-two-cycle pulse with intensity FWHM of ~60 fs, robustness against thermal background, and high dynamic range of detection, render this instrument ideal for field-resolved infrared vibrational spectroscopy of strongly absorbing samples, such as biofluids, biological tissues, and live cells, as well as in frequency-comb spectroscopy of gases. Ultrashort pulses are transmitted through the sample, and the waveforms are measured with EOS. The spatial distribution of microscopic charges (nuclei and electrons) in the organic sample is inhomogeneous and characteristic of the molecular species. The interaction of infrared field with molecules induces microscopic charge separation in space, due to electric dipole moments. The oscillating electric field drives the time evolution in these dipoles. The microscopic dipole oscillations occur with characteristics frequencies and magnitude, with fixed mutual timings, set by the excitation field. These resonant vibrations keep oscillating after excitation by few-cycle infrared pulse, constituting a molecular fingerprint. This resonant signal contains sample-specific information, as coherent superposition of the resonating sample oscillating fields.

The spectrometer, named as Infrasampler 1.2 (IS 1.2), was commissioned to the in house collaboration Broadband Infrared Diagnostic (BIRD) group, for the investigating of bio-fluids. In the next subsection, first studies done with this instrument are presented. The samples under investigation were prepared by the BIRD team (led by Mihaela Zigman), measurements and analysis by the team[37] including *Ioachim Pupeza, Marinus Huber, Michael Trubetskov, Wolfgang Schweinberger.*

5.3.1 Attosecond-timed molecular signals

For the investigation of a given molecular sample, sensitivity and specificity of field-resolved molecular fingerprints critically depends on temporal coherence of the fingerprint signal and its reproducibility over the measurement time. For the liquid-phase samples, coherent molecular signal typically survives for several picoseconds[31]. Field-resolved molecular fingerprint of human blood serum was measured with quantum-efficiency optimised EOS (grey curve in Figure 4.18).
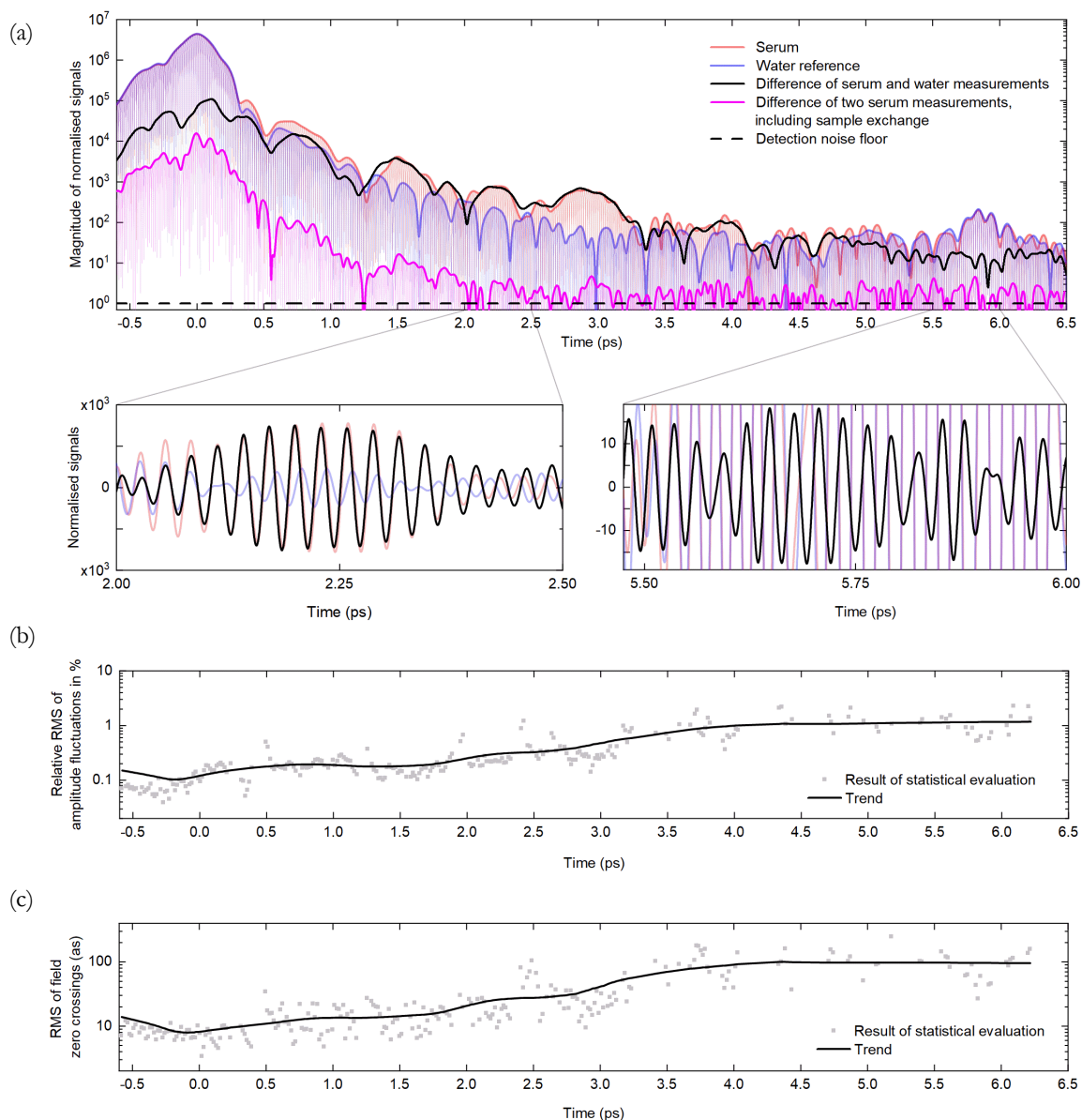
Figure 5.13 | Molecular fingerprint signals of human blood serum and their reproducibility. a) Magnitude of the EOS signals for blood serum, water and their difference. Linear scale representation of the EOS signals of main panel in different time windows. For five hundred consecutive measurements of the molecular fingerprint of a serum sample: b) Relative RMS of the oscillation amplitude and c) absolute RMS of the zero-crossings. Figure is taken from Ref. [37].

Figure 5.13 a,b show the time-resolved fingerprint signal of human blood serum, and differential signal by subtracting the blood serum signal from pure water signal. This bio-molecular signal decays by a few orders of magnitude within a few picoseconds. This reveals the dephasing time of bio-molecular vibrations in blood serum far below one picosecond. The blood serum was measured five hundred times consecutively for the same serum sample (each scan taking 4.5 s). The individual EOS traces were aligned in time using a one-parameter (time shift) optimisation. Furthermore, a one-parameter amplitude correction of

all traces to the maximum amplitude of the first measurement was performed, allowing for a compensation of minor, slow drifts of the laser intensity with time. Subsequently, the traces were frequency-filtered by a 20th order super-Gaussian filter suppressing any noise outside the spectral window 900–1450 cm^{-1}. For each trace, in steps of a few field oscillations, a sinus curve of ~1.5 oscillations was fitted with respect to 4 parameters: amplitude, amplitude offset, frequency and phase. The relative amplitude noise and the absolute timing jitter of the zero crossings, shown in Figure 5.13 c and d, respectively, were obtained by evaluating the statistics of the amplitude and phase fit parameters, respectively. Because the oscillating EOS trace exhibits regions of strong deviation from a sinus function (e.g., due to the temporal evolution of the molecular fingerprint signal), the fits with relative errors larger than 3 % are excluded. This resulted in the grey dots in Figure 5.13 c, d. The black, continuous lines indicate a trend, calculated by interpolating the grey points with an 82-point LOWESS filter (OriginPro 2017). Within the first two picoseconds following the main excitation, the relative RMS deviation of field oscillations amplitude form its mean value of ~0.2 % and an absolute RMS of the zero crossings of the infrared molecular fingerprint field of ~20 attoseconds (Figure 5.13 c,d). This reproducibility enables suppression of the infrared electric field background by up to three orders of magnitude compared to the reference field. This implies a background-free measurement after ~2 picoseconds following the excitation pulse peak, in a highly complex biofluid such as blood serum in a field-resolved fashion.

5.3.2 Sensitivity and specificity

The utilization of the spectrometer for biomedical applications greatly depends on its capability to distinguish smallest changes in molecular concentrations of the sample. The molecular fingerprinting needs to probe small changes in the chemical composition of the sample under investigation. Different concentrations of methylsulfonylmethane ($DMSO_2$) in serum sample (BioWest, Nuaillé, France) was measured to assess the smallest concentration level[*]. For each prepared concentration, 900 μl of serum were mixed with 100 μl of $DMSO_2$ in pure water. Subsequently, 1000, 100, 50, 10, 5 and 0 μg/ml of $DMSO_2$ solution were used to obtain spiked serum samples with 100, 10, 5, 1, 0.5, 0 μg/ml $DMSO_2$ concentration, respectively. These samples were measured with FRS (IS 1.2) as well as with FTIR. In order to avoid systematic effects in the sample preparation that might lead to a separation in the subsequent principal component analysis, each concentration of spiked serum was prepared 5 times independently. Concentrations below 10 μg/ml were measured at least 8 times. For FTIR measurements 0.5 μg/ml was excluded, as the previous experiment showed that this is below the limit of detection of our FTIR.

---

[*] These measurements and their evaluation were led by *Marinus Huber*.

Figure 5.14a shows the mean and relative standard deviation of the different concentration sets for repeated measurements of the samples, along the first principal component. The error bars show the capability of FRS for detecting changes in the concentration level down to 200-ng/ml level in human blood serum. This shows almost an order of magnitude improvement as compared to the research grade FTIR spectrometer. Hence, currently detectable smallest changes are more than 5 orders of magnitude below the concentration of the most highly abundant constituent of this biofluid, albumin[126]. This implies a concentration dynamic range in excess of 10^5, directly detectable without depletion of high-abundance molecules. While the relative intensity noise of the excitation does not affect the FRS detection limit with a spectrally isolated feature, the lowest detectable concentration of the same specimen *in a complex environment* is limited by the relative intensity noise of the overall molecular fingerprint signal. This, in turn, is likely to be dominated by the noise of the excitation source. As an important consequence, the current FRS concentration dynamic range of 10^5 offers substantial room for further improvement by suppressing the noise of the molecular fingerprint signal. An efficient measure to this end may be "freezing" the excitation source noise by scanning faster than the characteristic time of intensity fluctuations[84,127].

To study the *specificity* of the measured fingerprints, i.e., the sensitivity to small changes in *relative* concentrations, aqueous solutions of two different sugar molecules of constant total concentration, and varying relative concentrations were prepared. The measurement was performed with the bandwidth-optimised setting of the spectrometer, covering the spectral range between 900 cm^{-1} and 1524 cm^{-1} at -20-dB intensity. With this setting, the intensity dynamic range of detection was roughly 100 times lower than with the previous setting. Two sugars specimens, maltose (D-Maltose; Serva Electrophoresis GmbH) and melibiose (D-(+)-Melibiose; Sigma-Aldrich) were mixed in pure water at a constant total concentration of 100 μg/ml and at varying relative concentrations. Both of these sugars have similar spectral fingerprints. The total concentration of 100 μg/ml was chosen well above the limit of detection of both instruments. The data in Figure 5.14b reveal that FRS outperforms FTIR spectrometry in sensing not only small absolute changes but also relative changes in concentration of molecules of a complex ensemble.
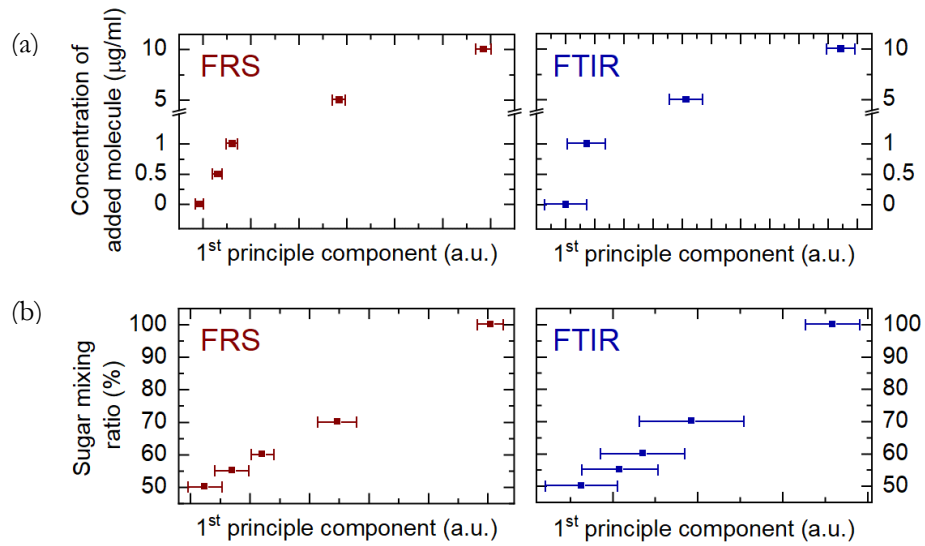
Figure 5.14| Sensitivity and specificity of complex fluids. a) PCA analysis for different concentrations of $DMSO_2$ in human blood serum, measured with FRS and FTIR, b) PCA analysis for a mixture of two sugars dissolved in water with constant total concentration and varying relative concentration, measured with FRS and FTIR. Figure is taken from Ref. [37].

Chapter 6

Conclusion and Outlook

The results presented in this thesis established the foundations of world's first laser instrument to perform highly-sensitive, broadband optical-field-resolved spectroscopy. The proof-of-principle experiments show a sensitivity surpassing that of commercial Fourier-transform infrared spectrometers by more than a factor of 40. Field-resolved spectroscopy of molecular vibrations requires three main ingredients. *Firstly*, is necessitates a highly-stable source of broadband mid-infrared light. This was accomplished by utilizing a bulk-broadening based near-infrared (NIR) frontend driving intra-pulse difference frequency generation (IPDFG) of an almost-octave-spanning mid-infrared (MIR) spectrum centred at 8.1 μm, with an average power of >50 mW. *Secondly*, a field-resolved detection scheme was realized by setting up electro-optic sampling (EOS). EOS detection was optimized for the maximum NIR power to the EOS crystal (limited by the crystal damage threshold), the size of NIR and MIR beams at the common focus, phase matching conditions and balanced detection. This resulted in shot-noise-limited balanced, high-quantum-efficiency EOS. *Thirdly*, high stability and reproducibility of the measured electric field waveforms is necessary. This requires both the generation and detection to be highly stable. IPDFG was found to have superior intrinsic stability compared to optical-parametric-amplification schemes employing separate signal and pump beams. In addition to the optimum EOS signal detection, the delay was tracked interferometrically along the NIR and MIR beam paths, instead of tracking only the delay stage.

High-quantum-efficiency EOS[94] was validated to be a broadband – in both the radio- and the optical-frequency domains – and highly sensitive metrology technique for optical-waveform stability. The measured waveforms were characterized and the pristine stability of the IPDFG was validated with an order-of-magnitude improved accuracy compared to previous measurements[114,115], reporting the – to the best of our knowledge – most phase-stable train of ultrashort light pulses to date. This certifies the need of highly-stable passive frontend sources for high-precision metrology, whether for a direct field-resolved application or as a seed for strong-field laser physics. Furthermore, wavelength-dependent temporal jitter variations on the order of 1 attosecond within an ultrashort pulse were measured and their origin was tracked back to the excessive intensity noise of the modelocked oscillator, showcasing the ability of the EOS-based metrology to characterise waveform stability beyond the carrier-envelope-phase model.

Highly phase-stable few-cycle MIR sources together with high-sensitivity sub-optical-cycle waveform sampling are instrumental for further developing time-domain, field-

resolved spectroscopy. For instance, our study promises that increasing the scan rate[84,128] from <1 Hz to >10 kHz in field-resolved infrared molecular fingerprinting of complex samples[37] will considerably improve the reproducibility of individual waveform scans, improving the visibility of low-abundance molecular constituents. In addition, the passive, high phase stability demonstrated here, together with nonlinear frequency upconversion[129,130] show a route towards the generation highly-stable near-infrared and (therewith) extreme-ultraviolet frequency combs[131].

Building on the results and insights presented in the thesis, the following directions of further development promise a substantial increase of the impact of field-resolved infrared spectroscopy in the near future.

6.1 Spectral coverage

The sample response for living cells and biomolecules is rather broadband and even the octave-spanning spectral coverage demonstrated here only partially covers the vibrational frequencies of proteins and carbohydrates. An interesting spectral region that is not covered in these experiments lies between 3 and 6 μm, corresponding to the characteristic vibrational modes for lipids. This requires the extension of the bandwidth of the driving NIR pulse for the generation of the idler beam at shorter wavelength, and a study of the phase-matching configuration of different nonlinear crystals.

MgO-doped periodically poled lithium niobate (MgO:PPLN) crystals with a poling period in the range of 23 μm to 28 μm would be potential candidates for MIR generation in this spectral region[132,133]. Preliminary experiments showed that MIR light centred at a wavelength of 4.5 μm, as shown in Figure 6.1, can be generated with a driving NIR pulse similar to the one presented in Section 3.1.3[*]. Further bandwidth in the driving NIR beam would be needed to reach shorter MIR wavelengths.

6.2 Intra-scan referencing

Real-life spectroscopic applications require the sample and the reference measurements to be performed close to each other in time. In the data processing, the two measurements are either subtracted or deconvolved/divided to obtain high-signal-to-noise-ratio sample-specific information. Such data processing is sensitive to the technical noise occurring on a time scale of a few seconds which is typically necessary to switch between the

---

[*] This experiment was performed on *Infrasampler 1.5* setup, the frontend provides slightly broadband NIR pulses, as compared to the NIR pulses presented in in Section 3.1.3. The experiment was performed with the help of *Theresa Buberl*.

sample and reference measurement. Moreover, it restricts standardization of the measurements performed under slightly different conditions. In principle, this issue can be tackled by decreasing the time between the two measurements by an intra-scan referencing (ISR) scheme and/or by fast-scanning techniques. ISR was implemented in the Infrasampler 1.2 setup, as a proof-of-principle experiment.
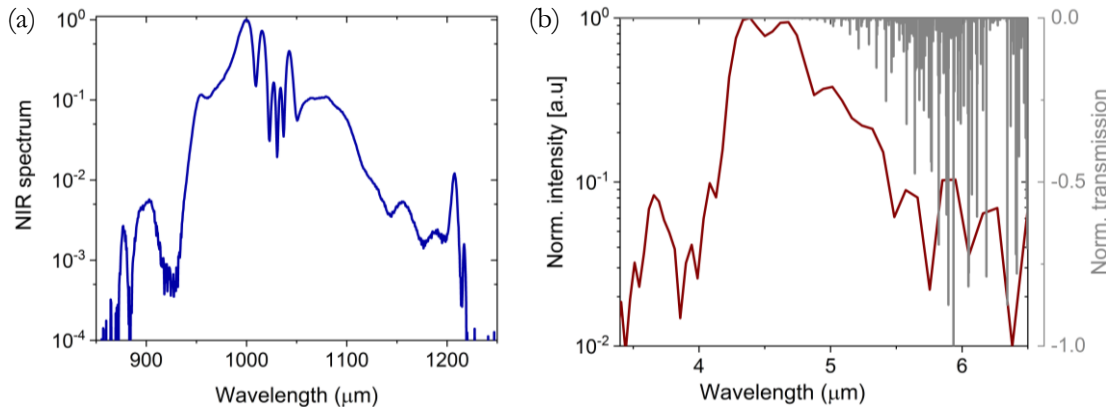
Figure 6.1 | Driving NIR spectrum and MIR spectrum generated in PPLN. The grey lines in the right panel shows water absorption lines in this spectral range. This experiment was performed in air, so the measured spectrum is attenuated by both the absorption from water in air as well as from the crystal absorption beyond 5 μm.
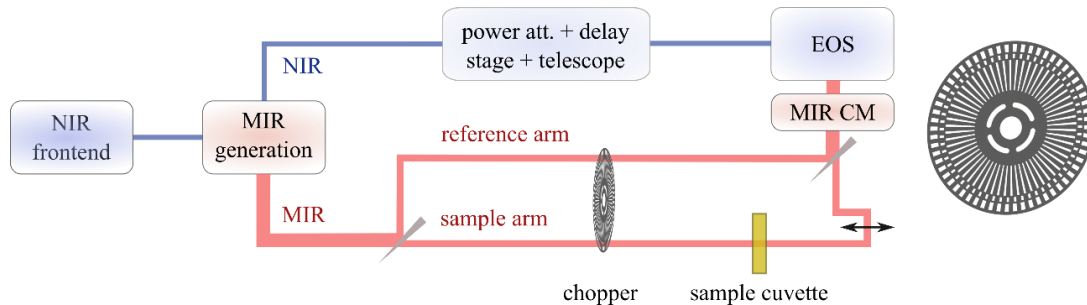
Figure 6.2 | Sketch of the intra-scan referencing scheme. MIR beams were separated before the chopper wheel and recombined after the sample cuvette by using ~0.5-mm thick diamond wedged windows. Right panel: design of custom chopper wheel used for chopping in ISR scheme.

The MIR beam was separated into two arms by using a very thin (~0.5-mm) diamond wedged window, such that only one MIR beam goes to the sample cell serving a sample arm and the other beam is used as a reference arm. The sample-arm and reference-arm beams were chopped such that there is a constant phase shift between the times each of the two are blocked. This could be done either by using two mechanical choppers synchronised for the given phase shift, or a specially-designed chopper wheel of a single optical chopper. The

chopper wheel with 60 slots, shown in Figure 6.2, was designed[*] for the commercial optical chopper previously used in the experiment (Newport optical chopper 3502). The outermost ring is used by the chopper controller itself for speed feedback, the next ring for the sample MIR beam, and the inner ring for the reference MIR beam.

The MIR beams were focused on the chopper by using bare-gold off-axis parabolic mirrors to avoid any distortions. Both of the MIR signals were measured with EOS, a delay stage was introduced in one of the MIR beam paths so that the two MIR pulses could be shifted relative to each other. The position of the MIR delay stage was adjusted, such that both of MIR pulses lied very closely to each other. Figure 6.3 shows the first interleaved EOS measurement of both MIR pulses. The beams were chopped with a frequency of 5.7 kHz, with a data acquisition rate of 312.5 kHz, corresponding to 54 points per chopping cycle. The inset shows raw data for two chopping cycles. The lower plateau of points corresponds to the reference MIR pulse (green circle), the centre plateau to the zero-base line (grey circle), and upper plateau to the sample MIR pulse (purple circle).
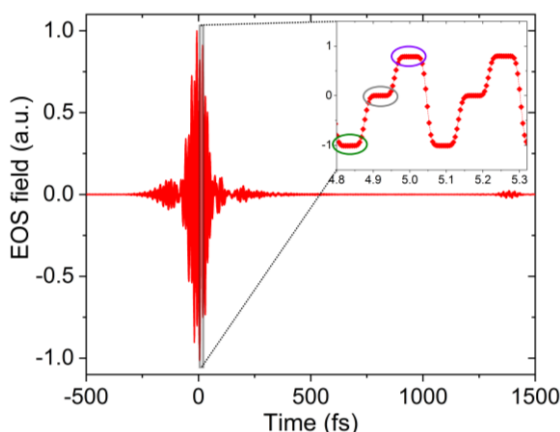
Figure 6.3 | EOS measurement of interleaved MIR pulses. The inset shows the set of data acquisition points for two chopping cycles. Green circle for the data points of reference MIR pulse, grey circle for the data points zero-base line, purple circle for the data points of the sample MIR pulse.

The ISR technique promises a higher SNR compared to the conventional measurement technique, in particular for longer measurement times (that is necessary for any real-life application measurement campaign). To demonstrate the ISR performance, a measurement campaign was performed[†] for 1-mg/ml concentration of $DMSO_2$ solved in water, measured in a 35-μm cuvette, and subsequent measurements of water. Figure 6.4

---

[*] The chopper wheel used here was designed by *Alexander Weigel*, and is shown in right panel of the Figure 6.2.

[†] These measurements were performed along with *Wolfgang Schweinberger*, and the data evaluation shown in Figure 6.4 was performed by *Michael Trubetskov*.

compares the deviation of the standard transfer function (spectrum and phase) for conventional scheme, and ISR scheme (with inter-leaved EOS traces of sample and reference arm, as shown in Figure 6.3). For the conventional scheme, the transfer function was calculated in the frequency domain from the measured averaged EOS traces of $DMSO_2$ and water. For the ISR evaluation, the transfer function was calculated from the measured averaged EOS traces of $DMSO_2$ and water, each referenced to the interleaved averaged EOS trace first, obtained from the reference arm. The same dataset was used in these evaluations, and ISR reference-arm measurements were discarded for the conventional scheme. Despite being in the very early development stages, these results attest to the promise of the ISR scheme for spectroscopic studies in real-life applications.
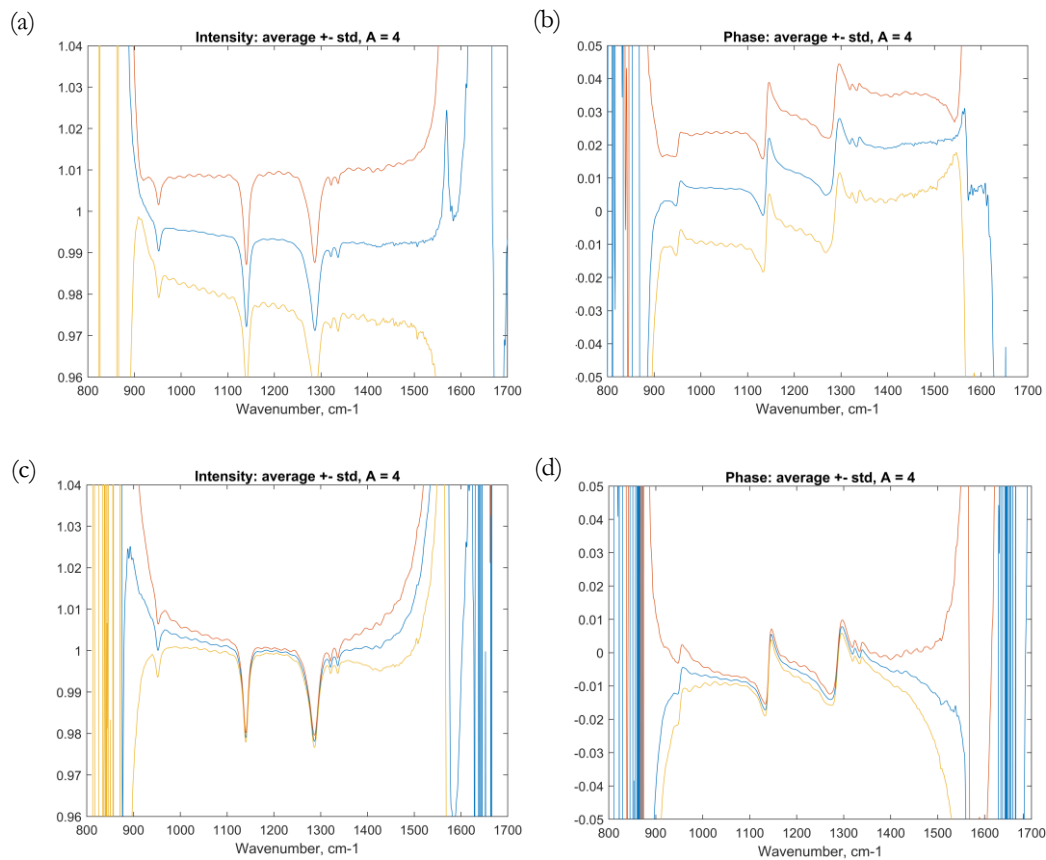
Figure 6.4 | First ISR measurements campaign. Comparison of the standard deviation of the transfer functions for conventional scheme a) intensity and b) phase and for ISR scheme c) intensity and d) phase. The variable A indicates the number of average transfer functions.

6.3 Precision time-domain optical metrology

The waveform stability characterization provides a promising route various nonlinear precision measurements. The demonstrated sub-attosecond real time field measurement could be combined with an induced nonlinear polarization measurement. The nonlinear polarization will induced the temporal change in the electric field cycle period. The z-scan of a very thin plate of MIR window (such that Ge or ZnSe) in the focus of the MIR

beam and recording the transmitted waveform at different intensity levels. The sub-attosecond timing precision of the zero crossings will translate into a precision measurement of the (quasi-instantaneous) nonlinear response of the electronic polarization and, thereby that of the nonlinear index of refraction. This promises to measure the nonlinear refractive index with unprecedented accuracy. Similarly, the transmitted waveform measurement of the z-scan an organic sample dissolved in water would have the retarded molecular response at different intensity levels. This may reveal miniscule changes of the vibrational response of an organic molecule with varying peak intensity of the excitation. This would give access to the (delayed) nonlinear response of the nuclear polarization, providing thereby insight into the anharmonicity and possible nonlinear coupling between vibrational modes with never-before achieved accuracy. Moreover, by employing fast scanning scheme, if the relative electric field period clocking clocking could be improved to zeptosecond level, this would allow to measure nonlinear phase shift of the order of $\sim \pi/10^5$ level.

Data Archiving

The experimental raw data, evaluation files, and figures can be found on the Data archive server of the Laboratory for Attosecond Physics at the Max Planck Institute of Quantum Optics:

//afs/ipp-garching.mpg.de/mpq/lap/publication_archive

The main folder Syed Ali Hussain contains two sub-folders Data and Figure, which contains all the raw data and figures, saved as chapter sub-folder. Each sub-folder, a readme file can be found which contains the detailed description of the raw data, and about figures.

Bibliography

1. Demtröder, W. *Molecular Physics: Theoretical Principles and Experimental Methods*. (Wiley-VCH, 2005).

2. Krausz, F. & Ivanov, M. Attosecond physics. *Rev. Mod. Phys.* **81**, 163–234 (2009).

3. Baker, M. J. *et al.* Developing and understanding biofluid vibrational spectroscopy: a critical review. *Chem. Soc. Rev.* **45**, 1803–1818 (2016).

4. Lasch, P. & Kneipp, J. *Biomedical Vibrational Spectroscopy*. (Wiley-Interscience, 2008).

5. Nie, S. M. & Emery, S. R. Probing single molecules and single nanoparticles by surface-enhanced Raman scattering. *Science* **275**, 1102–1106 (1997).

6. Movasaghi, Z., Rehman, S. & Rehman, I. U. Raman spectroscopy of biological tissues. *Appl. Spectrosc. Rev.* **42**, 493–541 (2007).

7. Jones, R. R., Hooper, D. C., Zhang, L., Wolverson, D. & Valev, V. K. Raman Techniques: Fundamentals and Frontiers. *Nanoscale Res Lett* **14**, (2019).

8. Kneipp, K., Kneipp, H., Itzkan, I., Dasari, R. R. & Feld, M. S. Surface-enhanced Raman scattering and biophysics. *J. Phys.-Condes. Matter* **14**, R597–R624 (2002).

9. Barth, A. & Haris, P. I. *Biological and Biomedical Infrared Spectroscopy*. (IOS Press, 2009).

10. Griffiths, P. R. & Haseth, J. A. D. *Fourier Transform Infrared Spectrometry*. (John Wiley & Sons, 2007).

11. Baker, M. J. *et al.* Using Fourier transform IR spectroscopy to analyze biological materials. *Nature Protocols* **9**, 1771–1791 (2014).

12. Haus, H. A., Fujimoto, J. G. & Ippen, E. P. Structures for additive pulse mode locking. *J. Opt. Soc. Am. B, JOSAB* **8**, 2068–2076 (1991).

13. Brons, J. *et al.* Powerful 100-fs-scale Kerr-lens mode-locked thin-disk oscillator. *Opt. Lett., OL* **41**, 3567–3570 (2016).

14.   Saraceno, C. J. *et al.* 275 W average output power from a femtosecond thin disk oscillator operated in a vacuum environment. *Opt. Express* **20**, 23535–23541 (2012).

15.   Saraceno, C. J., Sutter, D., Metzger, T. & Abdou Ahmed, M. The amazing progress of high-power ultrafast thin-disk lasers. *Journal of the European Optical Society-Rapid Publications* **15**, 15 (2019).

16.   Poetzlberger, M. *et al.* Kerr-lens mode-locked thin-disk oscillator with 50% output coupling rate. *Opt. Lett., OL* **44**, 4227–4230 (2019).

17.   Zhang, J. *et al.* High-Power, High-Efficiency Tm:YAG and Ho:YAG Thin-Disk Lasers. *Laser & Photonics Reviews* **12**, 1700273 (2018).

18.   Zhang, J., Mak, K. F. & Pronin, O. Kerr-Lens Mode-Locked 2-µm Thin-Disk Lasers. *IEEE Journal of Selected Topics in Quantum Electronics* **24**, 1–11 (2018).

19.   Zhang, J. *et al.* Intra-pulse difference-frequency generation of mid-infrared (2.7–20 µm) by random quasi-phase-matching. *Opt. Lett., OL* **44**, 2986–2989 (2019).

20.   Reichert, J., Holzwarth, R., Udem, Th. & Hänsch, T. W. Measuring the frequency of light with mode-locked lasers. *Optics Communications* **172**, 59–68 (1999).

21.   Telle, H. R. *et al.* Carrier-envelope offset phase control: A novel concept for absolute optical frequency measurement and ultrashort pulse generation. *Appl Phys B* **69**, 327–332 (1999).

22.   Apolonski, A. *et al.* Controlling the Phase Evolution of Few-Cycle Light Pulses. *Phys. Rev. Lett.* **85**, 740–743 (2000).

23.   Baltuška, A., Fuji, T. & Kobayashi, T. Controlling the Carrier-Envelope Phase of Ultrashort Light Pulses with Optical Parametric Amplifiers. *Phys. Rev. Lett.* **88**, 133901 (2002).

24.   Cerullo, G., Baltuška, A., Mücke, O. D. & Vozzi, C. Few-optical-cycle light pulses with passive carrier-envelope phase stabilization. *Laser & Photonics Reviews* **5**, 323–351 (2011).

25. Boyd, R. W. *Nonlinear Optics.* (Elsevier, 2008).

26. Pupeza, I. *et al.* High-power sub-two-cycle mid-infrared pulses at 100 MHz repetition rate. *Nature Photon* **9**, 721–724 (2015).

27. Gaida, C. *et al.* Watt-scale super-octave mid-infrared intrapulse difference frequency generation. *Light: Science & Applications* **7**, 94 (2018).

28. Butler, T. P. *et al.* Watt-scale 50-MHz source of single-cycle waveform-stable pulses in the molecular fingerprint region. *Opt. Lett., OL* **44**, 1730–1733 (2019).

29. Seidel, M. *et al.* Multi-watt, multi-octave, mid-infrared femtosecond source. *Science Advances* **4**, eaaq1526 (2018).

30. Xing, S. *et al.* All-fiber frequency comb at 2 μm providing 1.4-cycle pulses. *Opt. Lett., OL* **45**, 2660–2663 (2020).

31. Laubereau, A. & Kaiser, W. Vibrational dynamics of liquids and solids investigated by picosecond light pulses. *Rev. Mod. Phys.* **50**, 607–665 (1978).

32. Huber, M. *et al.* Detection sensitivity of field-resolved spectroscopy in the molecular fingerprint region. in *2017 Conference on Lasers and Electro-Optics Europe European Quantum Electronics Conference (CLEO/Europe-EQEC)* 1–1 (2017). doi:10.1109/CLEOE-EQEC.2017.8086921.

33. Pupeza, I. *et al.* Field-resolved spectroscopy in the molecular fingerprint region. in *2017 Conference on Lasers and Electro-Optics Europe European Quantum Electronics Conference (CLEO/Europe-EQEC)* 1–1 (2017). doi:10.1109/CLEOE-EQEC.2017.8086859.

34. Huber, M. *et al.* Optimum Sample Thickness for Trace Analyte Detection with Field-Resolved Infrared Spectroscopy. *Anal. Chem.* **92**, 7508–7514 (2020).

35. Huber, M. *et al.* Field-Resolved Infrared Transmission Spectroscopy of Strongly Absorbing Samples. in *2019 Conference on Lasers and Electro-Optics Europe European Quantum Electronics Conference (CLEO/Europe-EQEC)* 1–1 (2019). doi:10.1109/CLEOE-EQEC.2019.8872271.

36.   Pupeza, I. *et al.* Field-Resolved Infrared Spectroscopy of Biological Samples. in *2019 Conference on Lasers and Electro-Optics Europe European Quantum Electronics Conference (CLEO/Europe-EQEC)* 1–1 (2019). doi:10.1109/CLEOE-EQEC.2019.8872874.

37.   Pupeza, I. *et al.* Field-resolved infrared spectroscopy of biological systems. *Nature* **577**, 52–59 (2020).

38.   Zewail, A. H. Femtochemistry: Atomic-scale dynamics of the chemical bond. *J. Phys. Chem. A* **104**, 5660–5694 (2000).

39.   Itatani, J. *et al.* Tomographic imaging of molecular orbitals. *Nature* **432**, 867–871 (2004).

40.   Lewenstein, M., Balcou, Ph., Ivanov, M. Yu., L'Huillier, A. & Corkum, P. B. Theory of high-harmonic generation by low-frequency laser fields. *Phys. Rev. A* **49**, 2117–2132 (1994).

41.   Paul, P. M. *et al.* Observation of a Train of Attosecond Pulses from High Harmonic Generation. *Science* **292**, 1689–1692 (2001).

42.   Ghimire, S. & Reis, D. A. High-harmonic generation from solids. *Nature Physics* **15**, 10–16 (2019).

43.   Garg, M. *et al.* Multi-petahertz electronic metrology. *Nature* **538**, 359–363 (2016).

44.   Uemura, S. & Torizuka, K. Sub-40-fs Pulses from a Diode-Pumped Kerr-Lens Mode-Locked Yb-Doped Yttrium Aluminum Garnet Laser. *Jpn. J. Appl. Phys.* **50**, 010201 (2011).

45.   Südmeyer, T. *et al.* High-power ultrafast thin disk laser oscillators and their potential for sub-100-femtosecond pulse generation. *Appl. Phys. B* **97**, 281 (2009).

46.   Brons, J. *et al.* Energy scaling of Kerr-lens mode-locked thin-disk oscillators. *Opt. Lett., OL* **39**, 6442–6445 (2014).

47.   Pronin, O. *et al.* High-power 200 fs Kerr-lens mode-locked Yb:YAG thin-disk oscillator. *Opt Lett* **36**, 4746–4748 (2011).

48. Zhang, J. *et al.* 260-megahertz, megawatt-level thin-disk oscillator. *Opt. Lett., OL* **40**, 1627–1630 (2015).

49. Fritsch, K., Poetzlberger, M., Pervak, V., Brons, J. & Pronin, O. All-solid-state multipass spectral broadening to sub-20 fs. *Opt. Lett.* **43**, 4643 (2018).

50. Huber, M. *et al.* Active intensity noise suppression for a broadband mid-infrared laser source. *Opt. Express* **25**, 22499 (2017).

51. Birks, T. A., Knight, J. C. & Russell, P. S. J. Endlessly single-mode photonic crystal fiber. *Optics letters* **22**, 961–963 (1997).

52. Dudley, J. M., Genty, G. & Coen, S. Supercontinuum generation in photonic crystal fiber. *Rev. Mod. Phys.* **78**, 1135–1184 (2006).

53. Demmler, S. *et al.* Generation of high quality, 1.3 cycle pulses by active phase control of an octave spanning supercontinuum. *Optics express* **19**, 20151–20158 (2011).

54. Jocher, C., Eidam, T., Hädrich, S., Limpert, J. & Tünnermann, A. Sub 25 fs pulses from solid-core nonlinear compression stage at 250 W of average power. *Opt. Lett., OL* **37**, 4407–4409 (2012).

55. Seidel, M., Xiao, X. & Hartung, A. Solid-Core Fiber Spectral Broadening at Its Limits. *IEEE Journal of Selected Topics in Quantum Electronics* (2018) doi:10.1109/JSTQE.2018.2811907.

56. Svelto, O. *Principles of Lasers.* (Springer US, 2010). doi:10.1007/978-1-4419-1302-9.

57. Karow, M., Tünnermann, H., Neumann, J., Kracht, D. & Weßels, P. Beam quality degradation of a single-frequency Yb-doped photonic crystal fiber amplifier with low mode instability threshold power. *Opt. Lett., OL* **37**, 4242–4244 (2012).

58. Schulte, J., Sartorius, T., Weitenberg, J., Vernaleken, A. & Russbueldt, P. Nonlinear pulse compression in a multi-pass cell. *Opt. Lett.* **41**, 4511 (2016).

59. Engel, G. S. & Moyer, E. J. Precise multipass Herriott cell design: Derivation of controlling design equations. *Opt. Lett.* **32**, 704 (2007).

60. Seidel, M., Arisholm, G., Brons, J., Pervak, V. & Pronin, O. All solid-state spectral broadening: an average and peak power scalable method for compression of ultrashort pulses. *Opt. Express, OE* **24**, 9412–9428 (2016).

61. Emaury, F., Diebold, A., Saraceno, C. J. & Keller, U. Compact extreme ultraviolet source at megahertz pulse repetition rate with a low-noise ultrafast thin-disk laser oscillator. *Optica, OPTICA* **2**, 980–984 (2015).

62. Mak, K. F. *et al.* Compressing μJ-level pulses from 250 fs to sub-10 fs at 38-MHz repetition rate using two gas-filled hollow-core photonic crystal fiber stages. *Opt. Lett.* **40**, 1238 (2015).

63. Møller, U. *et al.* Power dependence of supercontinuum noise in uniform and tapered PCFs. *Opt. Express, OE* **20**, 2851–2857 (2012).

64. Petrov, V. Frequency down-conversion of solid-state laser sources to the mid-infrared spectral range using non-oxide nonlinear crystals. *Progress in Quantum Electronics* **42**, 1–106 (2015).

65. Petrov, V. Parametric down-conversion devices: The coverage of the mid-infrared spectral range by solid-state laser sources. *Optical Materials* **34**, 536–554 (2012).

66. Manzoni, C. & Cerullo, G. Design criteria for ultrafast optical parametric amplifiers. *J. Opt.* **18**, 103501 (2016).

67. SNLO software (free version). *AS-Photonics* https://as-photonics.com/products/snlo/.

68. Valdmanis, J. & Mourou, G. Subpicosecond electrooptic sampling: Principles and applications. *IEEE Journal of Quantum Electronics* **22**, 69–78 (1986).

69. Wu, Q. & Zhang, X. -C. Free-space electro-optic sampling of terahertz beams. *Appl. Phys. Lett.* **67**, 3523–3525 (1995).

70. Nahata, A., Weling, A. S. & Heinz, T. F. A wideband coherent terahertz spectroscopy system using optical rectification and electro-optic sampling. *Appl. Phys. Lett.* **69**, 2321–2323 (1996).

71. Wu, Q. & Zhang, X.-C. Free-space electro-optics sampling of mid-infrared pulses. *Appl. Phys. Lett.* **71**, 1285–1286 (1997).

72. Leitenstorfer, A., Hunsche, S., Shah, J., Nuss, M. C. & Knox, W. H. Detectors and sources for ultrabroadband electro-optic sampling: Experiment and theory. *Appl. Phys. Lett.* **74**, 1516–1518 (1999).

73. Kaindl, R. A., Eickemeyer, F., Woerner, M. & Elsaesser, T. Broadband phase-matched difference frequency mixing of femtosecond pulses in GaSe: Experiment and theory. *Appl. Phys. Lett.* **75**, 1060–1062 (1999).

74. Kübler, C., Huber, R., Tübel, S. & Leitenstorfer, A. Ultrabroadband detection of multi-terahertz field transients with GaSe electro-optic sensors: Approaching the near infrared. *Appl. Phys. Lett.* **85**, 3360–3362 (2004).

75. Keiber, S. *et al.* Electro-optic sampling of near-infrared waveforms. *Nature Photon* **10**, 159–162 (2016).

76. Keiber, S. Novel metrology techniques resolve strong-field-driven electron dynamics in solids. (Ludwig-Maximilians-Universität München, 2016).

77. Sulzer, P. *et al.* Determination of the electric field and its Hilbert transform in femtosecond electro-optic sampling. *Phys. Rev. A* **101**, 033821 (2020).

78. Gallot, G. & Grischkowsky, D. Electro-optic detection of terahertz radiation. *J. Opt. Soc. Am. B* **16**, 1204 (1999).

79. Porer, M., Ménard, J.-M. & Huber, R. Shot noise reduced terahertz detection via spectrally postfiltered electro-optic sampling. *Opt. Lett., OL* **39**, 2435–2438 (2014).

80. Tomasino, A. *et al.* Wideband THz Time Domain Spectroscopy based on Optical Rectification and Electro-Optic Sampling. *Scientific Reports* **3**, 3116 (2013).

81.   Nemoto, N., Higuchi, T., Kanda, N., Konishi, K. & Kuwata-Gonokami, M. Highly precise and accurate terahertz polarization measurements based on electro-optic sampling with polarization modulation of probe pulses. *Opt. Express, OE* **22**, 17915–17929 (2014).

82.   Li, K., Wang, S., Han, X. & Wang, Z. Dispersion Measurement of Electro-Optic Coefficient γ22 of Lithium Niobate Based on Photoelastic Modulation. *Applied Sciences* **10**, 395 (2020).

83.   Audier, X., Balla, N. & Rigneault, H. Pump-probe micro-spectroscopy by means of an ultra-fast acousto-optics delay line. *Opt. Lett., OL* **42**, 294–297 (2017).

84.   Schubert, O. *et al.* Rapid-scan acousto-optical delay line with 34 kHz scan rate and 15 as precision. *Opt. Lett.* **38**, 2907 (2013).

85.   Kliebisch, O., Heinecke, D. C. & Dekorsy, T. Ultrafast time-domain spectroscopy system using 10 GHz asynchronous optical sampling with 100 kHz scan rate. *Opt. Express, OE* **24**, 29930–29940 (2016).

86.   Brabec, T. & Krausz, F. Nonlinear Optical Pulse Propagation in the Single-Cycle Regime. *Phys. Rev. Lett.* **78**, 3282–3285 (1997).

87.   Quinlan, F. *et al.* Exploiting shot noise correlations in the photodetection of ultrashort optical pulse trains. *Nature Photon* **7**, 290–293 (2013).

88.   Semrock - Part Number: FF01-950/SP. https://www.semrock.com/FilterDetails.aspx?id=FF01-950/SP-25.

89.   Shortpass Filter / IR 930nm | Asahi Spectra USA Inc. https://www.asahi-spectra.com/opticalfilters/detail.asp?key=XIS0930&key4=.

90.   Thorlabs - FES0950 Ø1" Shortpass Filter, Cut-Off Wavelength: 950 nm. https://www.thorlabs.de/thorproduct.cfm?partnumber=FES0950.

91.   Buberl, T., Alismail, A., Wang, H., Karpowicz, N. & Fattahi, H. Self-compressed, spectral broadening of a Yb:YAG thin-disk amplifier. *Opt. Express, OE* **24**, 10286–10294 (2016).

92.   Jullien, A. *et al.* Spectral broadening and pulse duration reduction during cross-polarized wave generation: influence of the quadratic spectral phase. *Appl. Phys. B* **87**, 595–601 (2007).

93.   Schweinberger, W. *et al.* Interferometric delay tracking for low-noise Mach-Zehnder-type scanning measurements. *Opt. Express* **27**, 4789 (2019).

94.   Hofer, C. *et al.* Quantum-Efficiency and Bandwidth Optimized Electro-Optic Sampling. in *2019 Conference on Lasers and Electro-Optics Europe European Quantum Electronics Conference (CLEO/Europe-EQEC)* 1–1 (2019). doi:10.1109/CLEOE-EQEC.2019.8873083.

95.   Puskar, L. & Schade, U. The IRIS THz/Infrared beamline at BESSY II. *Journal of large-scale research facilities JLSRF* **2**, 95 (2016).

96.   Rogalski, A. History of infrared detectors. *Opto-Electronics Review* **20**, 279–308 (2012).

97.   Doherty, J., Cinque, G. & Gardner, P. Single-cell analysis using Fourier transform infrared microspectroscopy. *Applied Spectroscopy Reviews* **52**, 560–587 (2017).

98.   Brandstetter, M., Volgger, L., Genner, A., Jungbauer, C. & Lendl, B. Direct determination of glucose, lactate and triglycerides in blood serum by a tunable quantum cascade laser-based mid-IR sensor. *Appl. Phys. B* **110**, 233–239 (2013).

99.   Schwaighofer, A. *et al.* Beyond Fourier Transform Infrared Spectroscopy: External Cavity Quantum Cascade Laser-Based Mid-infrared Transmission Spectroscopy of Proteins in the Amide I and Amide II Region. *Anal. Chem.* **90**, 7072–7079 (2018).

100.   Akhgar, C. K. *et al.* The Next Generation of IR Spectroscopy: EC-QCL-Based Mid-IR Transmission Spectroscopy of Proteins with Balanced Detection. *Anal. Chem.* **92**, 9901–9907 (2020).

101.   Cheeseman, S. *et al.* Applications of Synchrotron-Source IR Spectroscopy for the Investigation of Insect Wings. *Synchrotron Radiation - Useful and Interesting Applications* (2019) doi:10.5772/intechopen.84591.

102.   Shi, H. & Yu, P. Advanced synchrotron-based and globar-sourced molecular (micro) spectroscopy contributions to advances in food and feed research on molecular structure, mycotoxin determination, and molecular nutrition. *Critical Reviews in Food Science and Nutrition* **58**, 2164–2175 (2018).

103.   Lanin, A. A., Voronin, A. A., Fedotov, A. B. & Zheltikov, A. M. Time-domain spectroscopy in the mid-infrared. *Scientific Reports* **4**, 6670 (2014).

104.   Amotchkina, T. *et al.* Broadband dispersive Ge/YbF3 mirrors for mid-infrared spectral range. *Opt Lett* **44**, 5210–5213 (2019).

105.   Habel, F. & Pervak, V. Dispersive mirror for the mid-infrared spectral range of 9–11.5 μm. *Appl. Opt., AO* **56**, C71–C74 (2017).

106.   Amotchkina, T., Trubetskov, M., Schulz, M. & Pervak, V. Comparative study of NIR-MIR beamsplitters based on ZnS/YbF3 and Ge/YbF3. *Opt Express* **27**, 5557–5569 (2019).

107.   Riek, C. *et al.* Direct sampling of electric-field vacuum fluctuations. *Science* **350**, 420–423 (2015).

108.   Yang, H., Yang, S., Kong, J., Dong, A. & Yu, S. Obtaining information about protein secondary structures in aqueous solution using Fourier transform IR spectroscopy. *Nature Protocols* **10**, 382–396 (2015).

109.   Haus, H. A. Mode-locking of lasers. *IEEE Journal of Selected Topics in Quantum Electronics* **6**, 1173–1185 (2000).

110.   Jones, D. J. *et al.* Carrier-Envelope Phase Control of Femtosecond Mode-Locked Lasers and Direct Optical Frequency Synthesis. *Science* **288**, 635–639 (2000).

111.   Liao, R. *et al.* Active f-to-2f interferometer for record-low jitter carrier-envelope phase locking. *Opt. Lett.* **44**, 1060 (2019).

112.   Borchers, B., Koke, S., Husakou, A., Herrmann, J. & Steinmeyer, G. Carrier-envelope phase stabilization with sub-10 as residual timing jitter. *Optics letters* **36**, 4146–4148 (2011).

113.   Koke, S. *et al.* Direct frequency comb synthesis with arbitrary offset and shot-noise-limited phase noise. *Nature Photon* **4**, 462–465 (2010).

114.   Rybka, T. *et al.* Sub-cycle optical phase control of nanotunnelling in the single-electron regime. *Nature Photon* **10**, 667–670 (2016).

115.   Yoshioka, K. *et al.* Subcycle mid-infrared coherent transients at 4 MHz repetition rate applicable to light-wave-driven scanning tunneling microscopy. *Opt. Lett.* **44**, 5350 (2019).

116.   Kowligy, A. S. *et al.* Infrared electric field sampled frequency comb spectroscopy. *SCIENCE ADVANCES* 8 (2019).

117.   Vernaleken, A. *et al.* Carrier-envelope frequency stabilization of a Ti:sapphire oscillator using different pump lasers. *Opt. Express, OE* **20**, 18387–18396 (2012).

118.   Butler, T. P. *et al.* Multi-octave spanning, Watt-level ultrafast mid-infrared source. *J. Phys. Photonics* **1**, 044006 (2019).

119.   Liang, H. *et al.* High-energy mid-infrared sub-cycle pulse synthesis from a parametric amplifier. *Nat Commun* **8**, 141 (2017).

120.   Thiré, N. *et al.* 4-W, 100-kHz, few-cycle mid-infrared source with sub-100-mrad carrier-envelope phase noise. *Opt. Express, OE* **25**, 1505–1514 (2017).

121.   Liehl, A., Fehrenbacher, D., Sulzer, P., Leitenstorfer, A. & Seletskiy, D. V. Ultrabroadband out-of-loop characterization of the carrier-envelope phase noise of an offset-free Er:fiber frequency comb. *Opt. Lett.* **42**, 2050 (2017).

122.   Heiner, Z., Petrov, V., Steinmeyer, G., Vrakking, M. J. J. & Mero, M. 100-kHz, dual-beam OPA delivering high-quality, 5-cycle angular-dispersion-compensated mid-infrared idler pulses at 31 μm. *Opt. Express* **26**, 25793 (2018).

123.   Hussain, S. A., Schweinberger, W., Buberl, T., Hofer, C. & Pupeza, I. Train of Ultrashort Mid-Infrared Pulses with Sub-Mrad Carrier-Envelope Phase Stability. in *2019 Conference on Lasers and Electro-Optics Europe European Quantum Electronics Conference (CLEO/Europe-EQEC)* 1–1 (2019). doi:10.1109/CLEOE-EQEC.2019.8872659.

124.   Newbury, N. R. & Swann, W. C. Low-noise fiber-laser frequency combs (Invited). *J. Opt. Soc. Am. B* **24**, 1756 (2007).

125.   Liehl, A. *et al.* Deterministic Nonlinear Transformations of Phase Noise in Quantum-Limited Frequency Combs. *Phys. Rev. Lett.* **122**, 203902 (2019).

126.   Geyer, P. E., Holdt, L. M., Teupser, D. & Mann, M. Revisiting biomarker discovery by plasma proteomics. *Mol Syst Biol* **13**, (2017).

127.   Newbury, N. R., Coddington, I. & Swann, W. Sensitivity of coherent dual-comb spectroscopy. *Opt. Express, OE* **18**, 7929–7945 (2010).

128.   Fellinger, J. *et al.* Tunable dual-comb from an all-polarization-maintaining single-cavity dual-color Yb:fiber laser. *Opt. Express, OE* **27**, 28062–28074 (2019).

129.   Chen, B.-H., Hofer, C., Pupeza, I. & Baum, P. Second-harmonic generation and self-phase modulation of few-cycle mid-infrared pulses. *Opt. Lett.* **44**, 4079 (2019).

130.   Schubert, O. *et al.* Sub-cycle control of terahertz high-harmonic generation by dynamical Bloch oscillations. *Nature Photon* **8**, 119–123 (2014).

131.   Benko, C. *et al.* Extreme ultraviolet radiation with coherence time greater than 1 s. *Nature Photon* **8**, 530–536 (2014).

132.   Lind, A. J. *et al.* Mid-Infrared Frequency Comb Generation and Spectroscopy with Few-Cycle Pulses and χ(2) Nonlinear Optics. *Phys. Rev. Lett.* **124**, 133904 (2020).

133.   Catanese, A. *et al.* Mid-infrared frequency comb with 6.7 W average power based on difference frequency generation. *Opt. Lett., OL* **45**, 1248–1251 (2020).

List of publications

Hussain, Syed A., Christina Hofer, Maximilian Högner, Theresa Buberl, Wolfgang Schweinberger, Daniel Gerz, Marinus Huber, Philip Jacob, Alexander Weigel, Nicholas Karpowicz, Ferenc Krausz, Ioachim Pupeza, 'Sub-attosecond-precision optical-waveform stability measurements using electro-optic sampling', in review.

Pupeza, Ioachim, Marinus Huber, Michael Trubetskov, Wolfgang Schweinberger, **Syed A. Hussain**, Christina Hofer, and others, 'Field-Resolved Infrared Spectroscopy of Biological Systems', Nature, 577.7788 (2020), 52–59 https://doi.org/10.1038/s41586-019-1850-7

Alismail, Ayman, Haochuan Wang, Gaia Barbiero, Najd Altwaijry, **Syed Ali Hussain**, Volodymyr Pervak, and others, 'Multi-Octave, CEP-Stable Source for High-Energy Field Synthesis', Science Advances, 6.7 (2020), eaax3408 https://doi.org/10.1126/sciadv.aax3408

Huber, Marinus, Michael Trubetskov, **Syed A. Hussain**, Wolfgang Schweinberger, Christina Hofer, and Ioachim Pupeza, 'Optimum Sample Thickness for Trace Analyte Detection with Field-Resolved Infrared Spectroscopy', Analytical Chemistry, 92.11 (2020), 7508–14 https://doi.org/10.1021/acs.analchem.9b05744

Amotchkina, Tatiana, Michael Trubetskov, **Syed Ali Hussain**, Daniel Hahner, Daniel Gerz, Marinus Huber, and others, 'Broadband Dispersive Ge/YbF3 Mirrors for Mid-Infrared Spectral Range', Optics Letters, 44.21 (2019), 5210–13 https://doi.org/10.1364/OL.44.005210

Schweinberger, Wolfgang, Lenard Vamos, Jia Xu, **Syed A. Hussain**, Christoph Baune, Sebastian Rode, and others, 'Interferometric Delay Tracking for Low-Noise Mach-Zehnder-Type Scanning Measurements', Optics Express, 27.4 (2019), 4789 https://doi.org/10.1364/OE.27.004789

Seidel, Marcus, Xiao Xiao, **Syed A. Hussain**, Gunnar Arisholm, Alexander Hartung, Kevin T. Zawilski, and others, 'Multi-Watt, Multi-Octave, Mid-Infrared Femtosecond Source', Science Advances, 4.4 (2018), eaaq1526 https://doi.org/10.1126/sciadv.aaq1526

Acknowledgments

Value of each man depends upon the art and skill which he has attained.
(Peak of Eloquence, Imam Ali (a.s) ibn Abi Talib)

Beginning with the blessed name of the Almighty ALLAH, who is kind and knows the state of hearts very well. HIS blessings are innumerable and spread all over the universe. Peace and blessing be upon the greatest teacher of mankind, Holy Prophet Muhammad (peace be upon him). He and his Ahlul-Bayt (a.s) taught us the principle and manners leading to the true essence of life.

My sincere thanks go to Prof. Dr Ferenc Krausz, who has given me the opportunity to work in his world-leading research group, having great infrastructure. His scientific vision always inspired me and I learned a lot from him. My deep gratitude goes to my direct supervisor Ioachim Pupeza, for all the guidance, suggestions, and motivation to tackle the problems in the lab. Your passion to always push the technological milestone to their limits, has given constant energy to keep moving forward. I would like to thanks Nicholas Karpowicz, for always sharing his deep scientific understanding in simple words. And, I would like to thanks Hanieh Fattahi for providing energetic motivation and pieces of advice, in early phase of my PhD.

This work would not have been possible without the sincere help of many individuals. I am really thankful to all colleagues specifically Christina Hofer, Marinus Huber, Marcus Seidel, Kilian Fritsch, Daniel Gerz, Theresa Buberl, Maximilian Hoegner, Sebastian Gröbmeyer, Lenard Vamos, and Philip Jacob. All of you created a really friendly and supportive working environment. My special thanks go to Wolfgang Schweinberger, for all the scientific discussion, insights, and help in the Lab. All of that, improved my scientific understanding and had played a crucial role in completion of this work. I am grateful to the colleagues in the coating group specially Dr Michael Trubetskov, your software TRUFRS played a key role in quick data-processing and experimental optimizations. A deep gratitude to Naeem Ahmed, for all scientific and social discussions in the native language URDU, these helped a lot to get a bit relaxed.

Besides the working environment, I am also thankful to the local Pakistani community for all the social and religious programs, those have given a bit home-like feelings. I am also thankful to all of my teachers, from my childhood to university, all of you played a role in my career.

I would like to thank my mother, my brother and sisters for their never-ending support, care, and cordiality. My humble gratitude to my late father 'Sajid Hussain', who was an inspiration for me in many aspects of life. My heartfelt gratitude to my wife and

daughters, for the moral support, encouragement and well wishes. I stole your time quit often for my work, and I would like to sincerely thank you of all of your understanding and patience for those times.